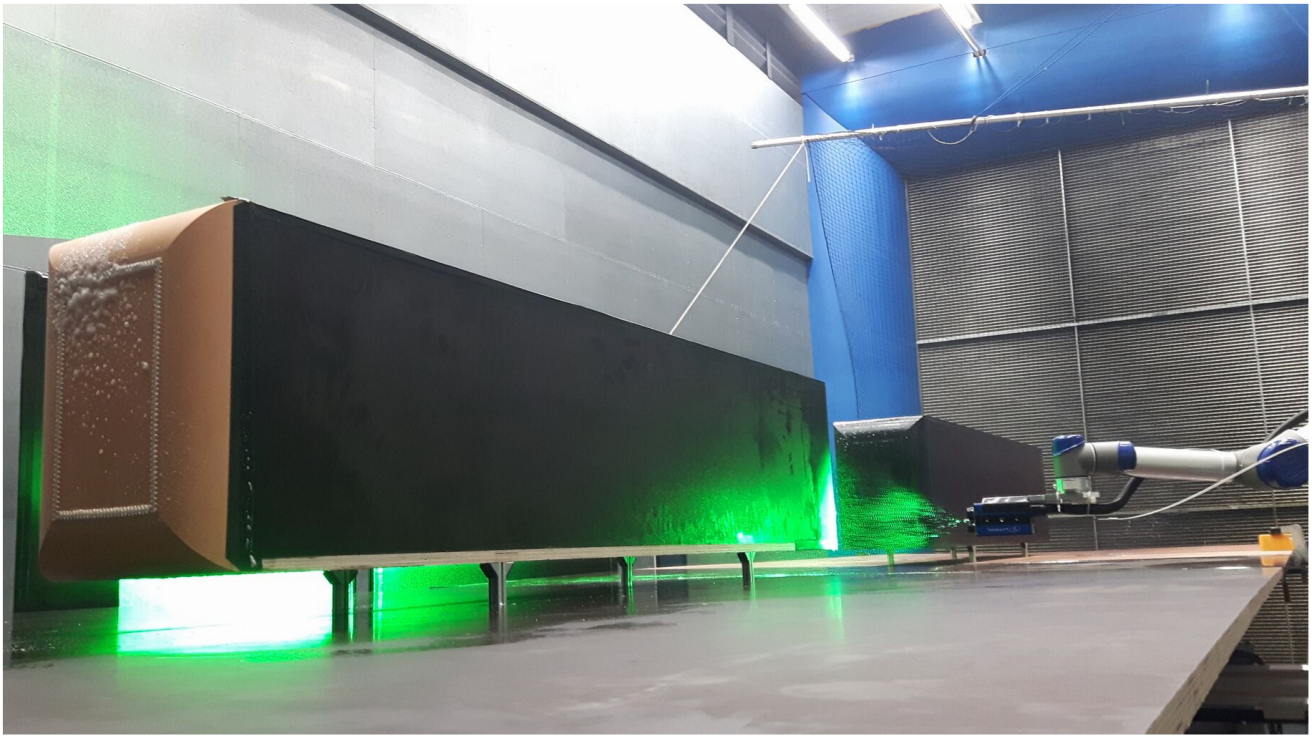
Master of Science Thesis



Flow analysis between two bluff bodies in a close distance platooning configuration

A Numerical and Experimental Study

Frank van Tilborg

January 29, 2018

Aerodynamics

TU Delft

Faculty of Aerospace Engineering

Delft University of Technology

Flow analysis between two bluff bodies in a close distance platooning configuration

A Numerical and Experimental Study

Master of Science Thesis

For obtaining the degree of Master of Science in Aerospace Engineering
at Delft University of Technology

Frank van Tilborg

January 29, 2018

Faculty of Aerospace Engineering · Delft University of Technology



Delft University of Technology

Copyright © Aerospace Engineering, Delft University of Technology
All rights reserved.

DELFT UNIVERSITY OF TECHNOLOGY
DEPARTMENT OF AERODYNAMICS

The undersigned hereby certify that they have read and recommend to the Faculty of Aerospace Engineering for acceptance the thesis entitled **"Flow analysis between two bluff bodies in a close distance platooning configuration"** by **Frank van Tilborg** in fulfillment of the requirements for the degree of **Master of Science**.

Dated: January 29, 2018

Supervisors:

Dr. Ir. G.M.R. van Raemdonck

Dr. A. Sciacchitano

Prof. Dr. F. Scarano

Prof. Dr. D. Casalino

Preface

This thesis concludes my masters study in Aerodynamics and also my years as a student at the Delft University of Technology. The subject required a lot of dedication and perseverance and over the past months I really learned a lot about heavy duty vehicle aerodynamics and how to conduct a numerical and experimental analysis. During the project I received a lot of help therefore I would like to thank some people.

First I would like to thank my daily supervisor Gandert van Raemdonck for his guidance during the project and never-ending enthusiasm about the subject. I would also like to thank Andrea Sciacchitano for his support and help during the wind tunnel experiment and throughout the project.

Furthermore many thanks go out to Damiano Casalino and Francesco Avallone for granting me access to use PowerFLOW for this study and helping me with the initial case set-up. Next to this the experimental campaign would not have been possible without the help of Daniele, Eduardo and Marijn as well as Jan Schneiders and the entire staff of the HSL.

Finally I would like to thank my friends, family and in particular my parents for giving me the opportunity to study at the TU Delft and supporting me in all kinds of ways during my studies.

Frank van Tilborg
Delft, January 2018

Abstract

In the European Union greenhouse gas emissions of heavy duty vehicles make up 30% of the total caused by road transport. By placing vehicles in a platoon configuration the aerodynamic drag can be heavily reduced. The effect of platooning has been studied on both American and European type vehicles. However many of these studies only disclose the drag reductions and do not fully explain the flow behaviour between the models which in the end is what is causing the reduction in drag. Next to this studies done on European type vehicles mostly used time-averaged simulations so a next step is understanding the effect of unsteady flow on the vehicles. In this study the flow field between two vehicles in a platooning configuration is analysed numerically and experimentally for varying intervehicle distance and front- and rear drag reduction devices. The GETS model was used in this study which is a simplified model of a European heavy duty vehicle. For the numerical analysis Exa PowerFLOW is used which is a transient CFD package based on the LBM. Turbulence is modelled using VLES together with a RNG of the $\kappa - \epsilon$ equations. A study of the mesh size showed the sensitivity on the drag coefficient of the single model.

The experimental analysis was performed in the OJF of the TU Delft at a Reynolds number of 3.9×10^5 based on the square root of the model. Next to balance measurements CVV measurements in the gap between the two models were taken in order to visualize the flow field.

The single model showed a toroidal recirculation region in which a vortex ring can be seen. The drag force fluctuates at a Strouhal number of 0.073, side and lift force at 0.058 and 0.102 and 0.130 and 0.160. These fluctuations are caused by pressure fluctuations in the wake where the highest magnitudes are seen in the shear layer. The models with a smaller front radius saw a rise in drag with flow separation occurring for the smallest radius for the numerical results and for both smaller radii in the experiment. The addition of a boat tail lowered the drag of the models. With increasing tail angles the drag reduction also increases which is caused by the increase in base pressure. The tails also decrease the force fluctuations due to decreased pressure fluctuations in the shear layer.

At the closest spacing of 0.10 times the vehicle length all tested configurations benefit from the platoon. The flow between the two models is made up of a toroidal recirculation region much smaller in size compared to the single model. In general the flow takes an S-shaped path between the two models. From the underbody of the leading model it either stagnates

on the front of the trailing model or moves into the gap where it ends up in the upper of lower vortex or stagnates on the front or rear of one of the models. When a sharper front edge radius is applied to the trailing model more flow is deflected into the gap leading to lower pressure vortices and a higher stagnation pressure. A small vertical misalignment of the trailing model, which was seen during the experimental campaign, leads to a higher stagnation pressure on the bottom of the trailing model, also here more flow is deflected into the gap. At this spacing the side-force fluctuations are a bit higher due to the vortices that leave the domain passing over the rounded edges of the model.
At the middle spacing of 0.45 times the vehicle length not all configurations benefit from the platoon. The trailing models with the baseline frontal radius saw an increase in drag due to the lack of thrust generated by the rounded edges. The other models did see a drag decrease. At this distance the wake of the leading model is quite similar to that of the single model. Flow enters from the top, bottom and sides of the model and ends up in the recirculation region or it stagnates on the rear of the model before it leaves the wake and stagnates on the front of the trailing model or flows over the rounded edges where it accelerates and leaves the gap. The effect of a sharper radius applied to the trailing model has little effect on the flow field. When a tail is applied to the leading model the recirculation region has been reduced as was seen for the single models. Due to the upwash the stagnation pressure on the bottom front has been increased but the drag has decreased compared to the platoon without a tail due to the increased suction of the rounded edges. At this distance the force fluctuations are much higher compared to the single model. The magnitude of drag and side force can go up to 2 and 6.5 times the values of the single model depending on the configuration. This is due to the stronger vortices from the leading model which pass over the trailing model.
For the last vehicle spacing of 0.91 s/L all the configurations benefit from the platoon again. For the baseline models the gains are only a few percent but for the trailing model with a sharper front radius the gains are higher than those at the middle intervehicle distance. This is due to the reduced stagnation pressure and almost undisturbed suction coming from the rounded edges. At this distance any effect on the wake of the leading vehicle has vanished. The unsteady forces still show an increased amplitude compared to the single model however compared to the middle intervehicle distance they are much lower.
The comparison between the results from the numerical and experimental analysis is quite good. The drag and flow field results are very similar. For the pressure and the unsteady forces this is less the case. The mismatch seen in the pressure comparison can be caused by alignment errors that were observed during the experiment. Next to this while reconstructing the flow field from the experimental measurements the resulting coordinates were outside the expected range. A manual coordinate shift was applied which may have resulted in additional errors. For the unsteady forces it is assumed that the ground plate and its interaction with the model as well as additional vibrations are the cause of the much higher fluctuations seen from the experimental data.

Table of Contents

Preface v

Abstract vii

Nomenclature xiii

1 Introduction 1

1.1 Bluff Body Aerodynamics . . . 2

1.1.1 Basis bluff body . . . 3

1.1.2 Drag reduction devices . . . 5

1.2 Platooning of bluff bodies . . . 7

1.3 Present Study . . . 12

2 Numerical Analysis 15

2.1 GETS Model . . . 15

2.2 Numerical Set-up . . . 17

2.2.1 Numerical Method and Turbulence Modelling . . . 17

2.2.2 Simulation Settings . . . 18

2.2.3 Simulation Volume and Boundary Conditions . . . 19

2.2.4 Wall Model . . . 21

2.2.5 Mesh Sensitivity . . . 22
2.3 Numerical Results . . . 24
2.3.1 Single Model . . . 24
2.3.2 Platoon . . . 33

3 Experimental Analysis 57
3.1 Experimental Set-up . . . 57
3.1.1 Open Jet Facility . . . 57
3.1.2 Wind Tunnel Models . . . 58
3.1.3 Performed Measurements . . . 59
3.1.4 Data Processing . . . 61
3.2 Experimental Results . . . 66
3.2.1 Single Model . . . 66
3.2.2 Platoon . . . 70

4 Discussion of Results 89
4.1 Comparison between numerical and experimental results . . . 89
4.1.1 Single Model . . . 89
4.1.2 Platoon . . . 94
4.2 Explanation of the differences between the numerical and experimental results . . . 110
4.2.1 Numerical Errors . . . 110
4.2.2 Experimental Errors . . . 111

5 Conclusions and Recommendations 113
5.1 Conclusions . . . 113
5.1.1 Single Model . . . 113
5.1.2 Platoon Configurations . . . 114
5.2 Recommendations . . . 116

Bibliography **119**

A Experimental Set-up **125**

A.1 Single Model 125

A.2 Platoon 126

Nomenclature

α_t	Tail Angle	[°]
ϵ_n	Nozzle blockage factor at the model	[-]
ϵ_{qn}	Nozzle blockage factor at the nozzle	[-]
ϵ_s	Solid blockage factor at the model	[-]
ν	Kinematic Viscosity	$[m^2/s]$
ρ	Density	$[kg/m^3]$
τ	Solid Blockage Constant	[-]
C	Duplex nozzle area	$[m^2]$
C_e	Effective nozzle area	$[m^2]$
C_D	Drag Coefficient	[-]
C_{D_i}	Drag Coefficient Isolated Model	[-]
C_{D_p}	Drag Coefficient Platoon Model	[-]
CFD	Computational Fluid Dynamics	
C_p	Pressure Coefficient	[-]
CVV	Coaxial Volumetric Velocimetry	
f	Frequency	[Hz]
h_m	Model Height	[mm]
$h_{r,m}$	Model Ride Height	[mm]
L,l_m	Model Length	[mm]
l_t	Tail Length	[mm]
LBM	Lattice Boltzmann Method	
NLR	National Aerospace Laboratory	
OTF	Optical Transfer Function	
PSD	Power Spectrum Density	
r_m	Model Front Radius	[mm]
R_n	Hydraulic Radius	[m]
Re	Reynolds Number	[-]
RNG	Renormalization Group	
S	Frontal Area	$[m^2]$
s/L	Intervehicle Distance	[-]
STB	Shake The Box	
St	Strouhal Number	[-]

u	Velocity along x coordinate	[m/s]
v	Velocity along y coordinate	[m/s]
V	Model Volume	[m^3]
VLES	Very Large Eddy Simulation	
w	Velocity along z coordinate	[m/s]
w_m	Model Width	[mm]
y^+	Non-dimensional wall distance	[-]
x_m	Distance between the centre of the model and the nozzle	[m]
x_s	Distance between the source and the nozzle	[m]

Chapter 1

Introduction

In the European Union CO_2 emissions from heavy duty vehicles currently make up 30% of all on-road transport Muncrief and Sharpe (2015). By 2030 this share is expected to increase to 45% Miller and Façanha (2014). At typical European highway speeds (83 km/h) aerodynamic drag accounts for 40% of fuel consumption and thus CO_2 emissions Frank and Turney (2016). For higher speeds the resistance due to aerodynamic drag is even larger which can be seen in figure 1.1.

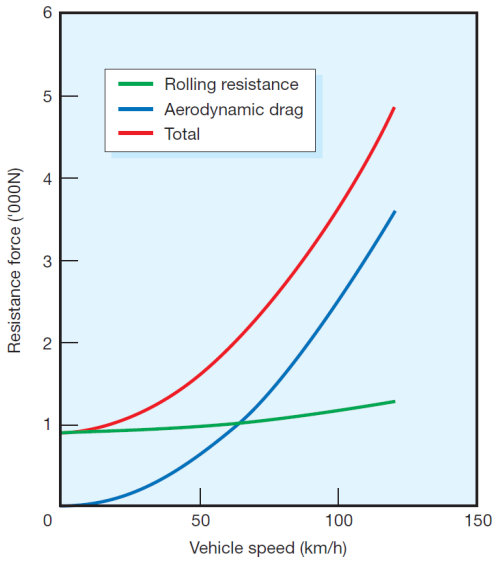


Figure 1.1: Resistance forces acting on a 10-tonne rigid vehicle at various speeds Harwell and Didcot (2001)

Streamlining heavy duty vehicles can have a large effect on the aerodynamic drag and therefore fuel consumption. This can be done by improving the aerodynamics of a single vehicle, as was done by McAuliffe (2015) and Hyams et al. (2011).

Next to improving the aerodynamic shape of a single vehicle the drag can also be reduced by using several vehicles driving behind each other which is called a platoon. The drag is reduced because the trailing vehicles drive in the low-velocity wake of the leading vehicle. Track tests done on American type trucks showed that the average fuel reduction for the platoon ranges from 8%, for an inter-vehicle distance of 8-10 m, up to 11% for a closer spacing of 3-4 m at a velocity of 22.4 m/s Browand et al. (2004). When next to the vehicle spacing, mass and speed are also varied the fuel savings drop for the heavier vehicles and the vehicles driving at higher speeds. The study showed that average fuel savings range from 3.7% to 6.4% Lammert et al. (2014). A study on the fuel saving in a platoon of European type vehicles, which lack the extended nose that is present on their American counterparts, was done by Bonnet and Fritz (2000). Track tests showed that in a two vehicle platoon driving at 80 km/h with a spacing of 10 m the trailing vehicle reduced its fuel consumption by 21% and the lead vehicle with 7%.

In Europe platooning of heavy duty vehicles has recently gotten more attention due to the European Truck Platooning Challenge which was issued in 2016 by the Netherlands during their EU presidency. In April of 2016 platoons from various European truck manufacturers departed from their headquarters and drove across Europe to meet up in the Netherlands. Because of this challenge experience and knowledge about driving in platoons on public roads in Europe was gained Eckhardt (2016). An example of a platoon that took part in the challenge can be seen in figure 1.2.



Figure 1.2: Example of a truck platoon European Truck Platooning (2016)

1.1 Bluff Body Aerodynamics

Before the state-of-art research on platooning is studied first studies done on the aerodynamics of a single bluff body and the effect of drag reduction devices will be presented.

1.1.1 Basis bluff body

The drag of a bluff body consists of friction and pressure drag where the latter is the main contributor due to the overall shape. A study done by Wood (2006) showed the main regions of drag contribution for which a graphic overview is shown in figure 1.3. From this it can be seen that 50% of the drag is generated by the front and wake. The other regions of drag are the tractor trailer gap and the underbody.

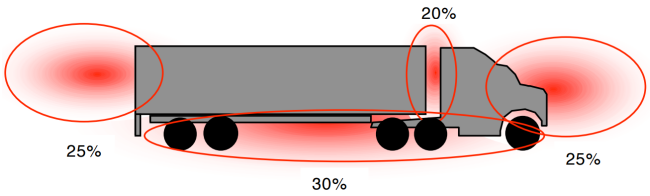
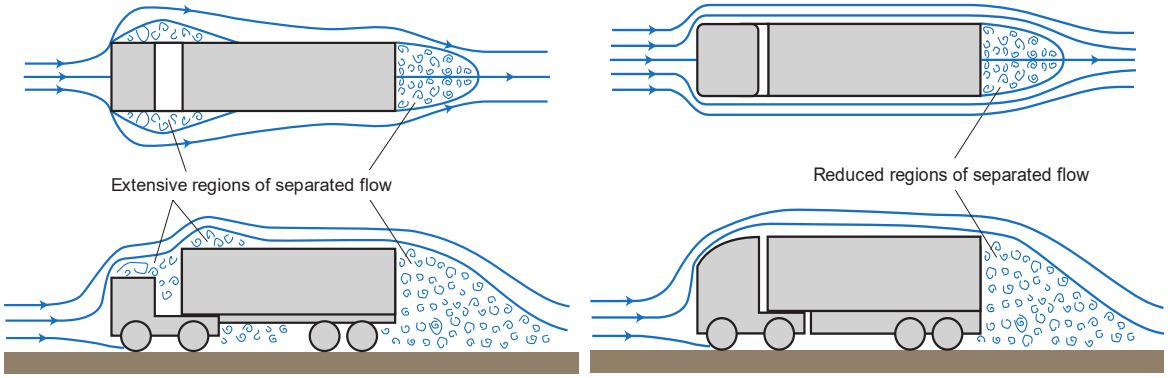


Figure 1.3: Regions of drag contribution for a tractor trailer Wood (2006)

Most of the drag comes from separated flow as can be seen in figure 1.4(a). This can be partly solved by streamlining the truck by minimizing the tractor trailer gap, introducing trailer skirts and cab roof fairings. Due to these improvements most of the regions of separated flow disappear as can be seen in figure 1.4(b) but the region of separated flow that remains is the wake.



(a) Flow field around a basic truck

(b) Flow field around a streamlined truck

Figure 1.4: Flow field around a basic and streamlined truck Harwell and Didcot (2001)

This wake is a region of unsteady flow and was investigated by Duell and George (1999), Bayraktar et al. (2001) and Khalighi et al. (2001), a schematic of the wake structure can be seen in figure 1.5. It was found that the wake consisted of a large ring-type vortex in which two smaller vortices of unequal strength are located. Wrapped around this wake region is a shear layer which is caused by the separating boundary layer at the base of the model. The vortices near the base of the model are shed at a Strouhal number of 1.157 based on the height of the model. Vortices are shed uniformly first from one side and obliquely from the top of the model. After half a period the process is reversed, the uniform vortex shedding occurs at the opposite side and the oblique vortex comes from the bottom of the model. Due

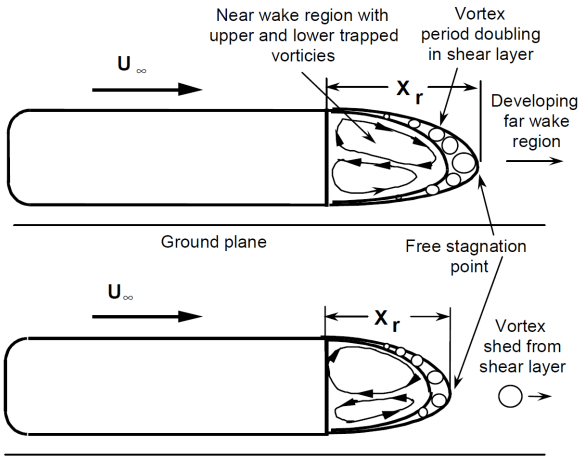


Figure 1.5: Schematic of the wake structure and pumping phenomenon Duell and George (1999)

to the shedding of these vortices a pseudo-helical vortex structure is formed. Downstream the vortices interact with each other and pair resulting in increased vortex size and a reduced frequency. This continues until they reach the stagnation point of the wake where they leave the shear layer at a Strouhal number of 0.069 based on the height of the model. This pumping motion causes the stagnation point to move up- and downstream changing the strength of the vortices in the wake region. The periodic drag values of bluff bodies is related to this pumping motion because of the pressure fluctuations associated with it.

Ortega et al. (2004) investigated the flow mechanism in the wake of the GTS model by performing unsteady large-eddy simulations and wind tunnel tests. In figure 1.6 iso-surfaces of the vorticity magnitude are shown at different time instances. The ring vortex found by others is also visible here in the top left figure. After that a secondary vortex ring develops but this one is less coherent than the first one. The vortex rings break apart downstream and flow downwards. The shear layer coming from the base of the GTS model moves in a wavelike motion and regularly sheds vortices in the wake. From the bottom right figure it can be seen that the wake interacts with the ground to form a separation bubble on the ground. Next to this they also showed that coherent swirling structures are formed on the corners of the GTS model which do not dissipate and extend beyond the wake.

The wake of the GETS model was investigated by Van Raemdonck and Van Tooren (2008) for varying forebody roughness which changes the thickness of the boundary layer. This was done by applying zig-zag tape of different thicknesses to the front of the model. The time-averaged wake structure can be seen in figure 1.7. This is in good agreement with the structure reported by Duell and George (1999), as can be seen there are two vortices present labelled by v1 and v2 as well as the stagnation point SP with their respective lengths and heights. When thicker zig-zag tape was applied the drag increased, with this increasing drag the stagnation point moved downstream and down in the vertical direction. This is because the secondary vortex v2 moves downstream while the primary one, v1 stays stationary.

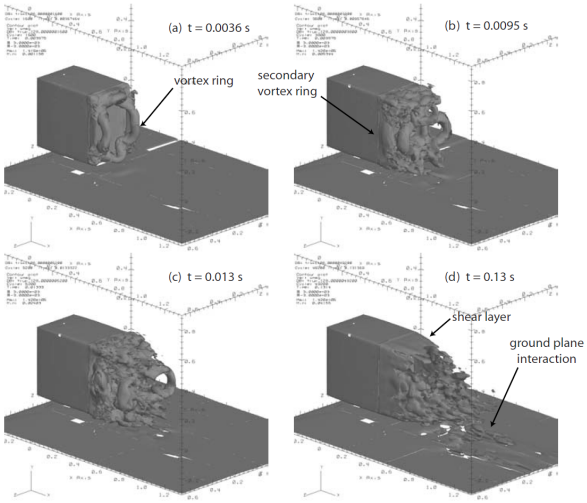


Figure 1.6: Iso-surfaces of the vorticity magnitude at different times for the fine grid Ortega et al. (2004)

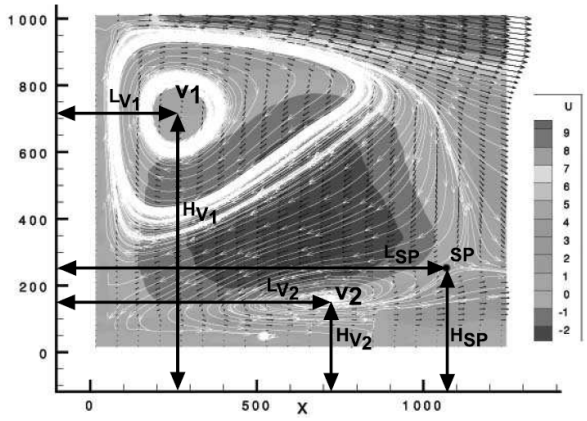


Figure 1.7: Structure of the wake when the thinnest tape was applied Van Raemdonck and Van Tooren (2008)

1.1.2 Drag reduction devices

Drag reduction devices come in many types such as: tractor-trailer gap devices, trailer skirts, boat-tails, etc. and have shown to reduce the drag of bluff bodies to a great extent. An example of a boat-tail applied to a heavy-duty vehicle can be seen in figure 1.8.

A study done by McAuliffe (2015) assessed the performance of various drag reduction devices on an American type tractor-trailer combination. A wind tunnel test on a 30% tractor-trailer model consisting of an International ProStar Short Sleeper tractor and a 53 ft trailer was done. Five different boat-tails were tested all with an angle of 13° for which the results can be seen in figure 1.9. It can be seen that the performance difference between the types of boat-tails is very small. The drag reduction provided by the boat-tails lies between 5.7% and 6.8% which is quite small compared to others. This could be due to that the tails were not



Figure 1.8: Example of a boat-tail applied to a heavy-duty vehicle Canadian Trucking Alliance (2014)

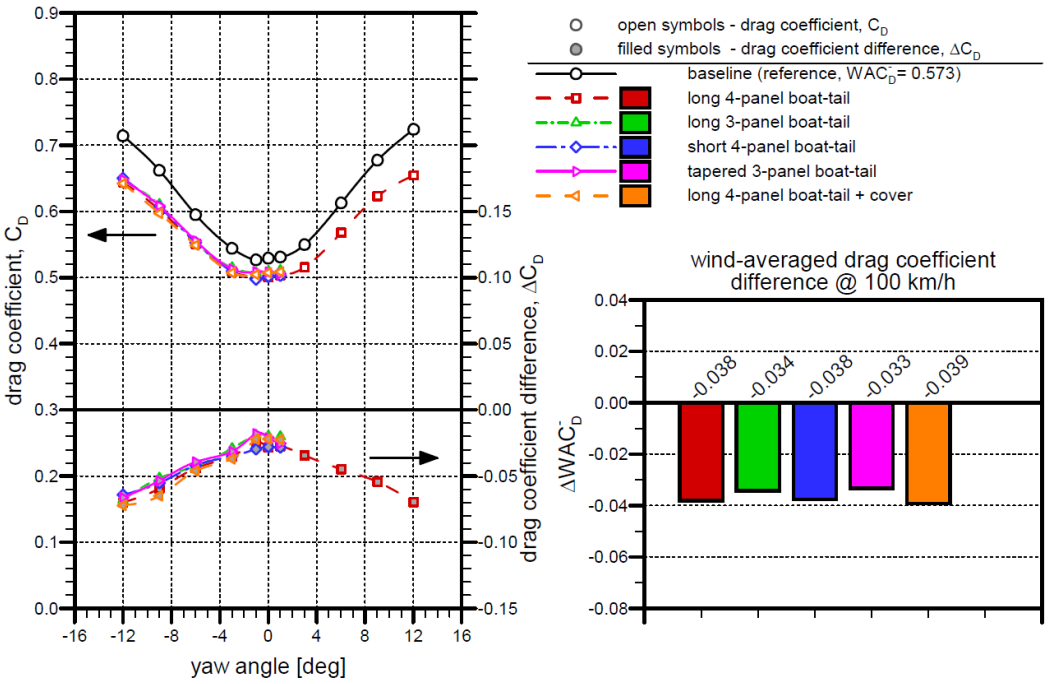


Figure 1.9: Effect of different boat-tails McAuliffe (2015)

installed flush with the roof of the trailer to allow for lights. This gap could cause a region of reversed flow hindering the wake to converge inwards. From the figure it is also observed that the drag reduction capability of the boat-tails increases with increasing crosswind angle.

Whereas McAuliffe only tested different type of boat-tails with a fixed angle, Van Raemdonck (2012) also tested tails with different angles. A wind tunnel experiment on the GETS model showed that the complete 4-sided, open, planar boat-tail with an angle of 12° reduced the drag by 30%. When the boat-tail is elongated this can even increase to 40% because a higher pressure recovery can be achieved. As was found by McAuliffe, van Raemdonck also found that the boat-tails performance increased with increasing crosswind angles.

Next to wind tunnel tests numerical studies on the performance of boat-tails were also done. Hyams et al. (2011) did a full-scale simulation using unsteady RANS on the

Generic Conventional Model equipped with a planar boat-tail of 15° with a panel length one quarter of the trailer width. A wind averaged drag reduction of 15% was found. The boat-tail performance was not influenced much by the crosswind angle but did manage slightly better when no crosswind was present.

Ellis et al. (2015) also did simulations on a truck with drag reduction devices. In this case a full-scale simulation using the lattice Boltzmann Method was done on a Volvo VNL 670 pulling a 53 foot trailer with various aero packages. In the first variation trailer skirts measuring 7 m in length were added which resulted in a 9% drag decrease. The next configuration consisted of the same trailer skirts but next to this a front fairing and boat-tail was added. This resulted in an additional 12% drag reduction. In the final configuration the standard trailer skirts were replaced with ones covering the entire length of the trailer this resulted in an 5% drag decrease compared to the second configuration.

The effect of a drag reduction device on the unsteady wake was investigated by Khalighi et al. (2001). A stepped tail with panel length of 50 mm and 8 mm offset from the edges of the model was installed on a square-back bluff body. A wind tunnel test, steady and unsteady simulations were performed on this model and a drag reduction of 20% was found. Next to this the difference between the wakes with and without the stepped tail was also studied. When the tail was installed the wake became narrower but its length stayed the same. The stepped tail also caused the highly unsteady flow in the wake to die down significantly which can be seen in figure 1.10.

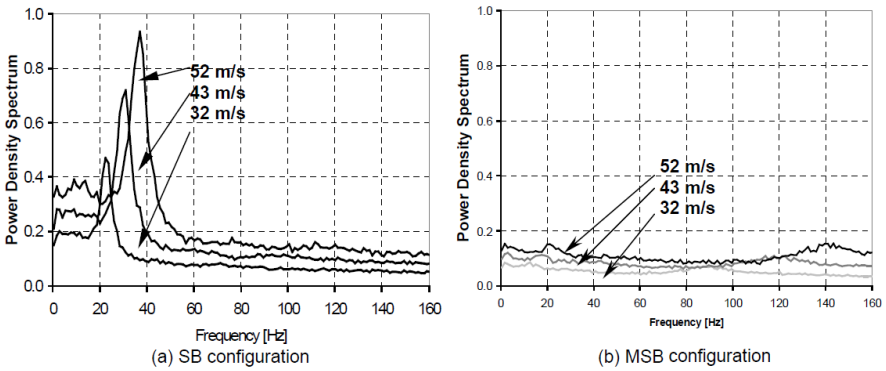


Figure 1.10: Power density spectrum of the hot-wire measurements done in the wake square-back (left) and modified square-back with tail (right) Khalighi et al. (2001)

1.2 Platooning of bluff bodies

Platooning is the act of vehicles driving close to each other such that the trailing vehicle drives in the wake of the leading one. Both vehicles benefit from this situation because the pressure in the wake of the leading vehicle increases while the stagnation pressure on the front of the trailing vehicle decreases. This leads to a drag reduction for both vehicles. Several studies have already been performed on the platooning of bluff bodies. An overview of the effect of

platooning on the fuel consumption for heavy duty vehicles can be seen in figure 1.11. It can be seen that when the separation distance reduces the fuel consumption also reduces, however the results from the different studies are quite spread out.

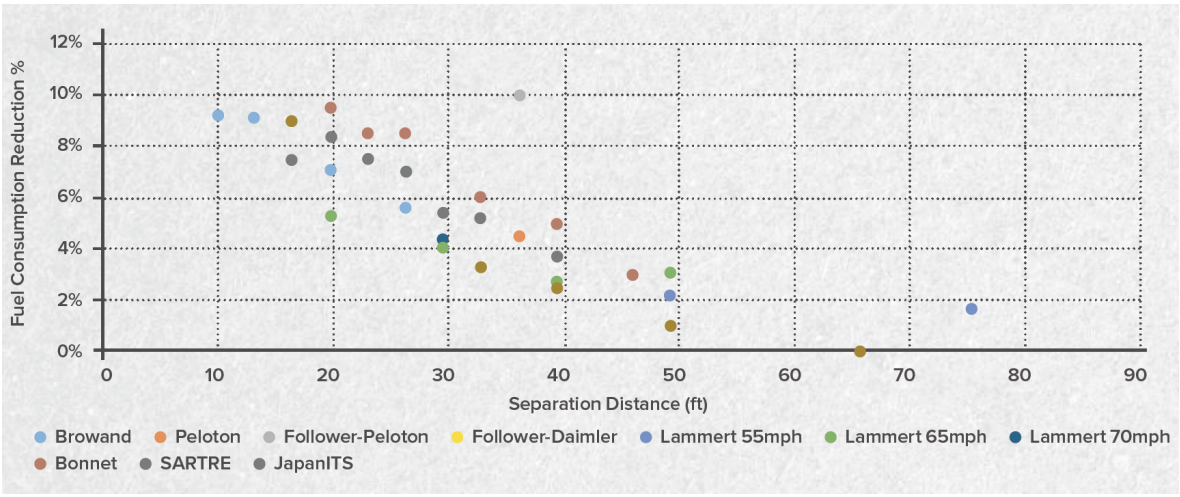


Figure 1.11: Reduction of fuel consumption for the lead heavy duty vehicle (unless stated otherwise) in a platoon at various separation distances Roberts et al. (2016)

Next to heavy duty vehicles, platooning of car models has also been tested. Watkins and Vino (2008) investigated the drag of a platoon of Ahmed models with a slant angle of 30° for an inter-vehicle spacing ranging from 0.1 to 4.0 vehicle lengths. For a spacing from 0.1 to 1.0 vehicle lengths it was shown that the drag of the trailing vehicle increased. For inter-vehicle distances larger than 1.0 the drag of the trailing vehicle went below that of the isolated vehicle. The leading vehicle did benefit from the smaller inter-vehicle distances and returned to the drag value in isolation for the larger spacings. This behaviour was confirmed by Mirzaei and Krajnović (2016) which did a large eddy simulation on the Ahmed platoon but this time with a slant angle of 25°. Three inter-vehicle distances were simulated namely: 0.3, 0.5 and 1 times the vehicle length. For all three the drag of the trailing vehicle was found to be higher than that of the leading one. This increased drag of the trailing vehicle was due to the vortices that are shed by the leading vehicle and impinge on the trailing one.

A study on the platooning of more truck-like models was done by Hammache and Browand (2004) which investigated the drag savings that can be achieved by placing two models with either a blunt or rounded front behind each other. This resulted in four platoon configurations that were tested in the wind tunnel for different inter-vehicle distances for which the results can be seen in figure 1.12. For the inter-vehicle distance between 0 and 1 there is a strong interaction which drops off for larger inter-vehicle distances. For a small inter-vehicle distance the lead vehicle experiences a value of about 70%-90% of the isolated drag value depending on whether the rounded or blunt front is applied. For the trailing vehicle the drag decrease is even stronger at a small inter-vehicle distance. For the blunt front it is 40% of the isolated value and for the rounded front it even drops to 20%.

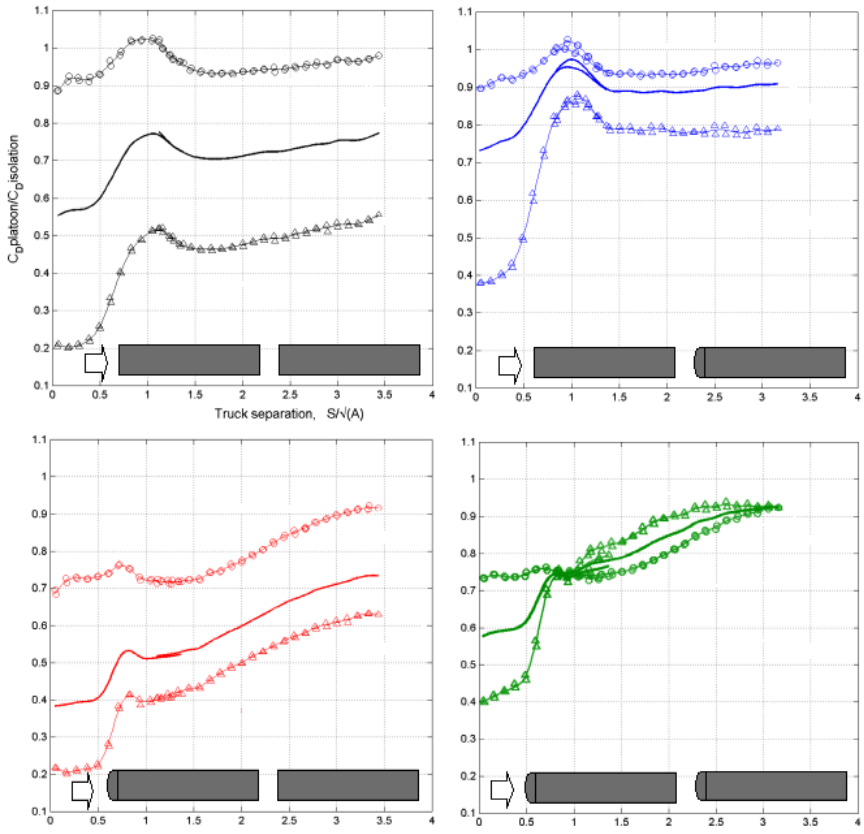


Figure 1.12: Drag curves for the four different platoon configurations: ○ lead vehicle, △ trailing vehicle,— platoon average Hammache and Browand (2004)

All platoon configurations experience a lower drag coefficient compared to the isolated case. The trailing vehicle receives a larger drag reduction than the lead vehicle in almost all configurations except one. Where both vehicles have a rounded front in the strong interaction region the trailing vehicle still experiences a higher drag decrease than the lead vehicle. However outside this strong interaction region the opposite is true. Applying a rounded front to the lead vehicle always decreases the drag of the vehicle and the platoon. When applying the rounded front to the trailing vehicle it increases the drag of the vehicle and the platoon. The optimal configuration is the one with the rounded front applied to the lead vehicle and the blunt front applied to the trailing vehicle. This configuration resembles that of an A-Train configuration the most which is in correspondence to the findings of Mihelic et al. (2015).

They performed a numerical study on a full scale 2 vehicle platoon and an A-train in order to compare the aerodynamic performance of the two configurations to the single vehicle, all of which are shown in figure 1.13. A detailed Peterbilt 579 was used as tractor for all configurations, the platoon vehicles used a 16.15 m long trailer and were separated 9.14 m. The A-train used two trailers of 14.63 m and these were separated 0.762 m. Simulations were performed at three different crosswind angles of 0°, 2° and 6° and results were averaged in order to arrive at so called wind averaged coefficients. It was shown that for the platoon both vehicles benefited. The drag of the lead vehicle decreased with 12% while the trailing vehicle

achieved a 14% drag reduction. The drag of the A-train increased with 18 % with respect to the single vehicle. But compared to the freight volume this results in an drag decrease of 35%. This shows that the A-train has an even better aerodynamic performance than the platoon but because of regulations in the European union this is not an option European Union (1996).

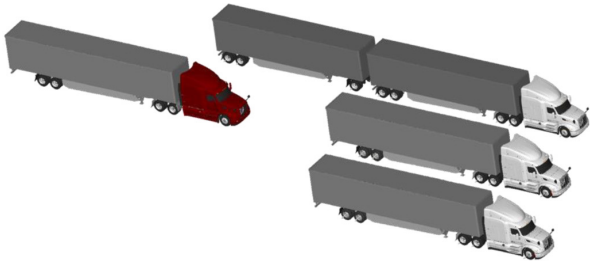


Figure 1.13: A-train, platoon and single vehicle used in Mihelic et al. (2015)

Another study about a two vehicle platoon was done by Hammache et al. (2002). Three different types of simplified truck models were used which can be seen in figure 1.14. The clean truck has netting but no wheels and no collar, the dirty truck has netting, wheels and a collar which increases the boundary layer thickness, the last configuration is the same as the dirty one but in this case a height mismatch between the cab and trailer is present. These different configurations were used in various platoons for which the platoon averaged results are shown in figure 1.15. The drag rises gradually up until a truck separation of 0.5. This is due to relatively stable cavity-like flow between the two trucks which is made up of the vortex ring shed by the leading truck. At a truck separation of 0.5 the drag rises steeply. This is because the previously mentioned stable flow structure disappears and the cavity flow becomes unstable and the vortex ring spends less time in the cavity. After a truck separation of 1 the flow in the wake is comparable to that of an isolated vehicle. It is also seen that when an aerodynamically clean and dirty truck are placed in a platoon it is better to place the clean truck in front.

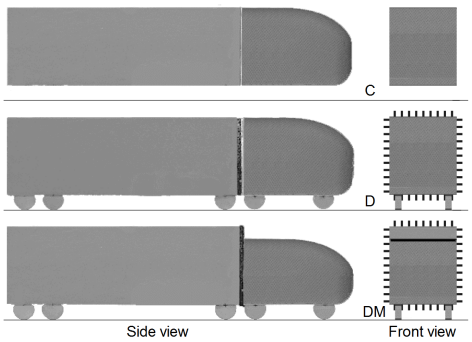


Figure 1.14: Overview of the clean (C), dirty (D) and dirty mismatch (DM) trucks Hammache et al. (2002)

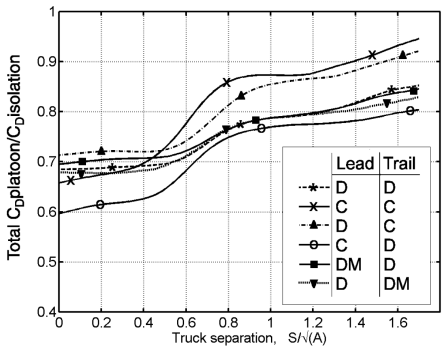


Figure 1.15: Average drag ratios for various truck platoons Hammache et al. (2002)

From figure 1.12 it can be seen that the drag reduction increases with decreasing inter-vehicle

distance. It would seem that is also the case for real life tractor-trailers, however there is a limit. As the inter-vehicle distance decreases the mass flow going through the radiator for the trailing vehicle also decreases, to compensate for this the engine fan needs to engage which reduces fuel savings. This was noticed by Smith et al. (2014) and studied by Ellis et al. (2015). The study done by Smith also investigated the drag reduction for a 2 vehicle platoon for 4 inter-vehicle distances of 30, 60, 100 and 160 ft. For the leading vehicle drag reductions increased as the inter-vehicle distance decreased. For the trailing vehicle this was also the case except for the lowest spacing of 30 ft where the drag increased again. This drag increase was due to reduced suction pressures, because of the lower flow velocity, on the curved surfaces such as the roof fairing of the Peterbilt 579. Because this type of truck has a very different geometry than the average European type truck this behaviour may not be observed. Ellis et al. (2015) tested a 3 vehicle platoon with the various configurations described in subsection 1.1.2 at inter-vehicle distances of 5 and 9 meters for two crosswind angles of 0° and 5°. Compared to the single vehicle the platoon with 9 m spacing offers a large reduction in drag. Reducing the inter-vehicle gap to 5 m only offers little extra reduction. Platooning also delivers higher drag reductions for the more aerodynamic vehicles, that is because they can benefit more efficiently from the protection of the upstream vehicle. The middle vehicle benefits the most from the platooning followed by the trailing vehicle and the lead vehicle shows the highest drag. Part of the drag reduction comes from the reduced mass-flow going through the radiator but this also means that less heat can be rejected which increases the possibility of the fan engaging which may void the potential fuel savings. At 9 m separation there was no reason for the fan to engage but at 5 m because of the reduced mass-flow and increased temperature in the engine bay it is expected that the fan would engage.

Marcu and Browand (1999) studied the effect crosswind has on a platoon of vehicles. A 3 vehicle platoon consisting of 1:8 scale Chevrolet Lumina minivans was tested in the wind tunnel at 10° crosswind and various inter-vehicle distances ranging from 0 to 0.72 vehicle lengths. The drag reducing effect of platooning did not diminish much under crosswind conditions. Between the yaw angles of 0° and 10° at 0.1 vehicle spacing the platoon average drag coefficient only increased 3%, from 58% to 61%. For all inter-vehicle spacings the middle vehicle experienced the greatest drag reduction. The lead vehicle experienced the greatest side force and thus also the greatest yawing moment. The side force and yawing moments for the following vehicles were considerably reduced. This was the case because the first vehicle realigned the flow in the travel direction of the platoon. It was also shown that the side force and yawing moment on the lead vehicle are influenced very little by trailing vehicles. The drag coefficient of the vehicles in the platoon are affected by the upstream neighbours the most and little by the downstream ones.

The effect of crosswind on a platoon consisting of heavy duty vehicles was investigated by Hai-lin et al. (2016). Two full scale European type trucks were tested for an inter-vehicle distance ranging from 0 to 30 m and crosswind angles from 0° to 20° using the XFlow software package. For the leading vehicle at the crosswind angles of 0°, 5° and 10° the drag reduction is about 10% at the smaller inter-vehicle spacings and diminishes gradually as they increase. For the higher crosswind angles of 15° and 20° the drag reduction is on the order of 5% and changes very little as inter-vehicle distances increase. For the trailing vehicle the story is very different however. When no crosswind is applied the drag reduction is about 70% for

small inter-vehicle distances and goes down as they increase. When a crosswind is applied the behaviour changes quite a bit. For starters the drag reduction at small inter-vehicle distances is about 60% for crosswind angles of 5°, 10° and 15° and 55% for the highest crosswind angle of 20°. The change of drag reduction as inter-vehicle distance increases is also quite different. For the smallest crosswind angle of 5° there is a drag increase in the region from 0 to 5 m after that the drag rises steeply where at about 1 vehicle length spacing it drops a little bit and fluctuates for the rest of the test range. As the crosswind angle increases the drag in the region from 0 to 5 m inter-vehicle spacing increases more rapid. On the other hand the drag in the second region going from 5 m to 1 vehicle length inter-vehicle spacing rises more slowly and seems to plateau as the crosswind angle increases. The drag for the larger inter-vehicle spacing is not influenced much with the increasing crosswind angle.

Gheyssens (2016) studied the effect of drag reduction devices consisting of front edge radius and the application of a boat tail, on a 3 vehicle platoon under cross wind conditions. Time averaged simulations showed that changing the front edge radius had a big influence on the flow. For larger radii the drag increased while for smaller radii the opposite was true. For smaller inter-vehicle distances the lead vehicle experienced large drag reductions due to the high pressure region from the middle vehicle. The trailing vehicle drag increased for decreasing inter-vehicle distances because of the inward deflection of the streamlines coming from the middle vehicle. The drag of the middle vehicle remained fairly constant experiencing both effects from the lead and trailing vehicle. When tails were added or had more inward deflection the drag reduction decreased. Cross wind conditions only had a little effect on the drag reduction of the platoon.

1.3 Present Study

The discussed literature in the above sections indicates that there is a great interest in reducing the aerodynamic drag of heavy duty vehicles by placing them in a platoon configuration. It is known that this reduction of drag leads to reduced fuel consumption and thus less emissions of CO_2 and other greenhouse gasses. Most of the studies in section 1.2 only presented the drag reductions and do not disclose anything referring to the flow field between the vehicles which is responsible for the drag reduction. This leads to the main question that this study will try to answer which is.

"How can the interacting wake flow of a leading vehicle in a bluff body platoon, with changing conditions, be characterized?"

These changing conditions will consist of varying intervehicle distance as well as modifications done at the front and rear of the bluff body. Because literature shows a large scatter of the results for platoons at close distances small intervehicle distances will be investigated. Next to this previous work done on platoons at the department was always done using time-averaged simulations. In this study transient simulations will be performed in order to understand the time dependency of the flow behaviour. This can be summarized into the following sub-questions.

- How does the flow behaviour change with intervehicle distance?
- What is the effect of front and rear body modifications on the flow field?
- What is the effect of the unsteady wake flow on the bluff bodies?

To answer the above questions use will be made of two analysis methods. One numerical which is discussed in the next chapter. The second analysis method is an experimental one which is handled in chapter 3. Next to this the results from both analysis methods will be compared to each other in chapter 4. Finally conclusions are drawn and recommendations are given for future studies. This is done in chapter 5.

Chapter 2

Numerical Analysis

The first method of analysing the flow between the two models will be done by using computational fluid dynamics (CFD). The geometry of the model will be handled in section 2.1. The chosen CFD code used in this study is the commercial software package Exa PowerFLOW which will be discussed in section 2.2. Afterwards the results from this analysis are presented in section 2.3.

2.1 GETS Model

European heavy-duty vehicles have a complex geometry. Next to the separation that exists between the tractor and trailer they are made up of additional parts such as the wheels, mirrors, grilles, bumpers etc. Since this study focuses on the flow between two heavy-duty vehicles these features are not required and would heavily increase the simulation and production cost for the experimental models. That is why a simplified model is used called the Generalized European Transport System which was introduced by Van Raemdonck and Van Tooren (2008). This GETS model can be seen in figure 2.1. The dimensions of both the scaled down model that will be used in this study and full scale model are given in table 2.1.

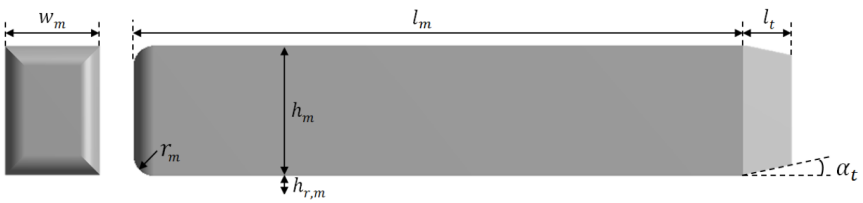


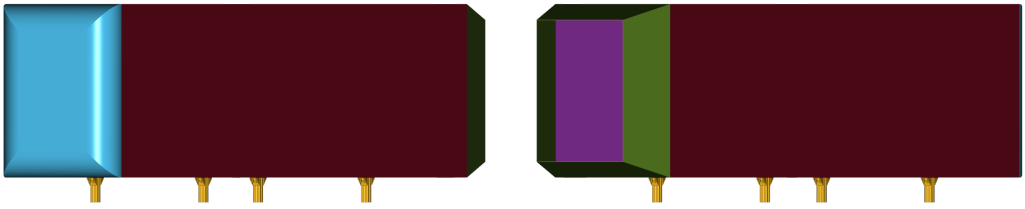
Figure 2.1: Geometry of the GETS model

Table 2.1: Dimensions of the scaled and full scale GETS model

Variable	Unit	Symbol	1:8	1:1
Length	[mm]	l_m	2063	16500
Width	[mm]	w_m	325	2600
Height	[mm]	h_m	439	3500
Front radius	[mm]	r_m	68*	540*
Tail length	[mm]	l_t	188	1500
Tail angle	[°]	α_t	12*	12*
Ride height	[mm]	$h_{r,m}$	63	500

* these values will be varied

For the simulation the model is split up into multiple parts which can be used later to see which part contributes the most to the drag. The drag contribution of each part is calculated by integrating the pressure and shear stress acting on it. In figure 2.2 these parts are made recognizable by giving them different colours. The front part is coloured blue, the rear purple. The sides, top and bottom have a maroon colour while the tail is green, lastly the supports that will also be simulated to have as little difference between the simulation and experiment are coloured yellow.



(a) Front view (b) Rear view

Figure 2.2: Parts breakdown of the GETS model

2.2 Numerical Set-up

2.2.1 Numerical Method and Turbulence Modelling

The first method to analyse the flow between the two GETS models is by using CFD. With this method the flow is simulated using mathematical equations that are calculated on computers. Most CFD codes use the Navier-Stokes equations however the software package that was used for this study which is Exa PowerFLOW 5.4a makes use of the lattice Boltzmann equations to simulate the flow. The lattice Boltzmann method is based on kinetic theory of gases and instead of directly calculating macroscopic variables such as velocity and pressure which is done by Navier-Stokes codes it models the interaction of molecules. The problem is expressed by a one-body distribution function $f(\mathbf{x}, \mathbf{v}, t)$ which indicates the density of particles at a given position $\mathbf{x}$, velocity $\mathbf{v}$ and time t. The resulting Boltzmann equation is given by equation 2.1 Chen et al. (2003).

$$\frac{Df}{Dt} = \frac{\partial f}{\partial t} + \mathbf{v} \cdot \frac{\partial f}{\partial \mathbf{x}} = C(f, f) \tag{2.1}$$

In this equation the left hand side represents the free-streaming of the molecules in space and time while the right hand side covers the complex interactions and collisions between molecules. In order to calculate this term PowerFLOW uses the Bhatnagar-Gross-Krook (BGK) collision term operator Bhatnagar et al. (1954). The particle distribution is calculated by solving the kinetic equations on a Cartesian mesh where each cube is named a voxel. On this Cartesian mesh particles are allowed to move in three dimensions using 19 discrete velocities better known as the D3Q19 model (figure 2.3). This model also recovers the Navier-Stokes equations when a third-order truncation of the Chapman-Enskog expansion is applied Succi and Yeomans (2001). During each simulated time step PowerFLOW models the particles in two distinct phases. In the first phase the particles, described by the distribution function, move from the voxel they currently occupy to an adjacent voxel. The second phase describes the interactions and collisions which are necessary to bring the system to a local thermodynamic equilibrium and ensures the correct results from the kinetic equations Exa Corporation (2017b). After these two phases the process repeats itself and particles are allowed to move to an adjacent voxel again.

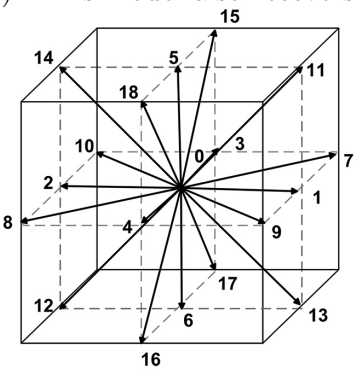


Figure 2.3: D3Q19 Model

Because of the high Reynolds number is it not feasible to use direct simulation to resolve all the scales of motion. That is why turbulence modelling must be used. PowerFLOW uses very large eddy simulation (VLES) together with a $\kappa - \epsilon$ Renormalization group (RNG) for the smaller unresolved scales Exa Corporation (2017b).

2.2.2 Simulation Settings

Before the grid around the model can be created first the options used for the simulation must be defined. The options used for this study can be seen in figure 2.4. A 3D external flow without heat transfer at a low Mach number was chosen. The simulated fluid is modelled as an ideal gas. Particle modelling was turned off as was vehicle simulation which is only necessary if one wants to know more about the forces and moments on the individual axles of the vehicle. Solver precision was set to single as this is standard practice. Lastly the boundary layer transition model was unchecked as it is assumed that the boundary layer starts out turbulent because during the experiment is was tripped using zig-zag tape. Next to the simulation options some characteristic variables must also be defined which will be used by the simulation. These are given in figure 2.5. From the figure it can be seen that the characteristic pressure is set to the standard atmospheric pressure at sea level. The velocity, temperature and viscosity are set in such a way that they are equal or as close as possible to the wind tunnel experiment. The characteristic length and area are defined as the square root of the frontal area of the model and the frontal area itself. The value in the resolution field comes from a mesh sensitivity analysis which will be given in section 2.2.5. The simulated Mach number is set to be chosen by PowerFLOW. This allows PowerFLOW to execute the simulation at a higher Mach number which reduces the computational time. At a higher Mach number the particles will flow faster across voxels and each time step will consist of a longer interval in time. This means less time steps are required to run the duration of the entire simulation. This simulated Mach number has a limit around 0.4 because the results are independent on the Mach number for values below and up to this Mach number Exa Corporation (2017a). Next to the resolution the duration of the simulation will also be explained in section 2.2.5. The following parameters are standard values for air. Lastly the turbulence intensity is set at 2%. For the OJF the free stream turbulence intensity is 0.5% as reported by Lignarolo et al. (2014). However when the seeding rake is introduced which will be done to conduct the CVV measurements this will increase the turbulence intensity. Jux (2017) investigated the increase of turbulence intensity and reported a value of about 2 % which was used for all simulations. The turbulence length scale is kept at the standard value of 5 mm.

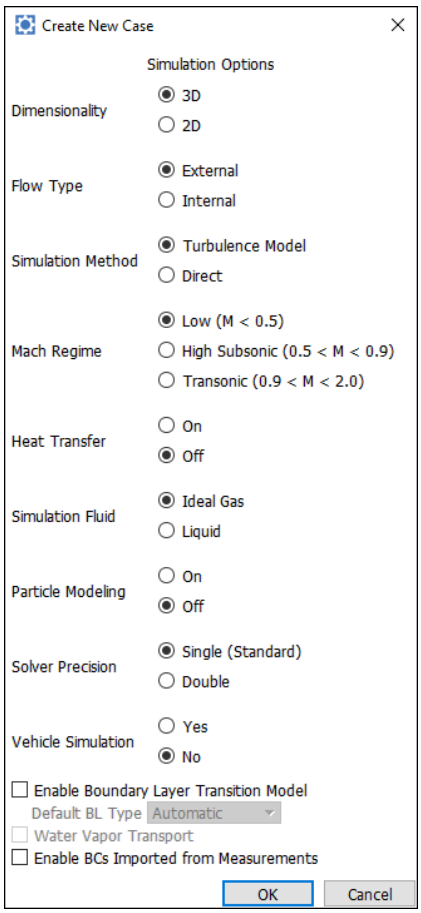


Figure 2.4: Simulation Options

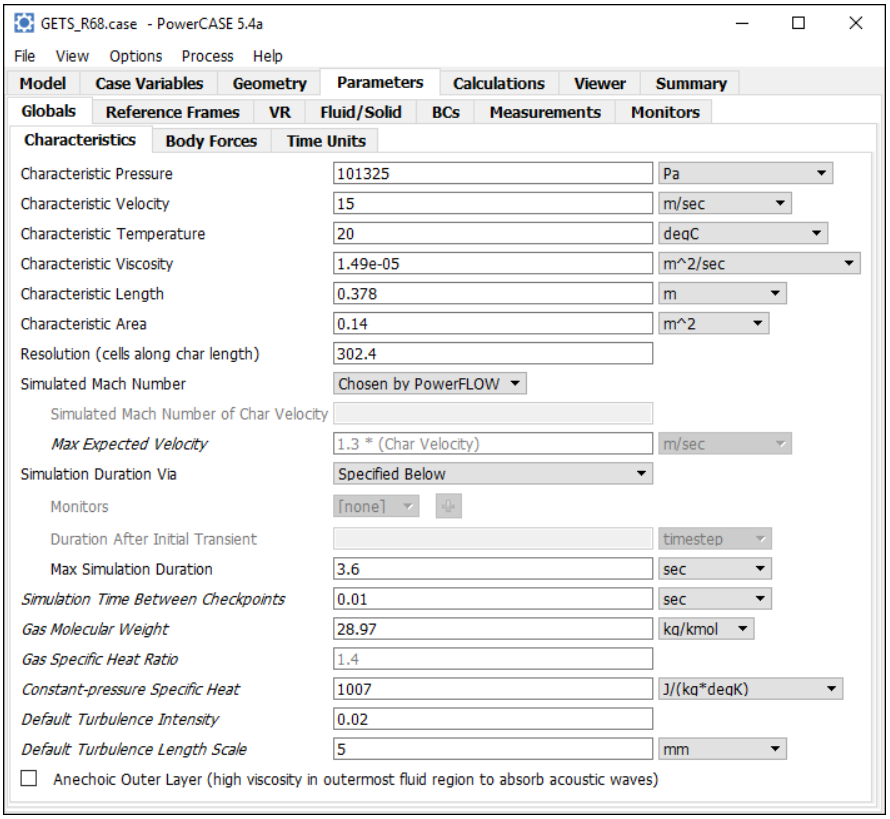


Figure 2.5: Characteristic variables used in the simulation

2.2.3 Simulation Volume and Boundary Conditions

Around the GETS model a simulation volume was created in which the flow is calculated. The dimensions of this simulation volume are based on the recommendations of SAE (2013) and can be seen in figure 2.6. From this it can be seen that the length is 11 times the length of the model with 3 lengths being upstream of the model and 7 lengths downstream. The model is placed laterally in the middle of the domain which is 10 model widths wide. Lastly the simulation volume is 6 model heights high. To resemble the experimental set-up as much as possible a ground plate was placed underneath the model, this plate has roughly the same dimensions as the one used during the experiment.

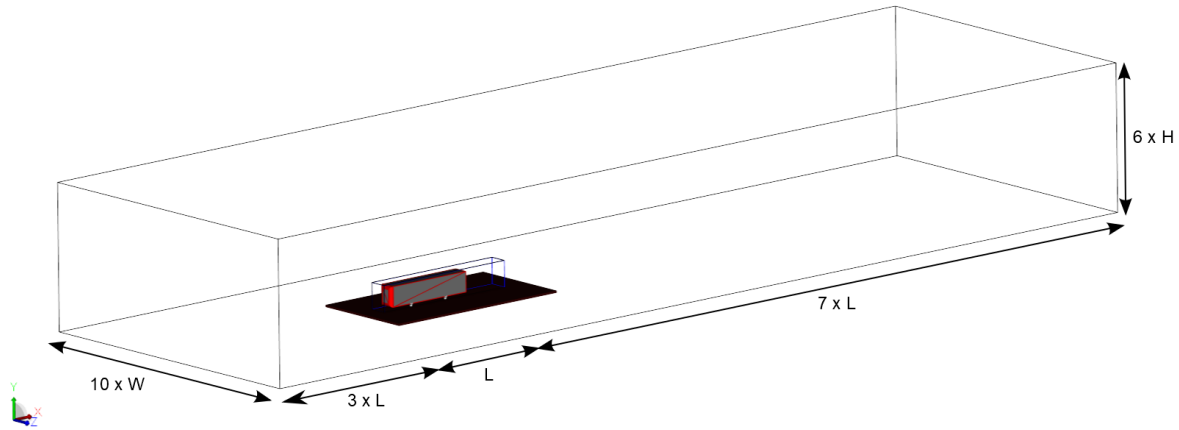


Figure 2.6: Simulation Volume Dimensions

Because one wants to have enough spatial resolution around the model two additional regions were created where a higher resolution discretization is enabled. These regions can be seen in figure 2.7, the region in red is a 5 mm offset and the blue box has a length of 1.6 times the model length. 10% of the model length is placed upstream and 50% is placed downstream of the model. The width and height of this wakebox is 1.2 and 1.3 times the width and height of the model.

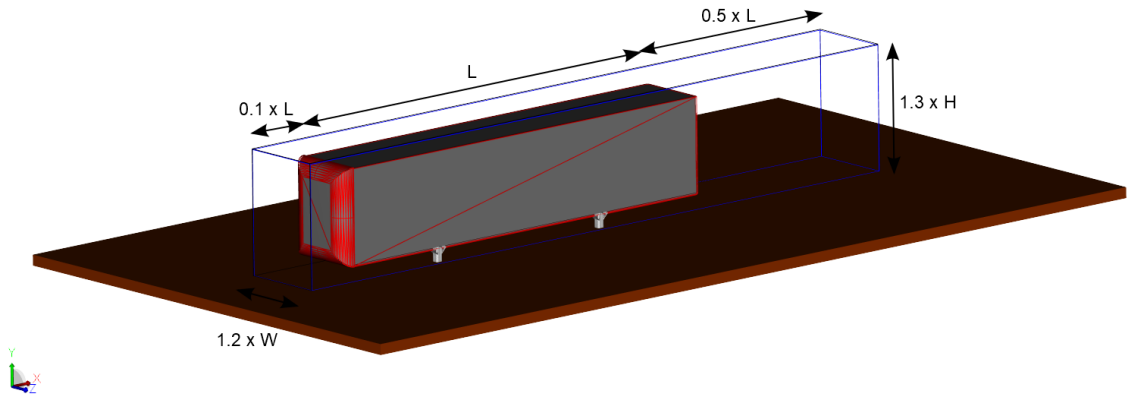


Figure 2.7: GETS offset and dimensions of the wakebox

In order to calculate the flow inside the simulation volume first boundary conditions must be defined. These are given in table 2.2. The front of the domain is assigned as velocity inlet. The back is defined as a pressure outlet. The left and right side, floor and ceiling of the domain are defined as a frictionless wall. Lastly the parts that are assigned as standard walls are the ground plate and the GETS model itself.

Table 2.2: Boundary conditions used in the simulation

Surface	Boundary Condition
Front	Velocity inlet
Back	Pressure outlet
Left	Frictionless wall
Right	Frictionless wall
Floor	Frictionless wall
Ceiling	Frictionless wall
GETS model	Wall
Ground Plate	Wall

2.2.4 Wall Model

The flow close to a wall will have different behaviour than that far away from it. In order to properly capture the behaviour of the boundary layer very fine meshes close to the wall are required. Because of the equal size of the voxels in all dimensions this would lead to a ridiculous amount of voxels. That is why PowerFLOW uses a turbulent wall-model Chen and Doolen (1998). This wall model which dynamically incorporates pressure gradients enables the accurate simulation with reduced near wall resolution Exa Corporation (2017b). In this model the velocity profile in the voxel closest to the wall is assumed to have a profile that is equal to that given by the Law of the Wall. This profile can be seen in figure 2.8.

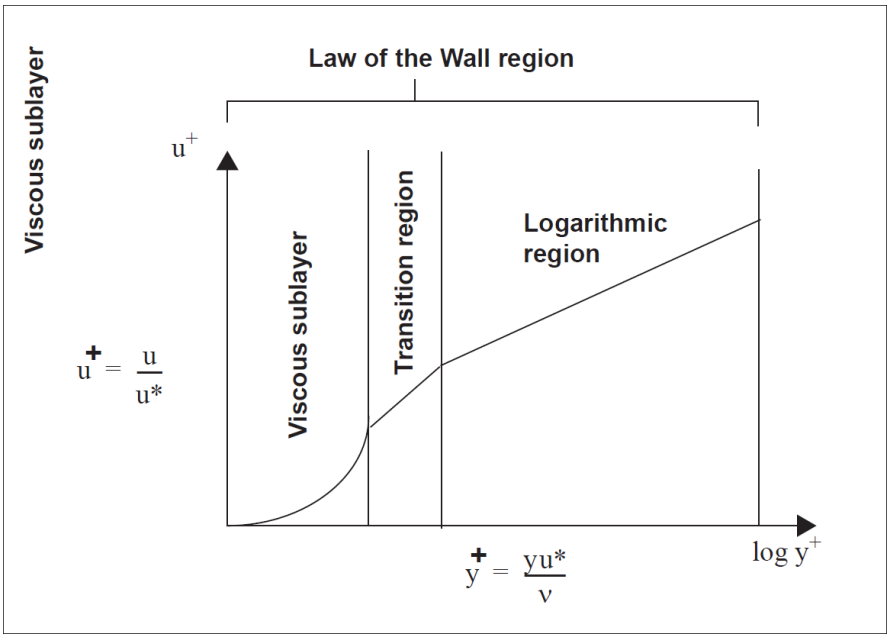


Figure 2.8: Turbulent Boundary Layer Profile Exa Corporation (2017b)

This velocity profile together with the wall model pressure gradient is then used to determine

the skin friction. The calculated skin friction is then implemented in the collision of particles with the wall. In order to use this wall model the values of y^+ must lie within a certain range for it to be valid. The y^+ on the baseline model are given in figure 2.9. From this it can be seen that the y^+ values lie between 0 and 90 which validates the use of wall models.

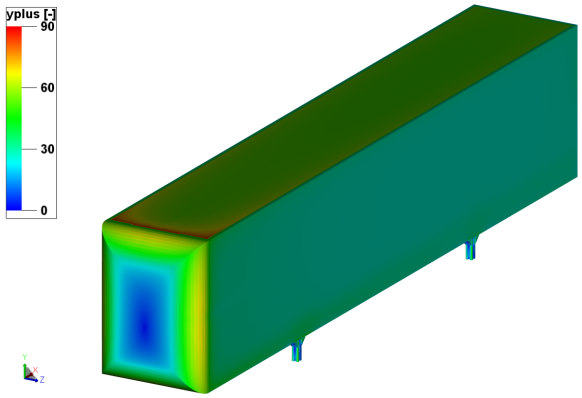
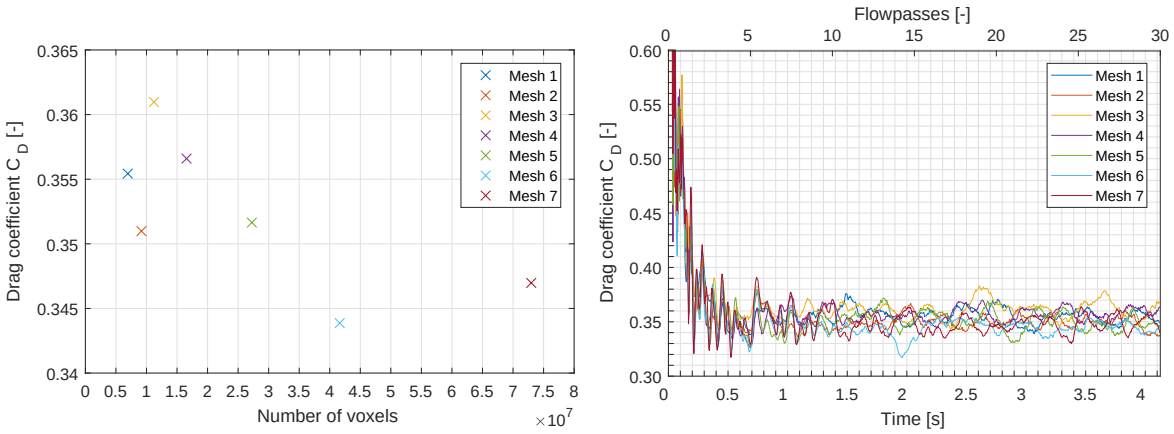


Figure 2.9: y^+ values on the surface of the baseline model

2.2.5 Mesh Sensitivity

As the simulation results are very dependent on the spatial resolution of the mesh it was decided to examine this sensitivity of the mesh. To do this 7 different meshes were created. The meshes all consist of 9 variable resolution (VR) levels. The way PowerFLOW works is that only the voxel size of the highest resolution level has to be specified after which next VR level gets double that voxel size which continues for all VR levels. The results of this mesh sensitivity study is given in figure 2.10(a). In general it can be seen that the drag coefficient decreases with increasing number of voxels and thus increasing resolution. Some exceptions can be seen. After the second mesh the drag coefficient jumps up again. For the finest mesh also a small jump can be seen. Since this jump is only 3 counts or less than 1% compared to the drag coefficient of the previous mesh it was decided to use mesh 6 for all the simulations. The parameters for this mesh are given in table 2.3.

Next to the spatial resolution it is also important that the simulation runs long enough such that the initial transient has passed and is avoided when taking the average measurements however with increasing runtime the computational costs also increase. Besides this the averaging window should be large enough such that average drag coefficient does not vary any more with increasing averaging window. In figure 2.10(b) the drag coefficient for the different meshes as a function of runtime is given. At the start all meshes show the initial transient behaviour which dies out after a certain time. Afterwards a periodic behaviour of the drag coefficient can be observed. For mesh 6 it was decided to start the averaging window at 1.8 seconds or 13 flowpasses based on the model length. The measurements are taken every 0.005 seconds which gives a acquisition frequency of 200 Hz. This window then continues until 3.6 seconds for a total averaging time of 1.8 seconds or 13 flowpasses. It was seen that further increasing the averaging window did not change the drag coefficient.



(a) Average drag coefficient as a function of mesh size

(b) Drag coefficient as a function number of runtime

Figure 2.10: Mesh Sensitivity

Table 2.3: Parameters for mesh 6

VR Level	Voxel Size [mm]	Geometry
0	320	Simulation Volume
1	160	-
2	80	-
3	40	-
4	20	-
5	10	-
6	5	-
7	2.5	Wakebox
8	1.25	GETS offset

2.3 Numerical Results

2.3.1 Single Model

In this section the results of the simulations of the single models will be presented. First the baseline configuration is analysed, after that the effect of different front edge radii is investigated and finally the effect of models applied with tails with varying angles is explained.

Baseline Configuration

The first configuration that was simulated is the baseline GETS model which has a front radius of 68 mm. The total drag coefficient of this configuration is 0.344, in figure 2.11 the drag contribution of each part of the model can be seen.

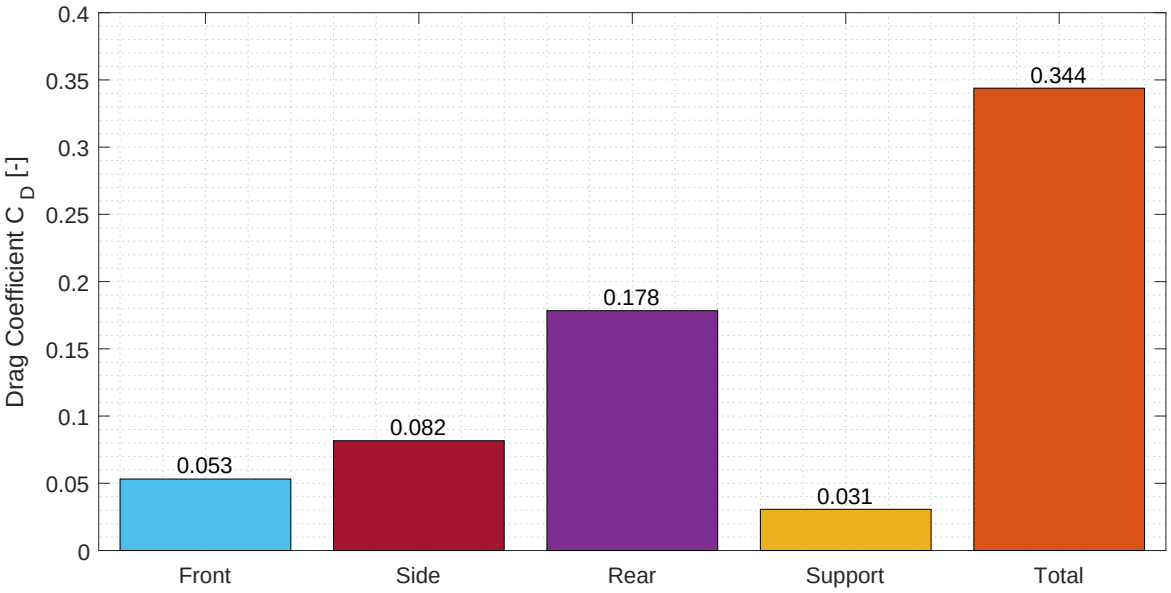


Figure 2.11: Numerical drag distribution for the baseline GETS model

Most of the drag is generated by the rear surface and only a small amount is generated by the front surface. This is different from a real life heavy duty vehicle where the front and rear surfaces generate equal amounts of drag Wood (2006). The reason for this difference is due to the rounded edges of the front surface. As the flow accelerates over them a low pressure region is created, which can be seen in figure 2.12. This causes a thrust force which relieves some of the drag that is created by the front stagnation surface where the flow stagnates.

Since most of the drag is caused by the rear surface it is very important that the flow in this wake region is simulated correctly. In figure 2.13 the wake is visualised. From the streamlines it is clearly visible that the wake is made up of a toroidal recirculation region in which a

vortex ring is present. This vortex ring was also found by Ortega et al. (2004) and Krajnović and Davidson (2003). The flow in this recirculation region is coming from the top, bottom and sides of the model. When it enters the wake it decelerates and is drawn into the toroidal vortex. There it reverses direction and stagnates on the rear surface of the model. After that it either stays in the recirculation region of it leaves the wake from the top or bottom.

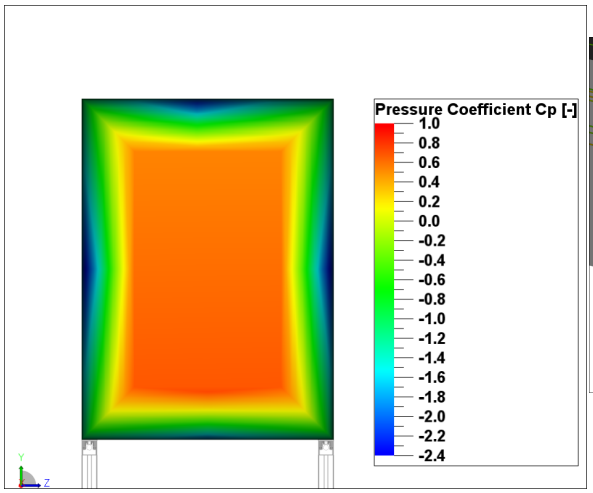


Figure 2.12: Numerical pressure coefficient over the front surface of the baseline model

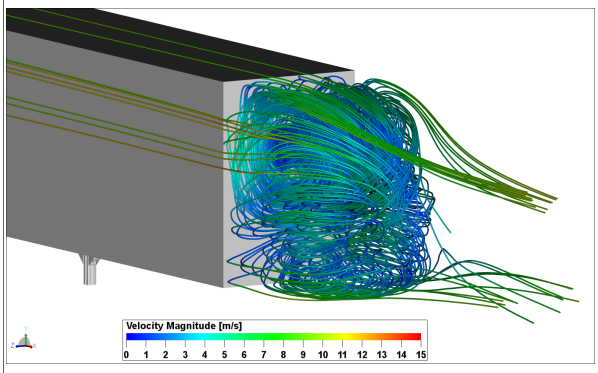
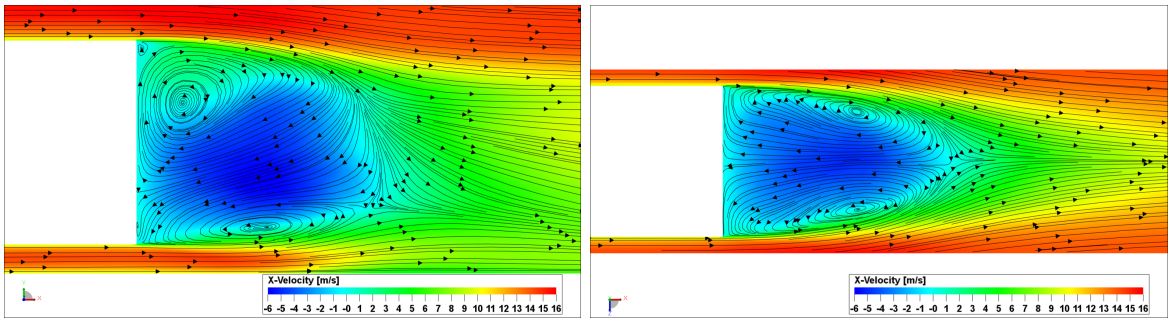


Figure 2.13: Numerical time-averaged and transient streamlines coloured by the velocity magnitude in the wake of the baseline model

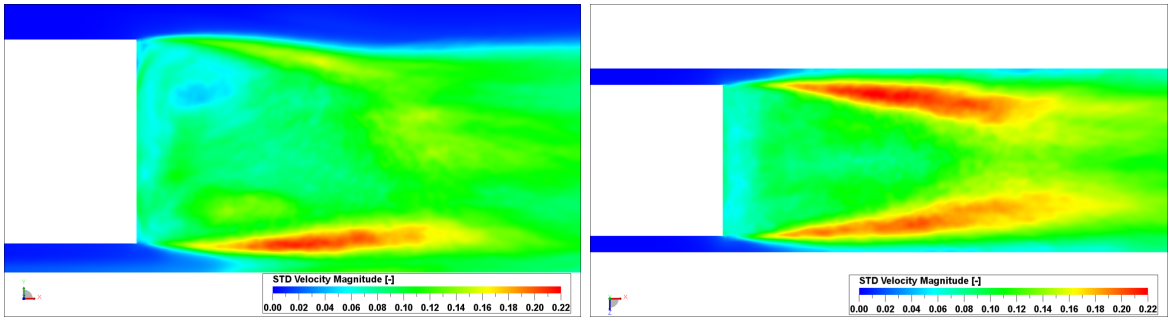
This wake can be seen in more detail in figure 2.14. Looking at the vertical centre plane (figure 2.14(a)) it can be seen that it consists of two vortices one at the top and one at the bottom. The size and strength of these vortices is not equal. The upper vortex is larger in size and located closer to the rear of the model. The lower one is more elongated and farther away from the rear surface. In general it can be said that the wake structure is very similar to that found by Van Raemdonck (2012) from Particle Image Velocimetry (PIV) measurements. In the horizontal centre plane (figure 2.14(b)) also two vortices can be seen. When comparing the left and right vortex it can be seen that these are equal in size and located at the same position. This is to be expected since the model is symmetric and was simulated at 0° yaw angle.



(a) Vertical centre plane z=0 (b) Horizontal centre plane y=0.5H

Figure 2.14: Numerical streamlines with contours of x-velocity in the wake of the baseline model

With the time averaged results discussed the fluctuations in the velocity field are shown next. These are given in figure 2.15 where the standard deviation of the velocity magnitude is shown. From the vertical centre plane (figure 2.15(a)) it can be seen that small fluctuations exist in the entire wake region. The highest fluctuations take place in the shear layer that exists at the bottom of the model. Next to this the upper shear layer and the arc region around the saddle point also show higher fluctuations compared to the wake region. The location in the wake which shows the lowest fluctuations is the centre of the upper vortex, located close to the rear surface of the model. From the horizontal centre plane (figure 2.15(b)) the regions of highest fluctuations are seen in the shear layer coming from the left and right of the model. Besides this the wake region shows fluctuations of the same order of magnitude that were found in the vertical centre plane.



(a) Vertical centre plane z=0 (b) Horizontal centre plane y=0.5H

Figure 2.15: Numerical contours of standard deviation of the velocity magnitude in the wake of the baseline model

Next to the velocity field the forces of the model also showed unsteady behaviour. Because of this it was decided to analyse them in the frequency domain. The results from this analysis are given in figure 2.16. From this figure it can be seen that the drag force varies with a

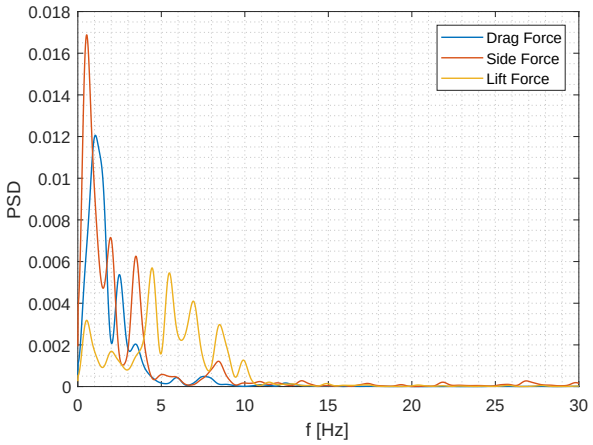
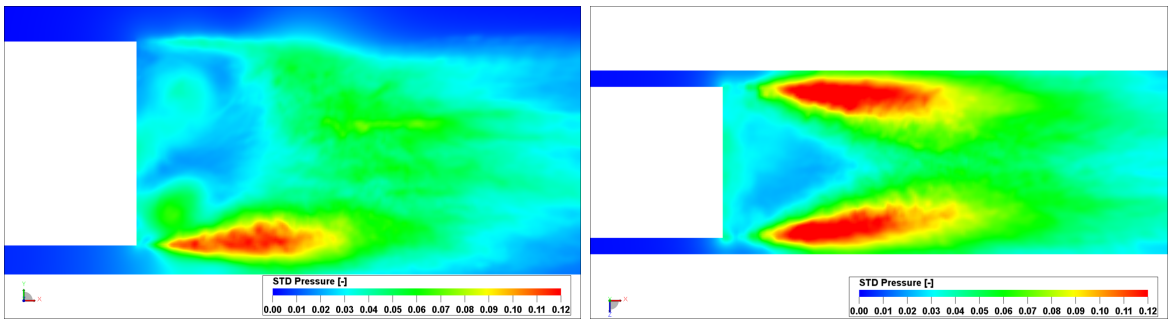


Figure 2.16: Numerical PSD of the unsteady forces of the baseline GETS model

Strouhal number of 0.073, which is very close to the values of 0.07 ,0.073 and 0.069 found by Khalighi et al. (2001) and Krajnović and Davidson (2001) from unsteady base pressure analyses. For the side and lift force multiple peaks of roughly the same magnitude can be seen. The side force fluctuates at a Strouhal number of 0.058 and 0.102 while the Strouhal numbers for the lift force are 0.130 and 0.160. These fluctuations are caused by the unsteady flow in the wake of the model which is visualised in figure 2.17 where contours of the standard deviation of pressure are shown.



(a) Vertical centre plane z=0

(b) Horizontal centre plane y=0.5H

Figure 2.17: Numerical pressure fluctuations in the wake of the baseline model

Looking at the vertical centre plane it can be seen that most of the fluctuations come from the shear layer at the bottom of the model. Next to this a region in the shape of an arc shows lower fluctuations. This region corresponds with the transient path that the saddle point follows. The fluctuations in the upper shear layer and vortex are rather low. This is not the case for the horizontal centre plane. The shear layers from the left and right represent the regions of highest fluctuations. Lower fluctuations can be seen downstream the shear layers. The region close to the rear surface of the model shows quite stable flow.

Effect of Front Edge Radius

Because drag distribution of the baseline GETS model did not resemble that of a real life heavy duty vehicle the front edge radius was varied to varied to see if these configurations had more representable front and rear drag contributions. The baseline radius of 68 mm was halved twice giving configurations with a 34 mm and 17 mm front edge radius. The drag distribution for these models can be seen in figure 2.18.

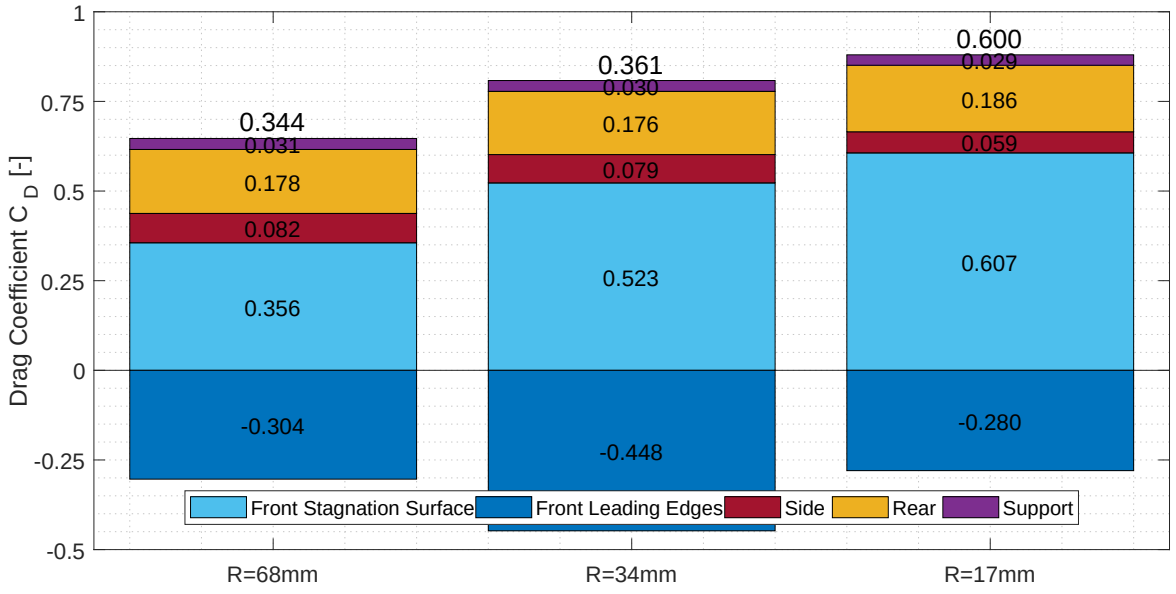


Figure 2.18: Numerical drag distribution for the GETS model with different front edge radii

When the radius is halved a first time the total drag increase is quite small. Only 17 counts are added compared to the baseline model. However the drag and thrust force generated by the front stagnation surface and front leading edges is quite different. Due to the larger stagnation surface its drag increases by 167 counts. Because of the sharper edges the flow is accelerated more which translates into a higher suction force. Compared to the baseline model 144 more thrust counts are generated. For the model with the smallest radius the total drag increase is quite dramatic, most of the drag increase is caused by the larger stagnation surface. Next to this 24 thrust counts are lost compared to the baseline model where it was expected that this configuration generated more thrust due to the sharper leading edges. This loss in thrust is due to the separation that occurred for this model which is visible in figure 2.19.

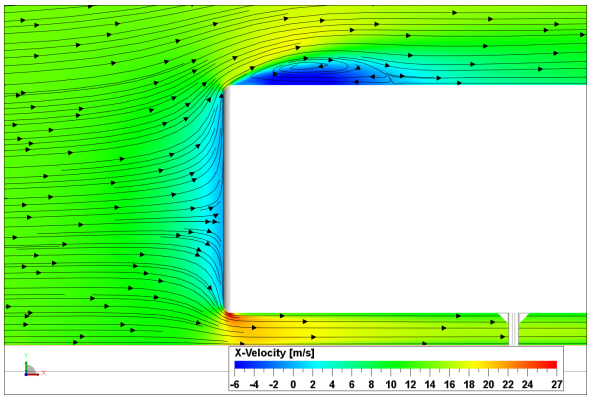


Figure 2.19: Numerical contours of x-velocity with streamlines indicating flow separation for the GETS model with R=17 mm z=0

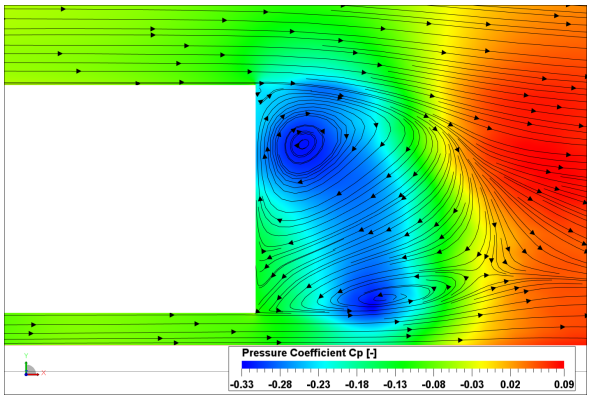


Figure 2.20: Numerical contours of pressure with streamlines in the wake of the model with R=17 mm z=0

Besides the changes in drag and thrust force generated by the front of the model some differences can be noticed when looking at the drag that is generated by the side and rear. When the radius increases the side drag decreases with 3 counts for the model with a radius of 34 mm and 23 counts for the model with the sharpest radius. This decrease is caused by the decreasing shear stress which in term is caused by the steepness of the gradient of the boundary layer. For decreasing front edge radii the steepness of the boundary layer also decreases explaining the reduced side drag. For the drag caused by the rear surface when the radius is halved a first time the drag is reduced by 2 counts. Due to the thicker boundary layer caused by the smaller radius of the front leading edges the pressure at the rear reduces and thus with it the drag caused by the rear. This behaviour was also seen by Van Raemdonck (2012) and Gheyssens (2016) from the results of a wind tunnel test and numerical simulation respectively. When the radius is halved a second time the drag of the rear increases by 8 counts. Also here a thicker boundary layer was seen however the wake structure, given in figure 2.20, is much smaller compared to the models with larger radii. Next to this the pressures of the two main vortices in the wake are lower and bottom vortex is located closer to the rear surface which is the reason for the drag increase.

Effect of Tails

The final set of simulations that were performed on the single model were those of the baseline model where tails with different angles were applied. The drag coefficients for these models are given in figure 2.21 where the drag is split up for the different components.

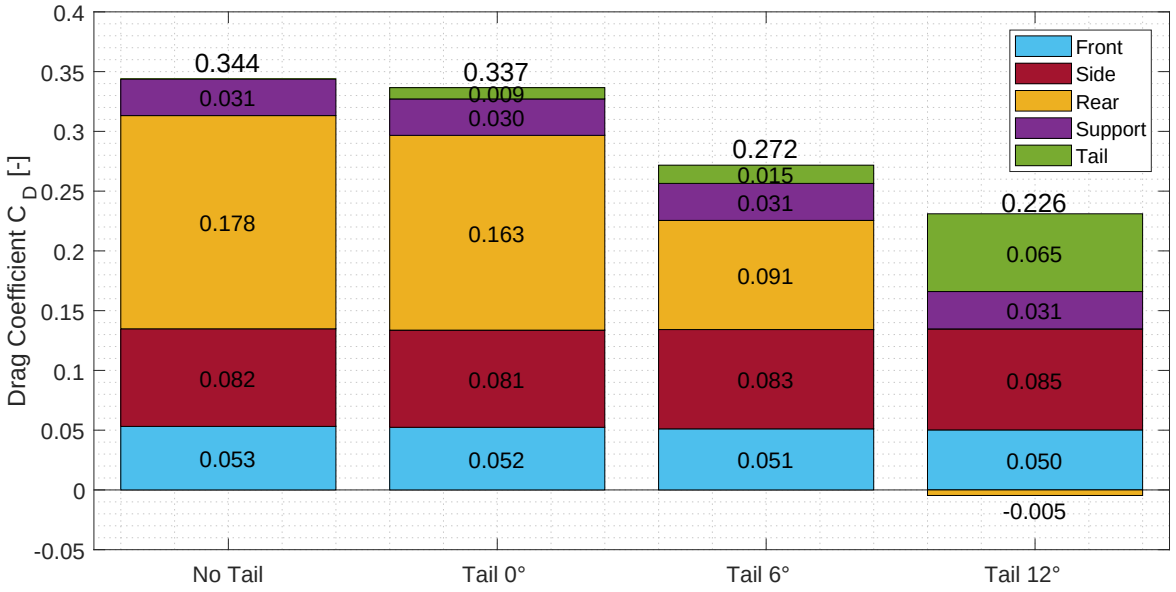
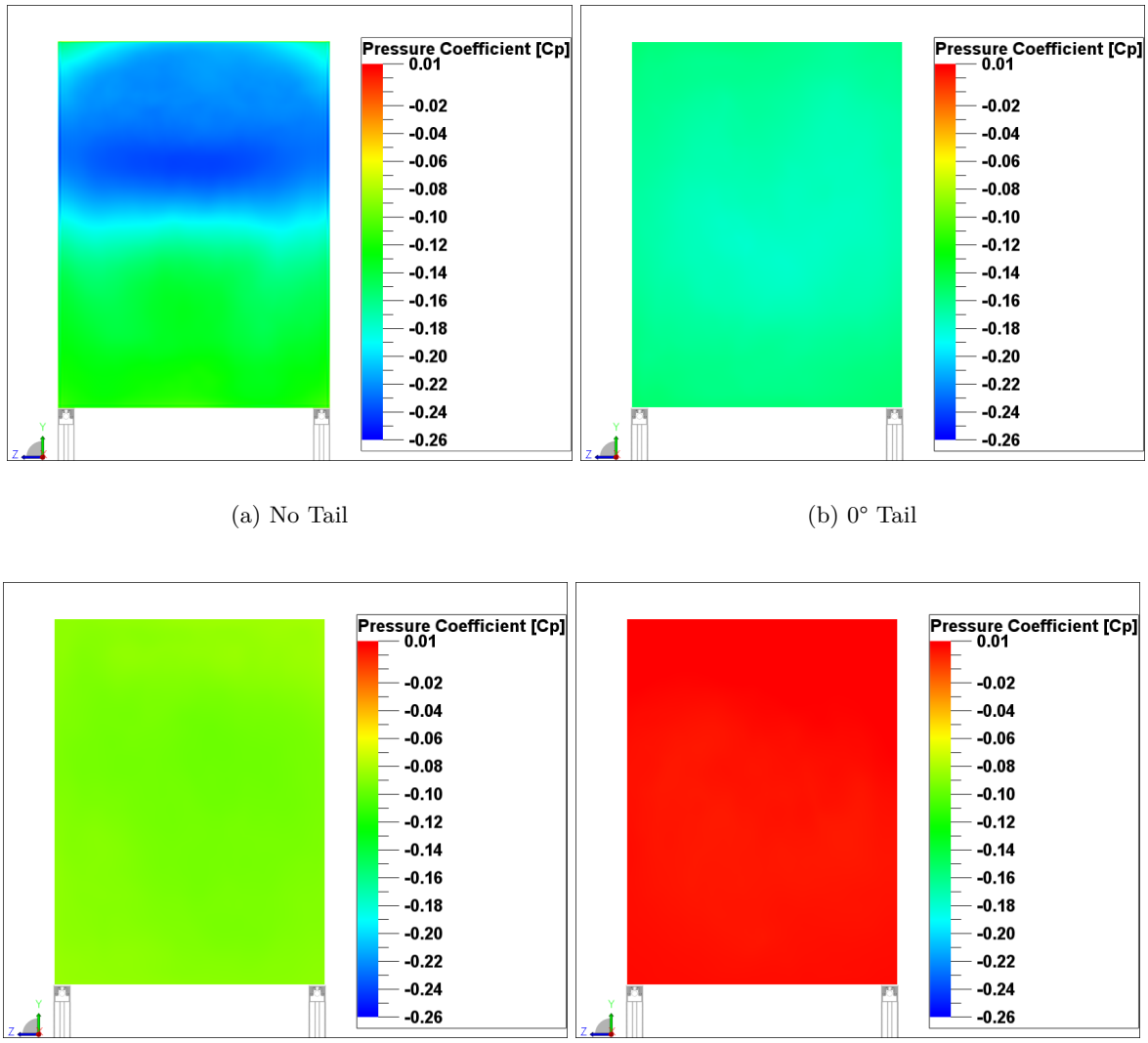


Figure 2.21: Numerical drag contributions for the baseline model with different tails

From the figure it can be seen that when a tail is applied the model loses drag. The higher the tail angle the greater the drag reduction. When the tail with an angle of 0° is applied the model loses 7 drag counts (2%). For a tail of 6° the drag loss is 72 counts (21%) and for the tail with the steepest angle of 12° the drag loss is 118 counts (34%). These tails were also tested by Gheyssens (2016) by performing numerical simulations on a full scale GETS model at a Reynolds number of 5.1×10^6. There drag reductions of 15 (5%), 87 (29%) and 124 drag counts (41%) for the tails with increasing angles were seen. In general it can be said that the tails are more effective at a higher Reynolds number. This is because at higher Reynolds numbers the pressure drag makes up more of the total drag so a reduction of the pressure drag, which is what a tail achieves, will result in a higher drag decrease. Van Raemdonck (2012) also tested the tail of 12° at a similar Reynolds number of 4.1×10^5. He reported a drag decrease of 90 counts (28%) however the length of the tail was 30% smaller than the one used in this study which explains the smaller drag decrease.

Most of the drag reduction comes from the rear surface of the model, for the model with the tail of 12° the rear surface even generates a small amount of thrust instead of drag. The drag reduction can be explained by looking at the pressure at the rear of the model which is given in figure 2.22.



(a) No Tail

(b) 0° Tail

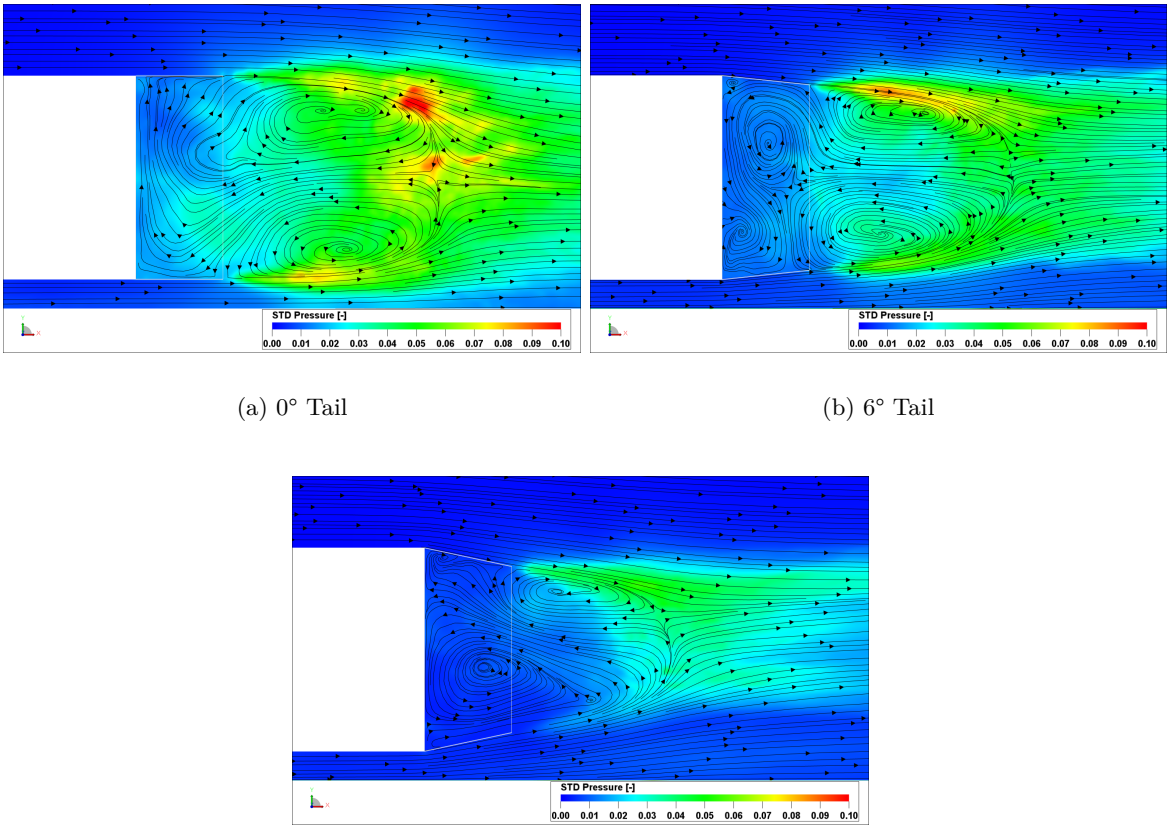
(c) 6° Tail

(d) 12° Tail

Figure 2.22: Numerical pressure distribution on the rear surface of the baseline model with different tails

From this pressure distribution it can be seen that adding a tail has a large effect on the distribution. The pressure of the model without a tail (figure 2.22(a)) is more negative on the top than it is on the bottom which can be explained by the closeness of the vortices seen in figure 2.14(a). When a tail of 0° is added the pressure distribution over the rear surface is almost constant. Compared to the model without a tail the pressure at the top is more positive while it is more negative at the bottom. This also explains the small drag decrease. When the tail angle is increased to 6° the negative pressure drops and becomes even more constant. For the last angle of 12° once again the negative pressure decreases and even becomes positive meaning that thrust is created next to this the distribution is now completely constant over the rear surface.

The addition of tails also has an effect on the flow field which can be seen by looking at the streamlines given in figure 2.23. When a tail of 0° is applied to the model the wake becomes



(a) 0° Tail

(b) 6° Tail

(c) 12° Tail

Figure 2.23: Numerical pressure fluctuations in the wake of baseline model where tails are applied

more symmetric. The flow outside the cavity still consists of two vortices. The upper one slightly extends into the cavity created by the tail. For the tail of 6° the wake becomes narrower. Next to the two vortices that can be found outside the cavity, inside this cavity also vortical structures are visible. The wake structure of the tail of 12° is again different. Due to the tail the recirculation region has become even narrower. The lower vortex has now fully extended into the cavity of the tail, the upper one is mostly defined outside this cavity.

Next to the time-averaged wake structure the tail also affects the unsteady flow indicated by the contours of pressure fluctuations. In general it can be seen that the fluctuations diminish with increasing tail angle. Lower fluctuations with a stepped tail were also reported by Khalighi et al. (2001). For the tail of 0° the highest fluctuations are coming from the upper and lower shear layer and the region around the saddle point of the recirculation region. The shear layer also contributes to most of the fluctuations of the model with a tail of 6°. The fluctuations in the lower shear layer are much lower as is the recirculation region itself. For the tail with the largest angle of 12° the fluctuations have diminished by

quite a lot. The only noticeable region is that of the upper shear layer. The effect of these fluctuations can also be seen in figure 2.24 were the PSD of the drag and side-force is given for the models applied with the varying tails. From the drag force it can be seen that for the

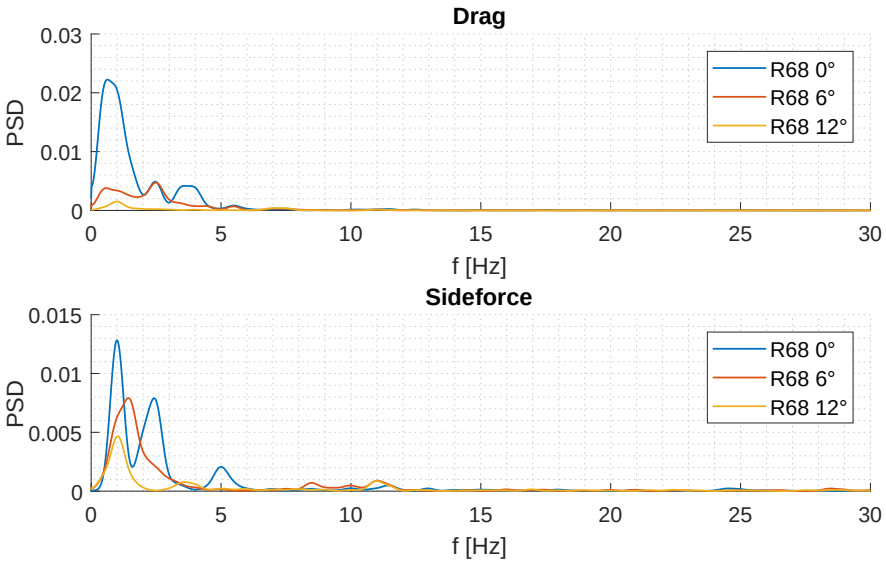


Figure 2.24: Numerical PSD of the drag and side force for the baseline model with tails

tail of 0° and 6° a peak exists at a Strouhal number of 0.071 no peak can be seen for the tail of 12°. The side force also shows a peak at the same Strouhal number for the model with a tail of 0°. For the other models no peak at this number can be seen although peaks at lower frequencies can be seen which for the tail of 12° shows a lower amplitude.

2.3.2 Platoon

Now that the single models have been discussed the platoon configurations are next. The platoons were simulated at three intervehicle distances of 0.10, 0.45 and 0.91 the vehicle length.

Intervehicle distance: 0.10 s/L

The first intervehicle distance at which the platoon was simulated was 0.10 times the vehicle length. Three simulations were performed at this distance namely the baseline platoon where both models had a front edge radius of 68 mm, one where the trailing model had a front edge radius of 17 mm and the baseline platoon where the trailing model had a misalignment of 10 mm in vertical direction. For the last simulation the trailing model was placed lower because the same misalignment was seen during the experimental campaign. The relative and absolute drag results for these simulations can be seen in figure 2.25. The bars indicate the relative drag coefficient which is scaled by the drag coefficient of the isolated model (C_{D_i}). C_{D_p} stands for the drag coefficient of the model when it is in the platoon configuration. The values above each bar indicate the absolute drag coefficient of each model.

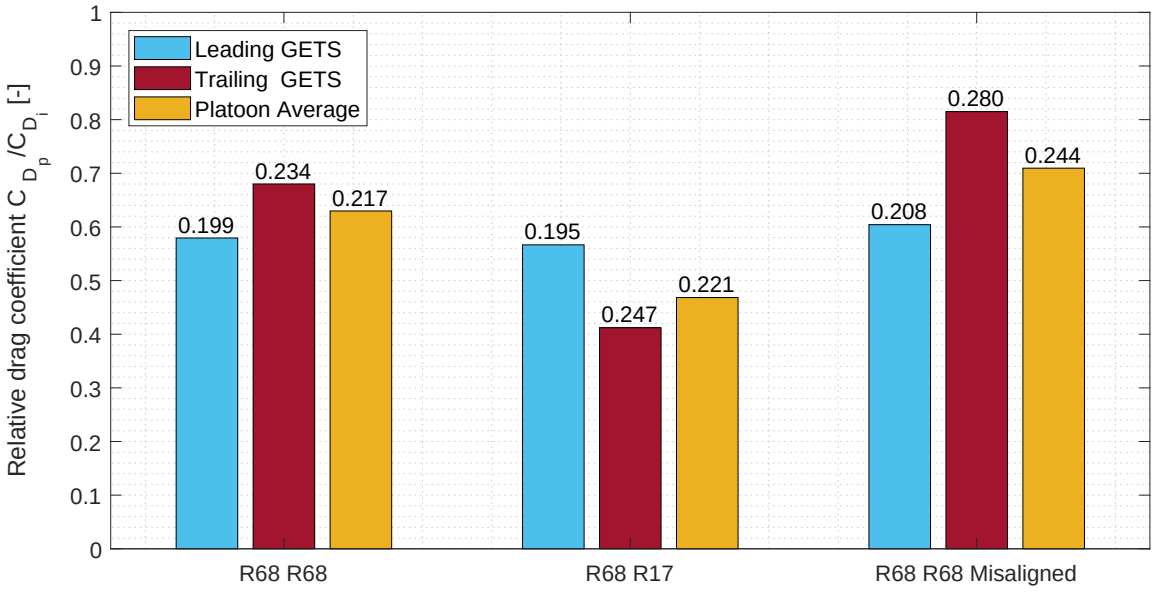


Figure 2.25: Numerical relative and absolute drag coefficient for the platoons at 0.10 s/L

Baseline configuration: R68-R68 From the figure it can be seen that both vehicles benefit from this platoon configuration. The gains are 42%, 32% and 37% for the leading, trailing and platoon average respectively. In this configuration the leading model benefits more than the trailing model. This was also found by Hammache et al. (2002). The reason for this is that when the models are in a platooning configuration the leading model experiences a drag decrease with most of it coming from the rear surface. Because most of the drag in the isolated case also is generated by the rear surface any drag decrease to the rear surface will give a larger gain than to any other part.

A breakdown of the differences in drag between the isolated model and the models in the platoon is given in figure 2.26. The model is split up into four parts namely the front, side and rear surface and the supports. For the leading model it can be seen that most of the drag decrease comes from the rear surface and for the trailing model the front surface loses the most amount of drag. This is to be expected because of the way the pressure fields from the rear and front influence each other. Due to the presence of the high stagnation pressure on the front of the trailing vehicle the low pressure of the wake of the leading vehicle is increased. The same is true for the pressure on the front of the trailing vehicle which is reduced because of the low wake pressure. The effect of this pressure increase and reduction for both the rear surface of the leading vehicle and the front surface of the trailing vehicle can be seen in figures 2.27 and 2.28. Looking at the pressure coefficient of the rear surface of the leading vehicle in figure 2.27(a) it can be seen that overall the pressure has increased compared to the isolated case which explains the drag decrease. The pressure increase is most pronounced at the centre of the model and drops off at the edges. For the pressure at the front of the trailing model shown in figure 2.27(b) the opposite is true. The high stagnation pressure is greatly reduced, the pressure coefficient is mostly negative. Next to this it can also be seen that the peak at the top of the model is greatly reduced whereas a

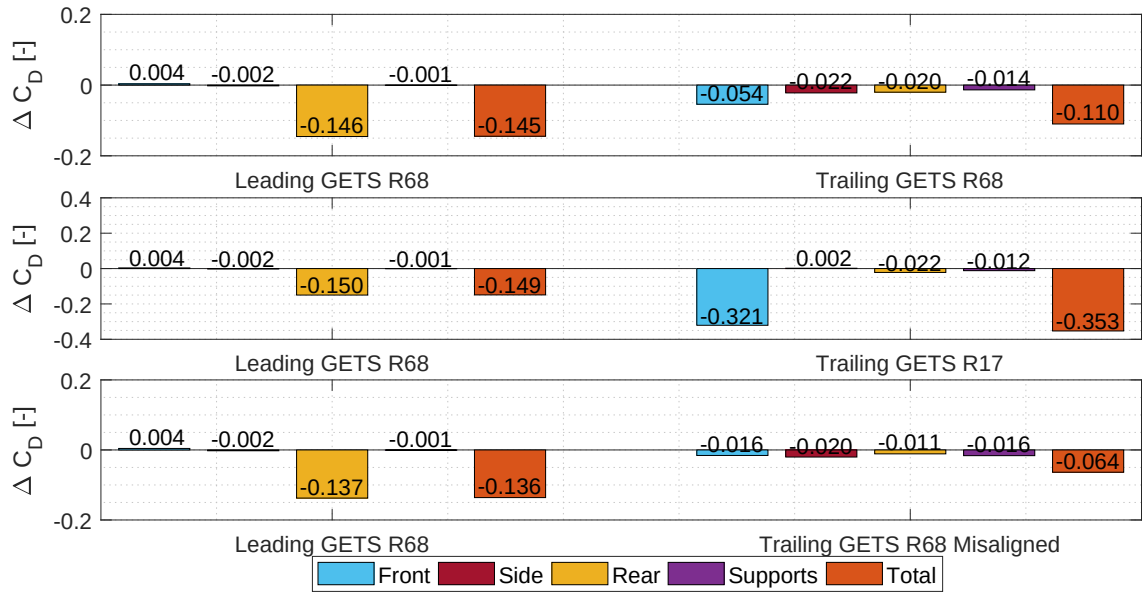
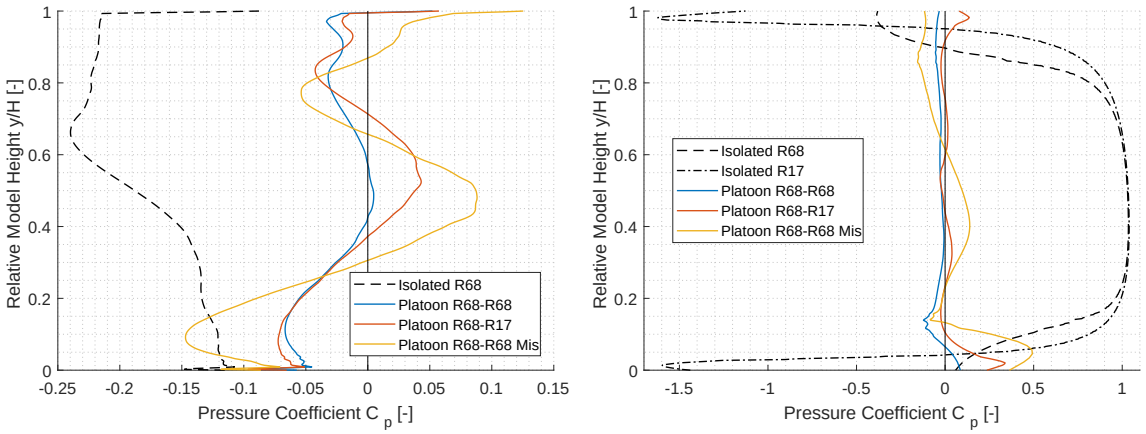


Figure 2.26: Numerical drag differences with respect to the single model for the leading and trailing model in a platoon at 0.10 s/L intervehicle distance

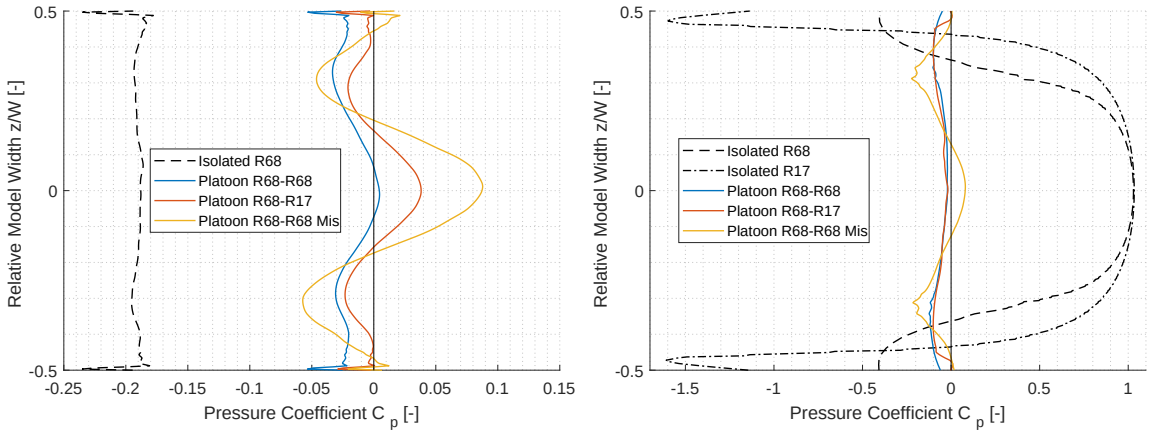


(a) Rear surface leading model

(b) Front surface trailing model

Figure 2.27: Numerical pressure coefficient over the surfaces of the platoon at 0.10 s/L z=0

new smaller peak is formed in the bottom. For the pressure over the horizontal centre line a similar story holds. The pressure at the rear of the leading model has been greatly reduced and has changed from being almost constant to having three distinct peaks. At the top and bottom the peaks indicate a small suction while in the centre a positive pressure peak can be found. For the front of the trailing model also here the suction generated by the rounded edges of the isolated model can no longer be observed. Also here two small suction peaks can be seen together with a lowered stagnation pressure in the centre of the model.



(a) Rear surface leading model

(b) Front surface trailing model

Figure 2.28: Numerical pressure coefficient over the surfaces of the platoon at 0.10 s/L intervehicle distance y=0.5H

The altered pressure can be explained by looking at the flow inside the gap which will be done next. The general flow is shown by figure 2.29. From this figure it can be seen that

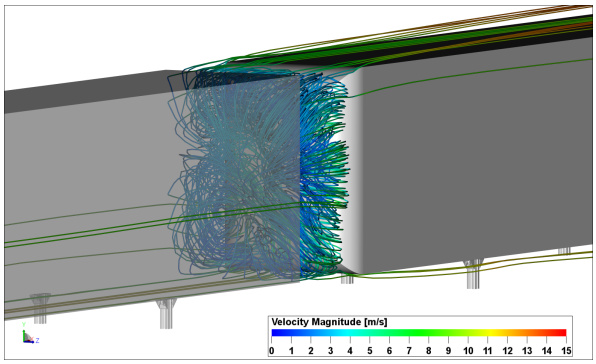
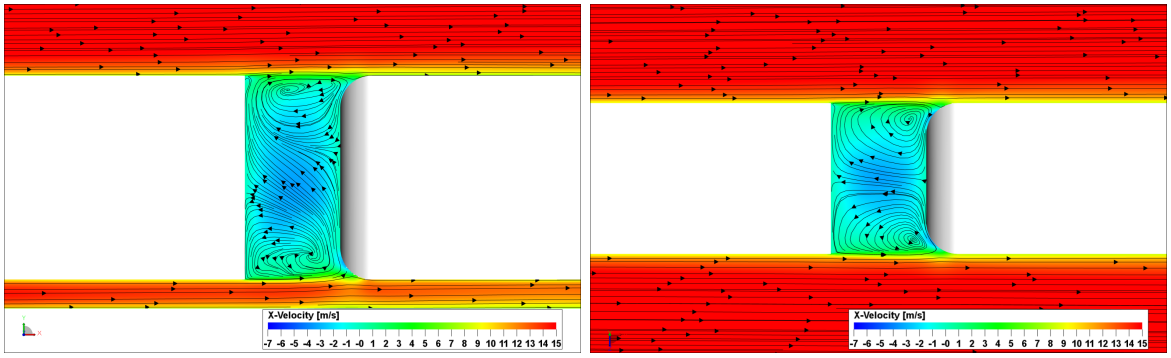


Figure 2.29: Numerical time-averaged and transient streamlines coloured by the velocity magnitude in the gap of the R68-R68 platoon at 0.10 s/L

most of the flow is entering the gap from the bottom of the leading model. As it enters the gap it decelerates and rolls up into the lower part of the toroidal vortex that exists in the gap. The flow not contained in this vortex moves upward where it stagnates on the surface of the leading model after which it enters the top part of the vortex and leaves the gap via the rounded edge of the trailing model where it accelerates.

To better explain the change in pressure the flow structure is studied in more detail. A visualisation can be seen in 2.30. From figure 2.30(a) it can be seen that the flow in the gap follows and S-shaped path. At the bottom the flow either stagnates on the bottom rounded edge creating high pressure or it enters the bottom vortex which creates a low pressure region, the flow that is not contained in this vortex continues its way up where

some of it stagnates on the rear surface of the leading model creating higher pressure. The rest of the flow moves further upward where it either enters the low pressure top vortex or stagnates on the rounded edge and leaves the gap. From the horizontal centre plane two counter rotating vortices can be seen the location of these vortices corresponds with the suction peaks that were found on the surfaces of the leading and trailing model. The higher pressure peaks can be explained by the flow that stagnates in between these two vortices.



(a) Vertical centre plane z=0 (b) Horizontal centre plane y=0.5H

Figure 2.30: Numerical flow structure in the gap of the R68-R68 platoon at 0.10 s/L with contours of x-velocity

The unsteady forces were also analysed for this configuration the platoon has little to no effect on the leading model but it does affect the trailing model. In figure 2.31 the PSD of the drag and side force is given for the three tested configurations at this intervehicle distance. A peak in the drag of the baseline platoon can be seen at a Strouhal number of 0.102, its amplitude is only slightly higher than that of the single model. This cannot be said for the sideforce. Here a peak can be seen at a Strouhal number of 0.132 with an amplitude about 3.5 times higher than that of the single model. These higher unsteady forces can be explained by looking at the pressure fluctuations which are given in figure 2.32. From figure 2.32(a) it can be seen that the highest fluctuations occur at the top, bottom and middle of the model. The pressure fluctuations are caused by the flow entering the gap from the bottom, leaving the gap from the top and stagnating in the centre of the model. From the horizontal centre plane the highest pressure fluctuations can be seen at the sides of the model as the flow leaves the gap using this path.

Effect of front edge radius: R68-R17 When the front edge radius of the trailing model is changed from the bluntest to the sharpest one of 17 mm the gains for the platoon become 43% for the leading model, 59% for the trailing model and 53% on average. In this case the trailing model gains the most from the platoon configuration which was also found by Hammache and Browand (2004). That is because most of the drag for the isolated model was generated by the front, which in the platoon loses the most drag shown in figure 2.26. For the trailing model the gain is slightly higher compared to the baseline platoon. This can be explained by looking at the pressures over the rear and front surfaces of the leading and trailing model given in figure 2.27 and 2.28. For the leading model the pressure over

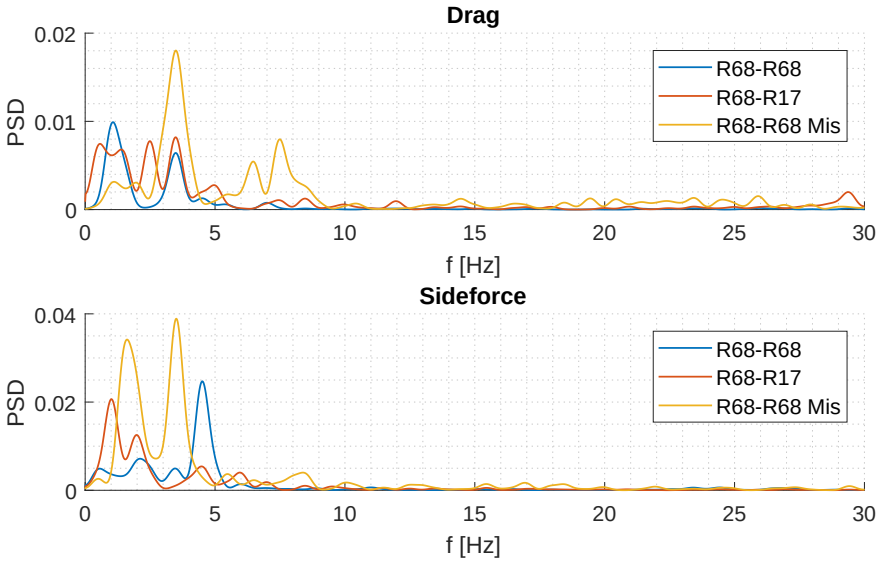
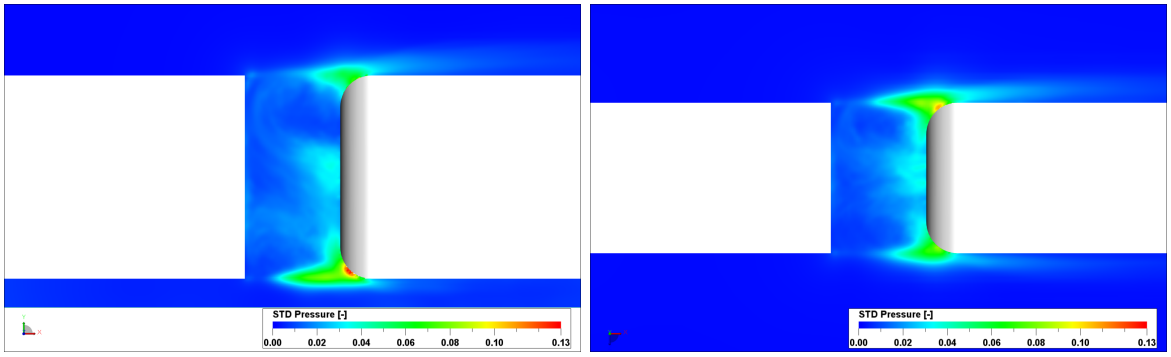


Figure 2.31: Numerical PSD of the drag and side force of the trailing model in the platoon at 0.10 s/L



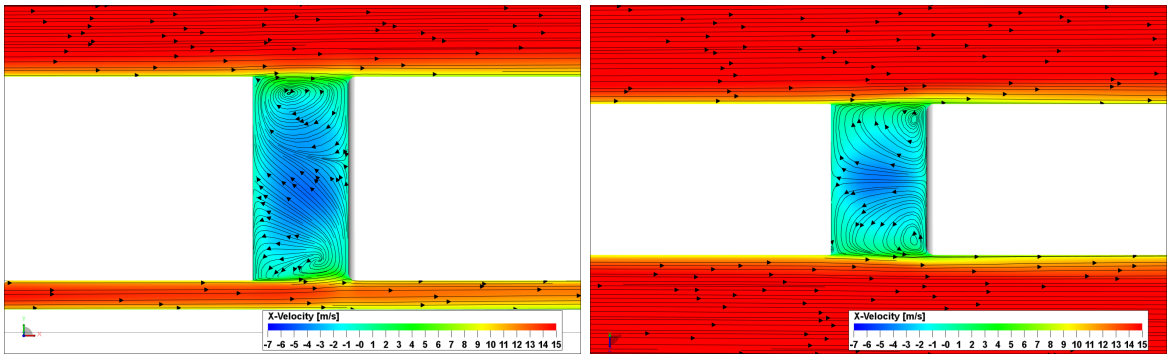
(a) Vertical centre plane

(b) Horizontal centre plane

Figure 2.32: Numerical pressure fluctuations in the gap of the R68-R68 platoon at 0.10 s/L

the rear surface is increased everywhere, in the middle the pressure is even positive meaning that in this region thrust is created. For the front surface of the trailing model the pressure is decreased everywhere but the rounded edges of the model where the pressure is increased due to the stagnation of the flow. Because the pressure in this region is higher compared to the isolated vehicle the adverse pressure gradient is greatly reduced meaning that the flow does not separate. This can also be seen in figure 2.33 where the flow field in and around the gap is visualised. For the pressure over the horizontal centre line much of what holds for the vertical centre line is also true here. The pressure over the rear surface of the leading model has changed from being constant to having three peaks. Two of them can be related to the vortices that exist in the gap while the other one is caused by the stagnation of the flow. The magnitudes of the suction peaks are smaller than those of the baseline platoon while the high

pressure stagnation peak is bigger. The pressure over the front of the trailing model is not altered much compared to the baseline platoon.



(a) Vertical centre plane z=0 (b) Horizontal centre plane y=0.5H

Figure 2.33: Numerical flow structure in the gap of the R68-R17 platoon at 0.10 s/L with contours of x-velocity

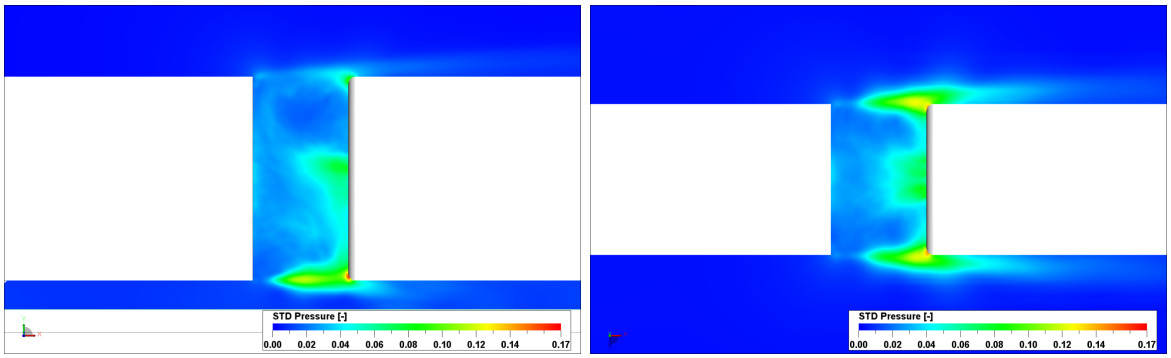
A similar flow structure to that of the baseline platoon can be seen in the gap. However because of the sharper edges the vortices are better contained in the gap. Another effect of the sharper front edges is that the flow circulating in the gap needs to make a sharper turn to stay in the gap. Because of this the magnitude of the vertical velocity close to the front surface of the trailing model increases which in turn leads to an increased magnitude of the reversed flow in the middle of the gap. This increased velocity gives a lower pressure in the middle of the gap and a higher pressure when it stagnates on the rear surface of the leading model.

Looking the unsteady forces for this configuration given in figure 2.31 it can be seen that the drag force fluctuates at the same frequency than the baseline platoon. The amplitude is slightly higher. The opposite is true for the sideforce, the peak at the Strouhal number of 0.132 has been greatly reduced. The reason for this can be given by looking at the pressure fluctuations which are presented in figure 2.34.

From this it can be seen that the pressure fluctuations are in the same location as was the case for the baseline platoon. Because of the less streamlined model the magnitude of these fluctuations are higher. The fact that the fluctuation in the sideforce are less compared to the baseline platoon can also be explained by the model. Due to the sharper front edge radius less area is exposed to the sides which means that the pressure has a smaller effect on the sideforce.

Effect of vertical misalignment: R68-R68 Misaligned The last simulation that was performed at this intervehicle distance is the one of the baseline platoon where the trailing model is placed 10 mm lower than the leading one. This was done because during the experiment a similar misalignment was noticed which proved very difficult to get rid off.

From figure 2.25 it can be seen that the gains for the leading model are similar to



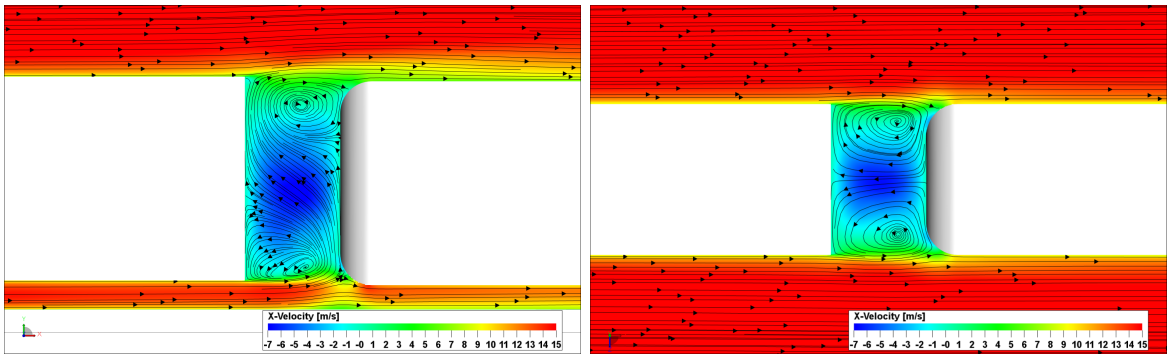
(a) Vertical centre plane z=0 (b) Horizontal centre plane y=0.5H

Figure 2.34: Numerical pressure fluctuations in the gap of the R68-R17 platoon at 0.10 s/L

that of the aligned platoon (40%), the trailing model suffers more from the misalignment. Its drag reduction is only 18% compared to the 32% of the aligned platoon. The greatest loss in drag reduction is found in the front part. For the leading model the small loss in drag reduction can be found in the rear surface. This loss in drag reduction can be explained by looking at the pressure distribution over the rear and front surface of the leading and trailing vehicle given in figure 2.27 and 2.28. For the leading model the pressure over the rear surface is higher everywhere but the lower part. Three distinct peaks in the pressure distribution can be seen, two of low and one of high pressure near the middle of the model. Due to the misalignment of the trailing vehicle these peaks are slightly shifted compared to the aligned platoons. The magnitude of the pressure peaks is also bigger than those of the aligned platoons. The location of these pressure peaks corresponds with the location of the two vortices and the stagnation point which are visible in figure 2.35. The reason for the pressure peaks of higher magnitude is because of the misalignment more flow coming from the underbody of the leading model is deflected into the gap. This causes the flow in the gap to be faster which leads to lower pressures for the vortices and a higher stagnation pressure on the rear surface of the leading model.

Looking at the pressure over the front surface of the trailing model it can be seen that the stagnation pressure in the middle of the model has been greatly reduced but not as much compared to the aligned platoon. The suction at the top is reduced compared to the isolated model but less than the aligned platoon. At the bottom of the model the suction has completely vanished and a high pressure peak is visible. This comes form the fact that when the model is lowered the bottom edge is more exposed to the underbody flow from the leading vehicle. This flow then stagnates on this front edge and creates a high pressure region visible in figure 2.35. The higher stagnation pressure in the middle and lower vortex pressure at the top can be explained by the increased amount of flow entering the gap from the bottom which leads to an increased flow velocity in the gap.

The effect of the misalignment can also be seen in the pressure on the horizontal centre line given in figure 2.28. The shape of the pressure on the rear of the leading model is

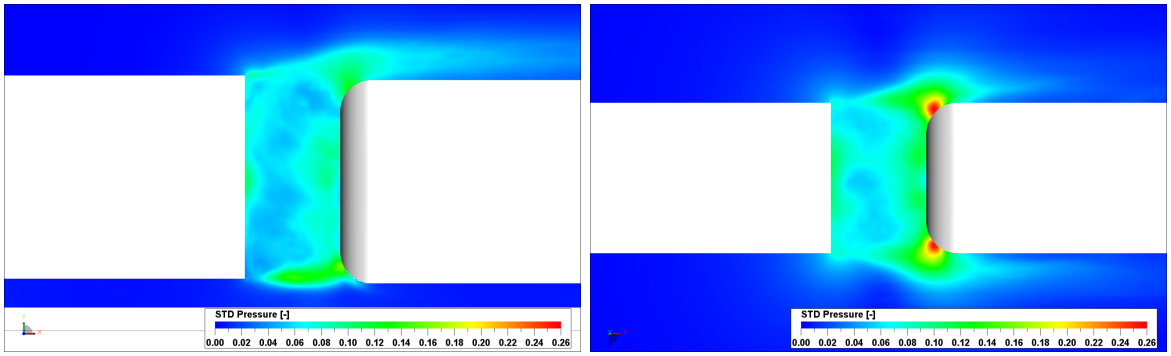


(a) Vertical centre plane z=0 (b) Horizontal centre plane y=0.5H

Figure 2.35: Numerical flow structure in the gap of the R68-R68 vertical misaligned platoon at 0.10 s/L with contours of x-velocity

comparable to that of the other platoons only the extrema are much bigger. This is because of the amount of flow that is deflected into the gap which causes a lower pressure in the vortices and higher stagnation pressure. For the pressure on the front of the trailing vehicle the same can be said.

For this configuration the magnitude of the unsteady forces is much higher than the previous two. The amplitude of the drag force which can be seen in figure 2.31 is about three times a high as the baseline platoon. For the sideforce the amplitude and frequency have changed, the amplitude has increased about one and half and the peak is located at a Strouhal number of 0.102. These higher fluctuations in force are caused by the pressure



(a) Vertical centre plane z=0 (b) Horizontal centre plane y=0.5H

Figure 2.36: Numerical pressure fluctuations in the gap of the R68-R68 vertical misaligned platoon at 0.10 s/L

fluctuations given in figure 2.36. Overall the pressure fluctuations are much higher, this can be seen especially in the horizontal centre plane.

Intervehicle distance: 0.45 s/L

For the second platoon configuration the models were places at an intervehicle distance of 0.45 times the vehicle length. Three simulations were performed at this distance, one of the baseline platoon, one where the trailing model had the sharp front edge radius of 17 mm and one where the leading model had a tail of 12°. The relative and absolute drag results of these platoon are given in figure 2.37. The bars indicate the relative drag reduction compared to the isolated model while the values above each bar indicate the absolute drag of the model.

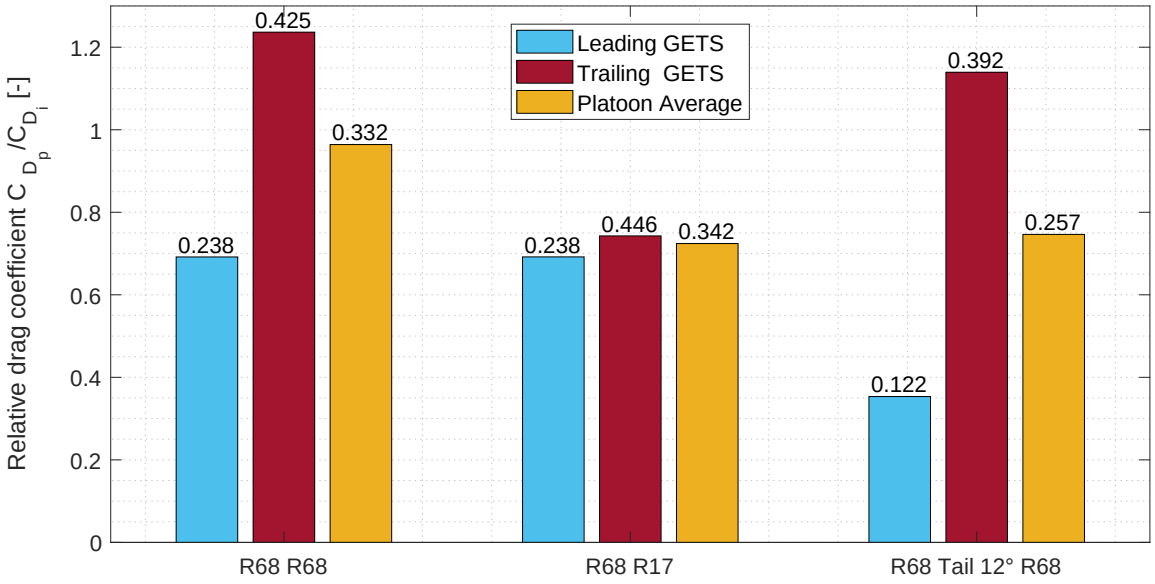


Figure 2.37: Numerical relative and absolute drag coefficient for the platoons at 0.45 intervehicle distance

Baseline Platoon: R68-R68 For the baseline platoon it can be seen that the trailing model benefits from the platoon configuration, 31% drag reduction compared to the isolated model. For the trailing model however the drag is 24% higher. Similar behaviour of vehicles in a platoon was observed by Rajamani (2006) and Pagliarella (2009) for a platoon of Ahmed bodies through experiments and numerical simulations respectively. Gheyssens (2016) also saw this behaviour for a 3-vehicle platoon of GETS models although the drag increase of the trailing model was only 3%. The drag decrease of the leading model however was slightly higher (38%).

From figure 2.38 where the drag differences for the various parts of the model are shown it can be seen that most of the drag decrease for the leading model comes from the rear surface. For the trailing model the part that causes the highest drag increase is the front. The reason behind this drag decrease and increase for the leading and trailing model can be explained by looking at the pressure over the rear and front surfaces given in figure 2.39 and 2.40. For the pressure on the rear surface of the leading model plotted over the vertical centre line in figure

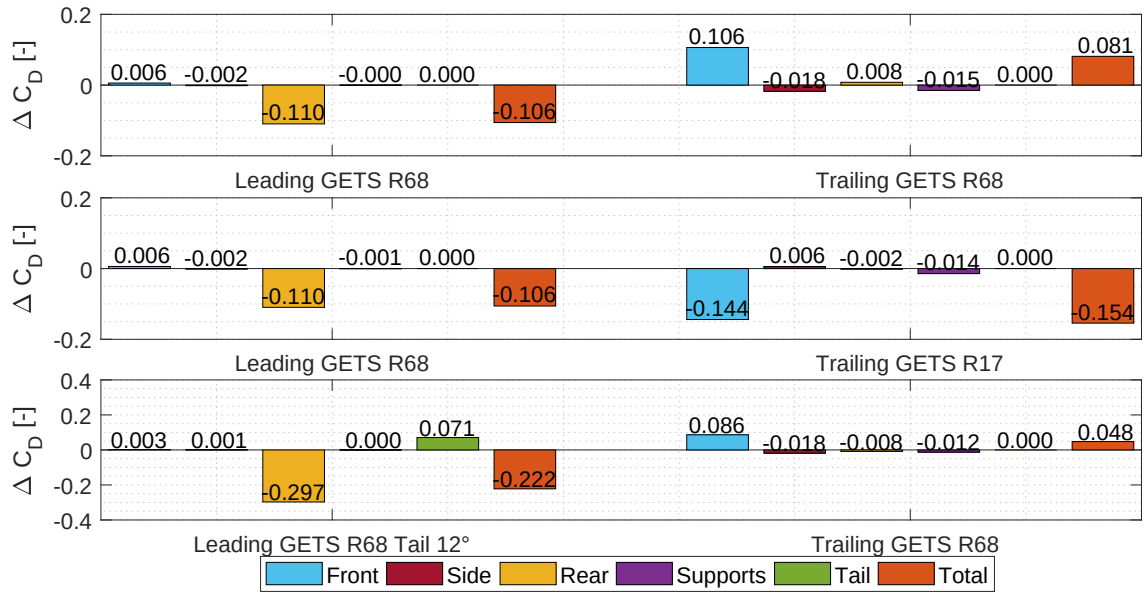
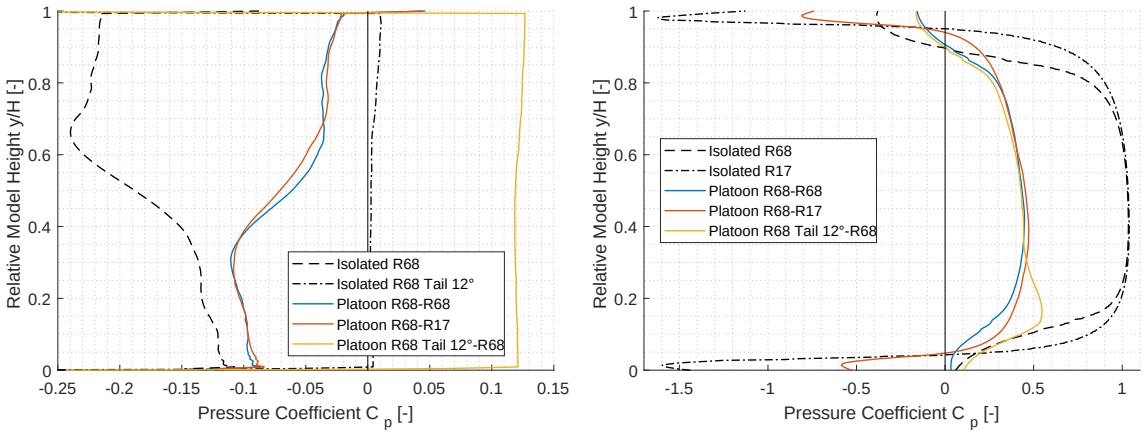


Figure 2.38: Numerical drag differences with respect to the single model for the leading and trailing model in a platoon at 0.45 s/L

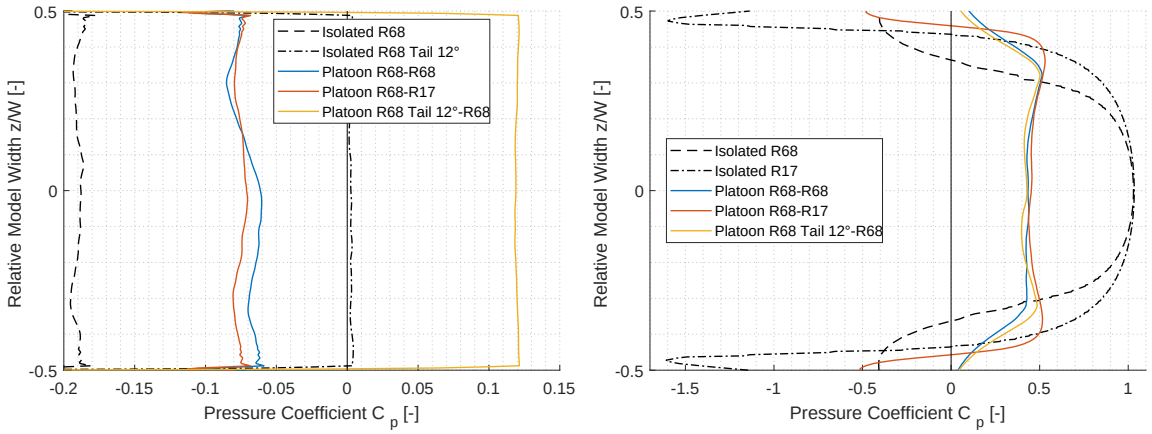


(a) Rear surface leading model

(b) Front surface trailing model

Figure 2.39: Numerical pressure coefficient over the surfaces of the platoon at 0.45 s/L z=0

2.39(a) it can be seen that it is increased everywhere compared to the isolated model. The increase is most pronounced at the top of the model. The pressure distribution on the front surface of the trailing model is also quite different compared to that of the isolated model. At the top the suction by the rounded edges has been greatly reduced, next to this the pressure at the bottom and on the stagnation surface has been decreased. The pressure over the horizontal centre line, given in figure 2.40, also shows quite some differences compared to that of the isolated model. First of all it must be noted that the pressures on the rear



(a) Rear surface leading model

(b) Front surface trailing model

Figure 2.40: Numerical pressure coefficient over the surfaces of the platoon at 0.45 s/L y=0.5H

surface, fig 2.40(b), are all quite symmetric. This was expected since the simulations were all performed at 0° yaw. The pressure of the platoon has seen a great increase compared to the isolated model. For the pressure on the front of the trailing model it can be seen that the suction peaks at the right and left edge are completely vanished in the platoon configuration. The pressure on the stagnation surface has been reduced and has a more constant value.

From this pressure analysis one can now explain the differences in drag for the leading and trailing model. For the leading model the negative pressure is lower everywhere which explains the lower drag. For the trailing model the reasoning is not as straightforward. On one hand a decreased stagnation pressure was observed which decreases the drag. On the other hand the suction peaks on the rounded edges were decreased for the top of the model and vanished completely for the left and right front edge. These two phenomena determine whether the model experiences a drag increase or decrease and at this distance a drag increase is the result.

Now that the drag increase and decrease have been explained by the pressures, the flow field in the gap will be analysed in more detail. In figure 2.41 streamlines coloured by the velocity magnitude are shown in the gap between the two models. The flow that is coming from the trailing model enters the gap from the top bottom and sides where part of it rolls up and decelerates creating a toroidal recirculation region. The flow in this recirculation region moves toward the centre of the model where part of it stagnates on the rear surface of the trailing model. The rest of the flow continues its way and either stays trapped in the recirculation region or it leaves the recirculation region. Subsequently the flow that leaves the recirculation region stagnates on the front surface or flows over the rounded edges of the trailing model where it is accelerated and continues its way downstream.

The flow field in the gap is also visible in figure 2.42 which will be used to explain the pressures that were described in the previous paragraphs. Looking at the wake of the leading model

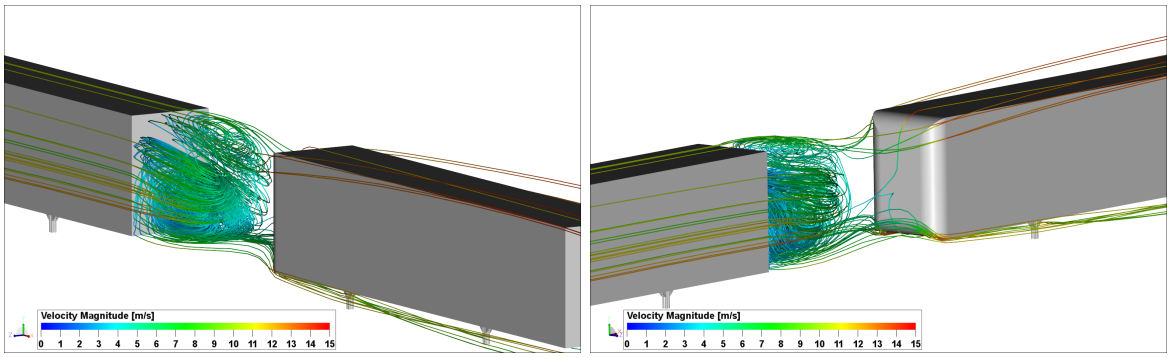
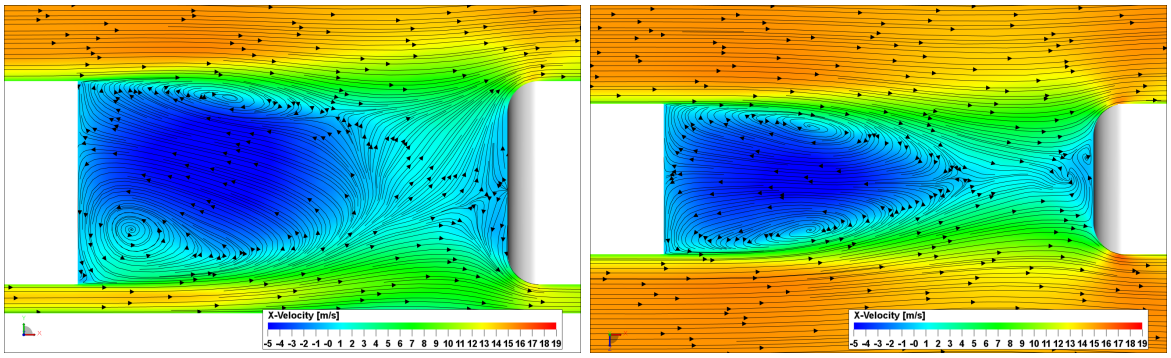


Figure 2.41: Numerical time-averaged and transient streamlines coloured by the velocity magnitude in the gap of the R68-R68 platoon at 0.45 s/L

a large region of reversed flow can be seen, the magnitude of this reversed flow however is smaller than that of the isolated model which explains the higher pressure on the rear of the model. Moving downstream the velocity in front of the front surface of the trailing model is also greatly reduced compared to the isolated model. This leads to a lower stagnation pressure on one hand but also has an undesirable consequence for the rounded edges of the model. Due to the lower velocity seen by the rounded edges the flow is only accelerated to a value just below the free-stream velocity. This means that no negative pressure is formed on the rounded edges as was detected in the previous paragraphs. This lack of suction explains the drag increase experienced by the trailing model. With the time averaged results discussed



(a) Vertical centre plane z=0 (b) Horizontal centre plane y=0.5H

Figure 2.42: Numerical streamlines with contours of x-velocity in the gap of the R68-R68 platoon at 0.45 s/L

the transient findings are addressed next. In figure 2.43 the results of a frequency analysis for the drag and sideforce of the various platoons configurations. From this figure a peak in the drag force can be seen at a Strouhal number of 0.088. The magnitude of this peak is twice as high as that of the single model. For the sideforce a peak at a Strouhal number of 0.160 can be seen, the magnitude is 6.5 times higher than that of isolated model. The cause of these force fluctuations can be attributed to the pressure fluctuations which are given in

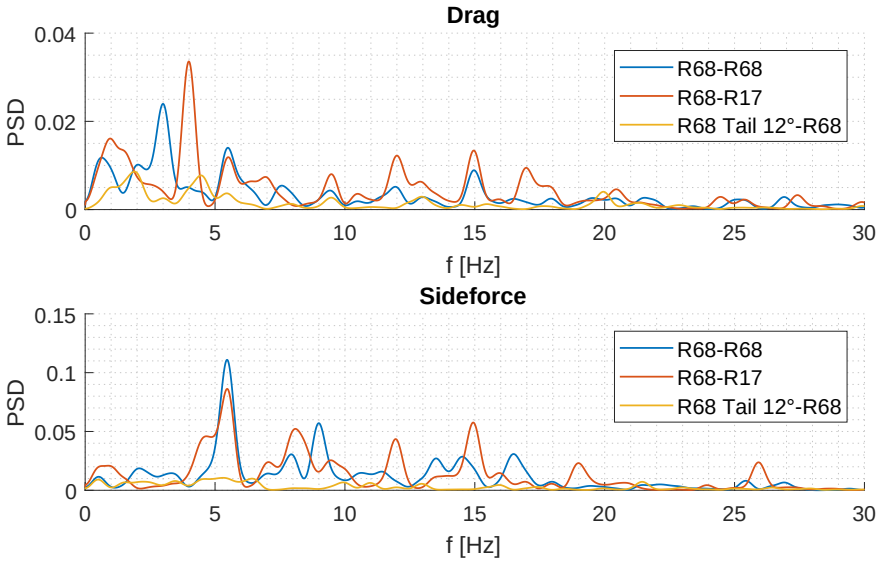
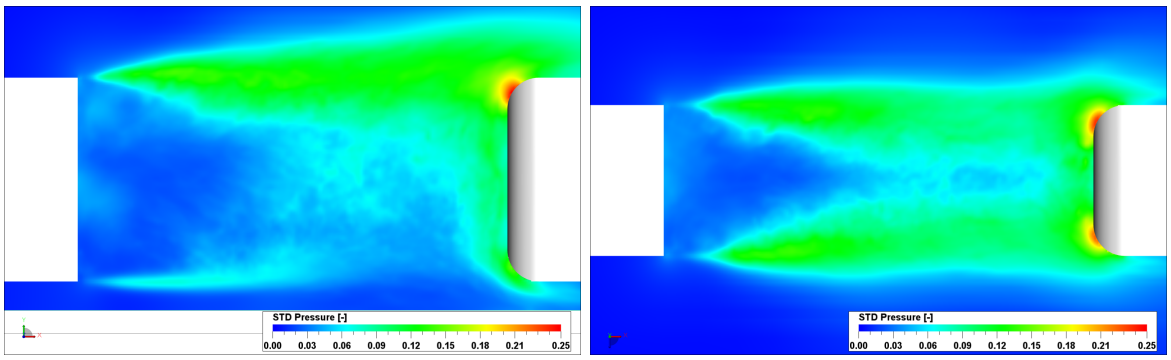


Figure 2.43: Numerical PSD of the drag and side force of the trailing model in the platoon at 0.45 s/L

figure 2.44. From this figure it can be seen that the fluctuations have increased compared to



(a) Vertical centre plane z=0

(b) Horizontal centre plane y=0.5H

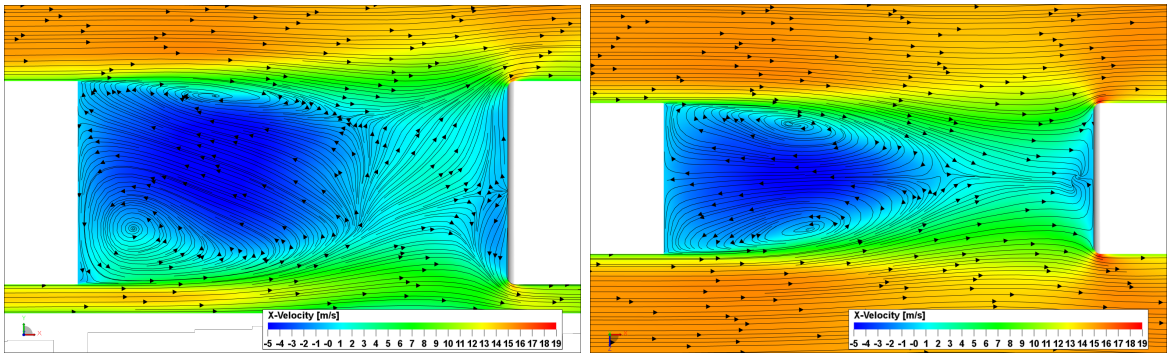
Figure 2.44: Numerical pressure fluctuations in the gap of the R68-R68 platoon at 0.45 s/L

the platoon at 0.10 intervehicle distance. From an unsteady pressure analysis it was seen that the force fluctuations were caused by the vortices being shed from the leading model. These hit the front of the trailing model where they are deflected.

Effect of front edge radius on the trailing model: R68-R17 For the second platoon the front edge radius of the trailing model was changed to the most sharp one of 17 mm. From figure 2.37 it can be seen that changing the front edge radius of the trailing model has no influence whatsoever on the drag reduction of the leading model. Its drag is still 69% of the isolated model. The behaviour of the trailing model however is quite different. Where the

trailing model of the baseline platoon experienced a drag increase the drag is now lowered by 26%. The same drag decrease was also found by Gheyssens (2016) for the trailing vehicle of a 3-vehicle platoon.

The drag breakdown in figure 2.38 clearly shows that the majority of the drag reduction is caused by the rear and front surfaces for the leading and trailing model respectively. Compared to the results found by Gheyssens (2016) more drag reduction is generated from the front part, from his research also a significant drag reduction was found from the rear surface which can not be seen here. As the drag reduction of the leading model is identical to that of the baseline platoon a similar pressure distribution is expected on the rear surface. From figures 2.39(a) and 2.40(a) it can be seen that this is indeed the case. The pressure on the front surface of the trailing model is quite similar as well although some differences can be noticed. For starters the suction peak on the rounded edges which was absent, with exception of the top edge, on the baseline platoon has now returned. The magnitude of this peak is lower compared to the isolated model. Next to this the stagnation pressure on the front middle part is decreased, its magnitude is very much the same as the model with the larger front edge radius. The flow field between the two models given in figure 2.45 is



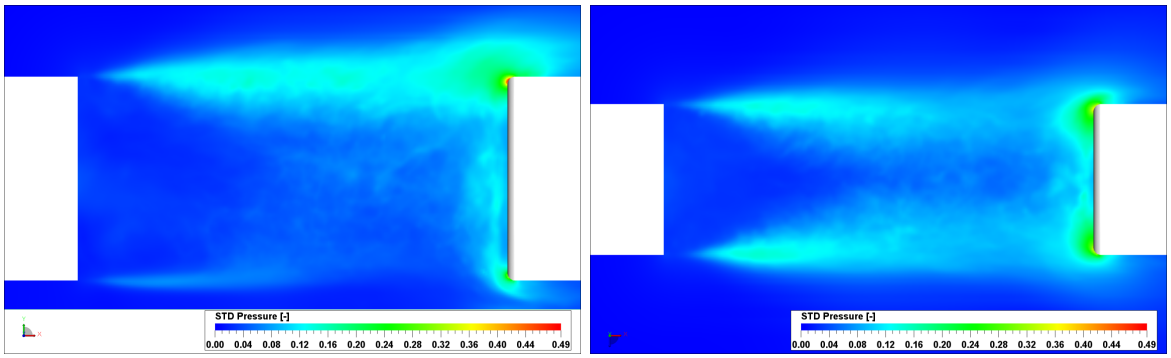
(a) Vertical centre plane z=0

(b) Horizontal centre plane y=0.5H

Figure 2.45: Numerical streamlines with contours of x-velocity in the gap of the R68-R17 platoon at 0.45 s/L

very similar to that of the baseline platoon. In fact the only differences can be seen in the vicinity of the trailing model. Due to the larger frontal stagnation area the region of flow of decelerated flow is wider. This is most noticeable from the horizontal centre plane in figure 2.45(b). Next to this due to the sharper edges the flow over these edges is accelerated to a higher velocity.

An analysis of the unsteady drag and sideforce given in figure 2.43 shows a peak at a Strouhal number of 0.117 the magnitude of this peak is a lot higher than the one of the baseline platoon. For the sideforce the peak occurs at the same frequency as the baseline platoon, only its magnitude is slightly lower. The difference in force fluctuations can be attributed to the sharper front edge radius that the trailing model has. From figure 2.46 it can be seen that the fluctuations in the shear layer of the leading model have not changed. It is the way the trailing model receives the vortices shed that influences the forces. Because



(a) Vertical centre plane z=0 (b) Horizontal centre plane y=0.5H

Figure 2.46: Numerical pressure fluctuations in the gap of the R68-R17 platoon at 0.45 s/L

of the larger front part the vortices are not deflected that easily leading to the higher drag fluctuations. Also because of the sharper edges when the vortex passes it has less area exposed to the side to work with which results in the lower side force fluctuations.

Effect of a tail on the leading model: R68 Tail 12°-R68 For the last simulation at this distance a tail of 12° was added to the leading model. In this configuration the drag of the leading model is reduced by 65% while the drag of the trailing model is again higher than that of the isolated model. Although not as severe as the baseline platoon still 14 % more drag is added. Because of the high drag reduction of the leading model the average drag reduction is still 25%.

From figure 2.38 one can see that most of the drag reduction from the leading model comes from the rear surface while the drag increase for the trailing model is generated by the front. This decrease and increase in drag can be explained by looking at the pressures given in figures 2.39 and 2.40. For the pressure over the rear surface it can be seen that the pressure has experienced a constant increase compared to the isolated model. This means that an even greater thrust force is now exerted on the rear surface. The effect of the platoon on the pressure of the front of the trailing model is not as big. From figure 2.40(b) it can be seen that most of the pressure is very similar to that of the baseline platoon. The upper half of the model shows that the pressure is slightly lower. This is not the case for the lower part, here the pressure is higher and a small peak can be seen at about 15% model height. The pressure on the horizontal centre line over the rear surface of the leading model shows the same behaviour as that on the vertical centre line. The pressure has shifted to a higher value and is almost constant over the entire domain. For the pressure over the front surface of the trailing model also not much has changed compared to the baseline platoon. On the right side the pressure is slightly lower everywhere while on the left side a small pressure increase can be seen. The small asymmetry that is seen when comparing the pressures on the left and right side may be resolved by averaging over a longer time.

These changes in pressure can be explained by looking at the flow field in the gap. This is visualised in figure 2.47. From this one can see that the recirculation region is much smaller than that of the baseline platoon. Just as in the case of the baseline platoon the flow is entering this region from the top, bottom and sides of the leading model. Before entering however it is guided inwards due to the tail. When it enters it turns, reverses and flows into the cavity of the tail where it is slowed down even more. The flow not entering the recirculation region is also drawn inward and follows a curved path on its way to the front of the trailing model. Part of the flow stagnates on the front surface while the rest flows over the rounded edges and is accelerated.

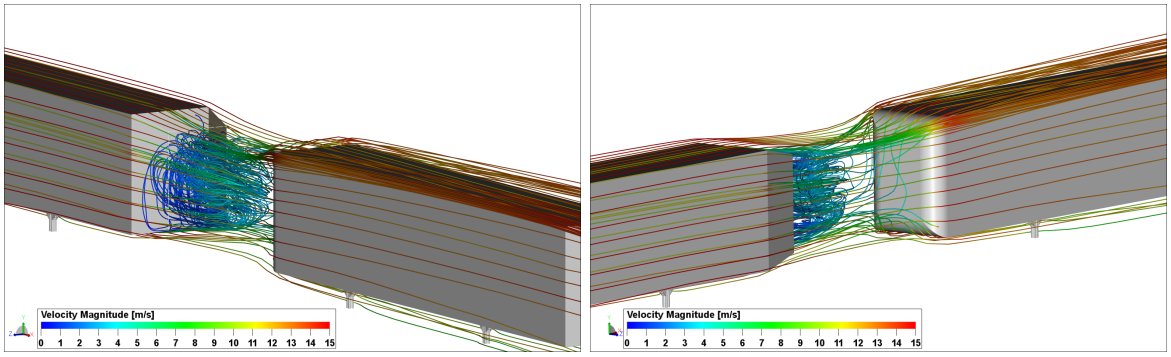
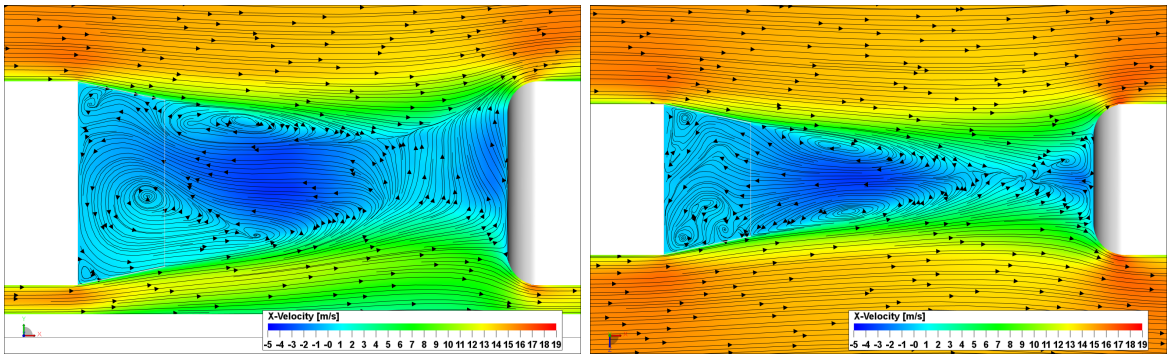


Figure 2.47: Numerical time-averaged and transient streamlines coloured by the velocity magnitude in the gap of the R68 Tail 12°-R68 platoon at 0.45 s/L

The flow in the gap can also be seen in figure 2.48 in more detail. From the vertical centre plane the wake structure can be observed. This structure is made up of multiple vortices. The two main ones can be seen in the upper right corner and one that is located inside the cavity of the tail. Next to this three smaller vortices can be seen. Two of them are located in the corners of the tail and the other one lies outside the tail next to the main vortex. The flow entering the wake region can be seen coming from the top and bottom. As it enters the wake it turns and its direction is reversed, it either ends up in one of the vortices that are further downstream or enters the cavity of the tail where it is slowed down even more. Flow that is not captured by the wake can be categorized into three regions. The flow above the streamline that leaves from the saddle point, flow between that streamline and the stagnation streamline from the front surface of the trailing model and the region below the stagnation streamline. In the first region the flow is drawn inward and decelerated. When it comes close to the trailing model it turns and moves upwards where it is accelerated over the rounded edge and leaves the gap. The flow in the second region is coming from the bottom of the leading model. Due to the upwash that the tail induces the flow stagnates with a higher velocity on the front of the trailing model. The flow that does not stagnate takes a very sharp turn and is sent upwards where it is accelerated over the top edge and leaves the gap. The flow in the last region is quite similar than that of the first one. The flow is drawn inward and decelerated, when it comes in the vicinity of the trailing model it turns and accelerates over the bottom rounded edge. Looking at the flow in the horizontal centre plane first of all it can be seen that the flow to the left and the right of the centre line is quite symmetric although some differences are visible. The flow in the wake is composed of multiple vortices. The main two are seen outside the



(a) Vertical centre plane z=0 (b) Horizontal centre plane y=0.5H

Figure 2.48: Numerical streamlines with contours of x-velocity in the gap of the R68 Tail 12°-R68 platoon at 0.45 s/L

cavity of the tail while the rest is located inside this cavity. In front of the trailing model there also appear to be two vortical structures. The flow that is coming from the sides either ends up in the wake or passes by and takes one of two paths. Part of it stagnates on the front surface of the trailing model where it turns and reverses direction creating the vortex. The other part flows past the model and is accelerated over the rounded edge as it leaves the gap. The flow that ends up in the wake also reverses direction and is drawn into one of the two main vortices or it flows into the gap where it swirls and creates smaller vortices.

The unsteady force analysis of this configuration shows that most of the fluctuations in drag and sideforce have diminished. It was already seen that effect of a tail of 12° on a single model reduced the pressure fluctuations in the wake region. This is also the cause of the lower fluctuations in force for this configuration.

Intervehicle distance: 0.91 s/L

For the third and final platoon configuration the models where placed 0.91 times the vehicle length from each other. Next to the baseline platoon the effect of a sharper front edge radius on the trailing model was also investigated. Figure 2.49 shows the resulting relative and absolute drag values from these simulations. The bars indicate the relative drag while the values above each bar display the absolute drag.

Baseline platoon: R68-R68 At this distance the benefit of platooning for the baseline platoon is hardly noticeable. The gains are only 7, 5 and 6% for the leading, trailing and average of the two models. Compared to the results from Gheyssens (2016) the drag reduction of the trailing model is very similar, he found a drag reduction of 6% for the leading model of a 3 vehicle platoon. The trailing model in this platoon experienced a drag decrease of 13 % which is more than double of what is seen here. This extra drag reduction could come due to the fact that in his study the trailing vehicle is shielded by two vehicles rather than

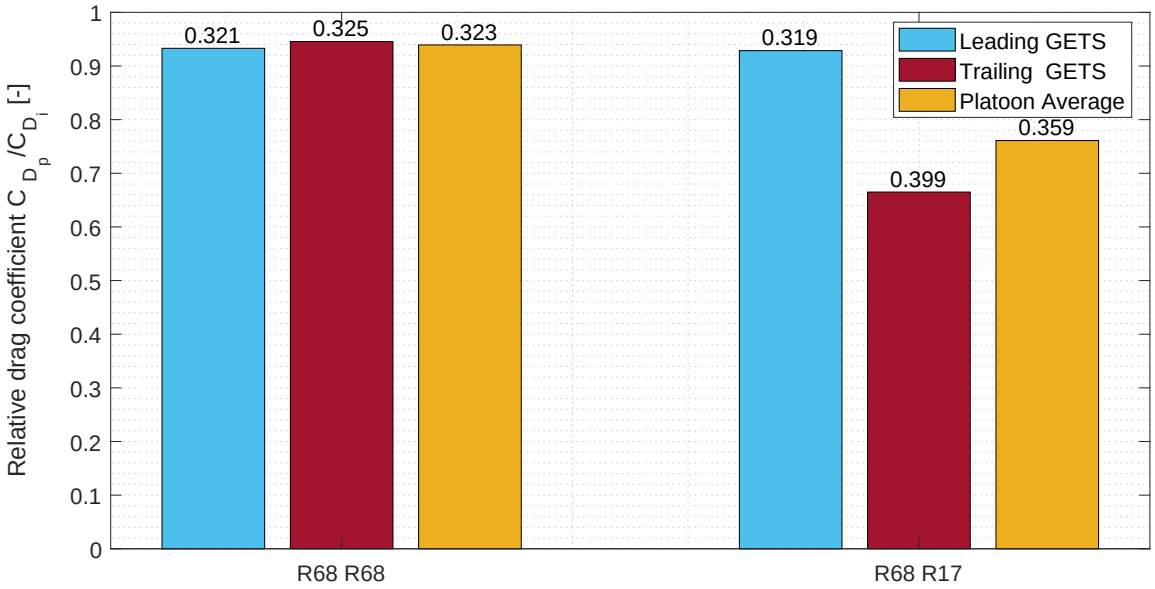


Figure 2.49: Numerical relative and absolute drag coefficient for the platoons at 0.91 s/L

the one in this study. From figure 2.50 it can be seen that most of the drag reduction from

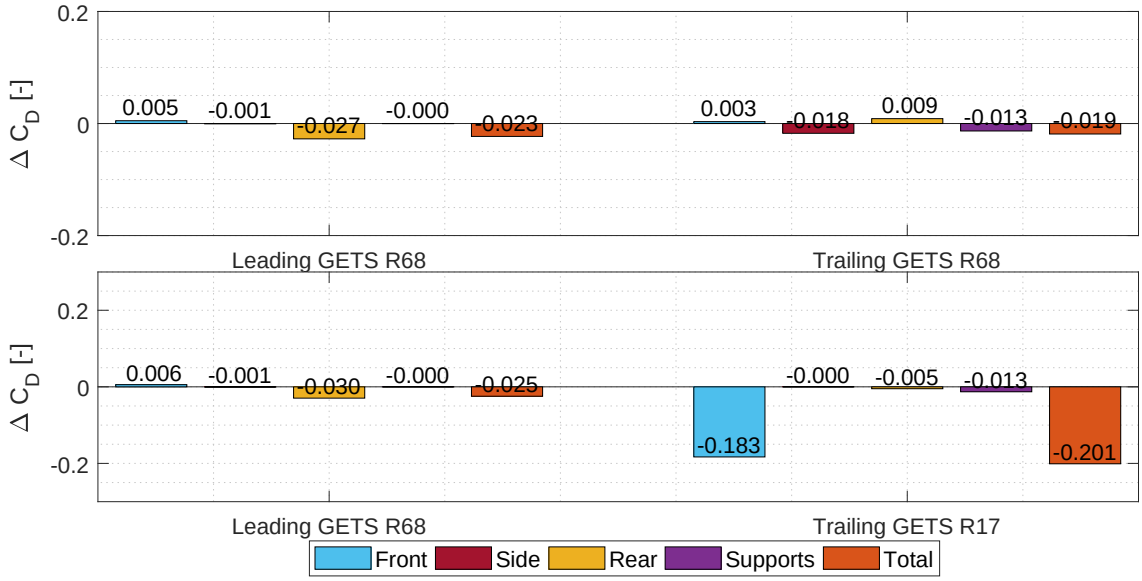
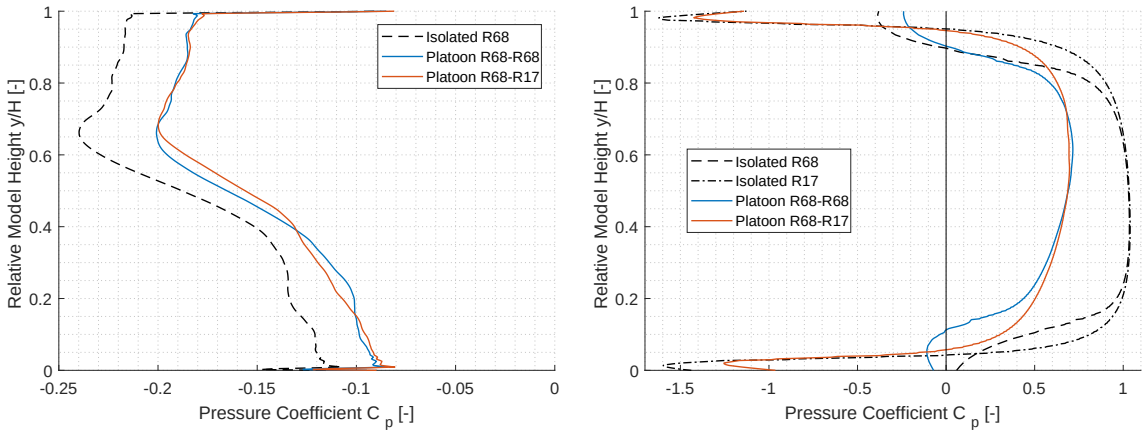


Figure 2.50: Numerical drag differences with respect to the single model for the leading and trailing model in a platoon at 0.91 s/L

the leading model is generated by the rear surface which is to be expected. For the trailing model however most of the drag reduction is caused by the sides. Whereas the drag decrease for the trailing model in previous analysed platoons was mostly caused by the front surface. Its value is now very close to that of the isolated model. The reason for this can be explained

by looking at the pressure given in figures 2.51 and 2.52.

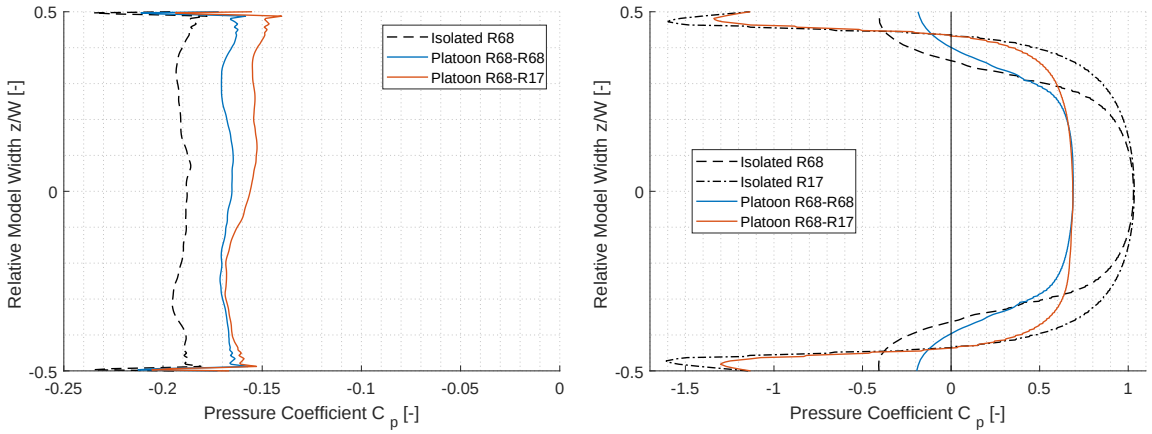


(a) Rear surface leading model

(b) Front surface trailing model

Figure 2.51: Numerical pressure coefficient over the surfaces of the platoon at 0.91 s/L y=0.5H

For the pressure on the surface of the rear of the leading model it can be seen that the suction has been lowered, there is an almost constant offset compared to the isolated model. The pressure distribution on the front surface of the trailing model does show some more differences compared to the isolated model. First off the suction peak at the top of the model has been slightly reduced, the stagnation pressure on the front middle part has also been decreased. On the bottom of the model a new suction peak has been formed where there was none on the isolated model. The pressure on the horizontal centre line on the rear surface of



(a) Rear surface leading model

(b) Front surface trailing model

Figure 2.52: Numerical pressure coefficient over the surfaces of the platoon at 0.91 s/L distance z=0

the trailing model shows similar behaviour to that on the vertical centre line. Also here an

almost constant offset compared to the isolated model can be seen which explains the lower drag. For the trailing model the same two effects that were noticed on the previous platoons can be seen. The suction peaks on the rounded edges have been reduced but in this case still have a negative magnitude. Next to this the stagnation pressure on the middle part has been decreased as well. Just as in the case of the previous platoons these two phenomena cause a drag increase or decrease. Remarkable in this configuration is that the reduced thrust force from the rounded edges and the drag reduction from the reduced stagnation pressure almost cancel each other out giving nearly the same front drag as the isolated model.

At this distance the flow field between the two models given in figure 2.53 resembles that of the isolated model quite well. The wake structure of the leading vehicle is almost identical to that of the isolated model. Flow from the top, bottom and sides of the model enters the recirculation region where it decelerates and reverses direction. After that it stagnates on the rear surface and flows back in the recirculation region or flows out of the wake and hits the front of the trailing model where it stagnates or flows over the rounded edges where it accelerates.

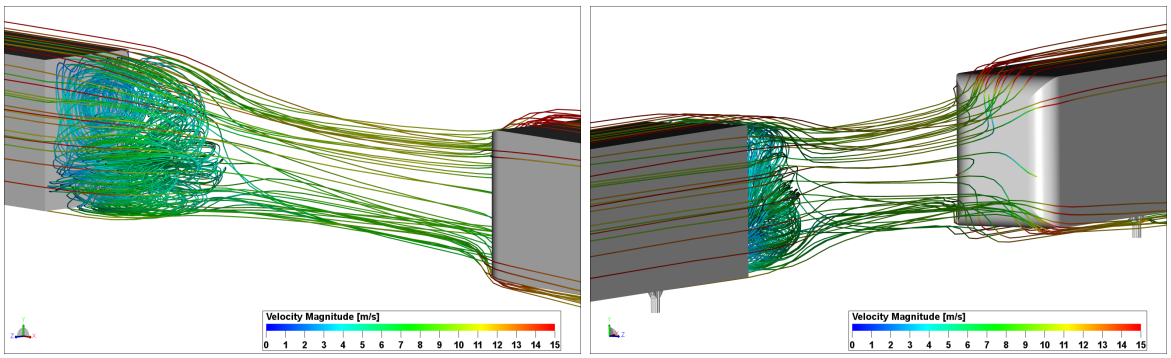
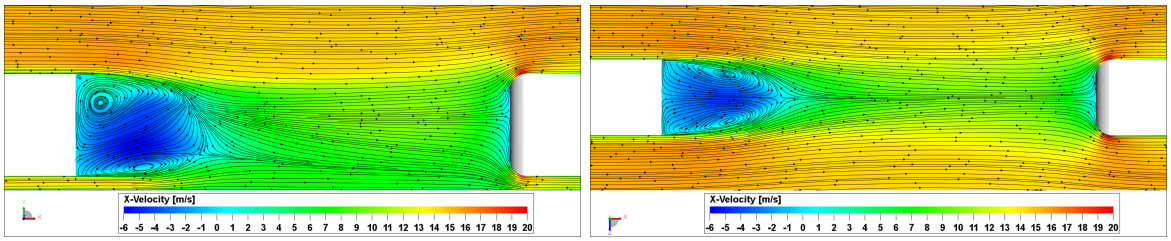


Figure 2.53: Numerical time-averaged and transient streamlines coloured by the velocity magnitude in the gap of the R68-R68 platoon at 0.91 s/L

The similarities in the wake flow of the leading model can also be seen in figure 2.54. From figure 2.54(a) it can be seen that the saddle point has been shifted to the bottom of the model and is now very close to that of the isolated model. The size and shape of the recirculation region is also very similar compared to that of the isolated model. Besides this it is also clear the the incoming flow for the trailing model has a much higher velocity compared to the platoon at 0.45 vehicle distance. This explains the higher stagnation pressure and also the return of the suction peak on the rounded edges of the model. The suction peak on the bottom of the model which was not present in the isolated case is caused by looking at the streamlines. When they enter the underbody of the trailing model they converge which indicates an acceleration of the flow and decrease in pressure. With the time-averaged results analysed next the transient behaviour of the flow is discussed. The effect of it on the drag and sideforce is given in figure 2.55 where the PSD of both of these forces is shown.

Form this figure peaks in both the drag and sideforce for the baseline platoon can be seen. These peaks are of higher magnitude than those of the single model and occur at a Strouhal number of 0.100 and 0.146 for the drag and side-force respectively.



(a) Vertical centre plane z=0 (b) Horizontal centre plane y=0.5H

Figure 2.54: Numerical streamlines with contours of x-velocity in the gap of the R68-R68 platoon at 0.91 s/L

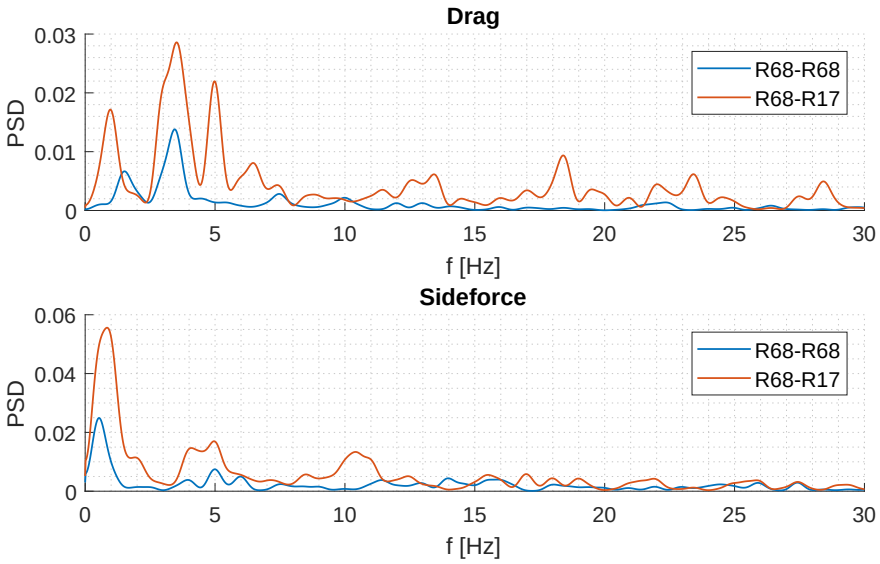
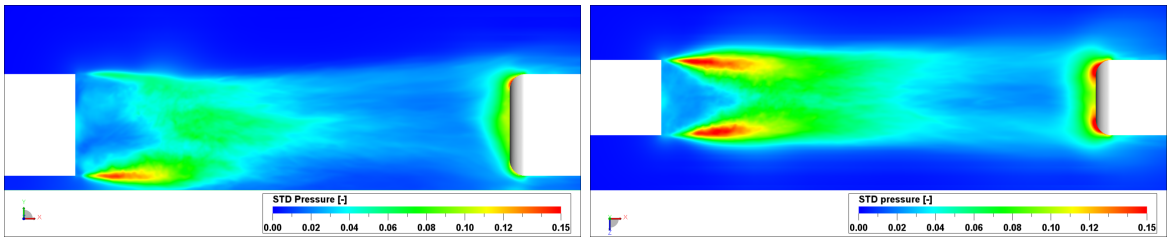


Figure 2.55: Numerical PSD of the drag and side-force of the platoons at 0.91 s/L

The increase in the unsteady forces is caused by the pressure fluctuations which are given in figure 2.56. From this it can be seen that the fluctuations in the wake of the leading model have returned to the values that were seen for the isolated model. Next to this high fluctuations can be seen at the front of the trailing model which are the cause of the force fluctuations. The fluctuations are smaller than of the platoon at 0.45 intervehicle distance. This is because the strength of the vortices being shed from the leading model have been reduced when they move downstream.

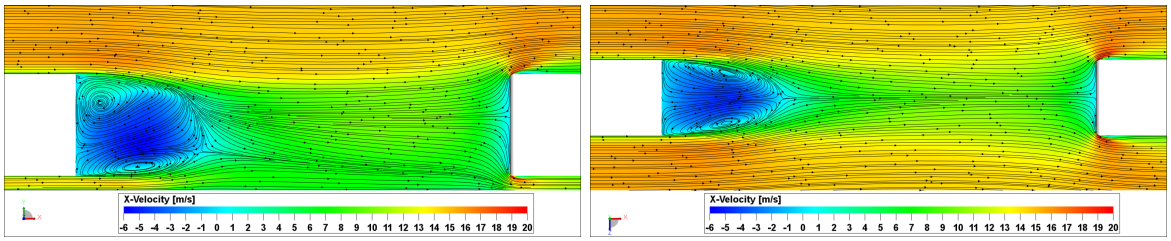


(a) Vertical centre plane z=0 (b) Horizontal centre plane y=0.5H

Figure 2.56: Numerical contours of the standard deviation of pressure in the gap of the R68-R68 platoon at 0.91 s/L

Effect of front edge radius on the trailing model: R68-R17 The second platoon tested at this intervehicle distance is the one where the trailing model is applied with the sharpest front edge radius of 17 mm. The effect of the platoon on the leading model is virtually unchanged compared to the baseline platoon. Again the drag decrease is 7%. For the trailing model the platoon has a much greater effect the drag decrease is 34% which is even higher than the platoon at 0.45 intervehicle distance. This is similar to the value of 37% which was found by Gheyssens (2016). On average the drag reduction is 24%. From figure 2.50 it can be seen that for the leading model most of the drag reduction is coming from the rear surface. Whereas most of the drag reduction for the trailing model of the baseline platoon was coming from the side in this configuration the part generating the most drag reduction is the front part again. Compared to the values found by Gheyssens (2016) the drag reduction of the front is very similar, 30% vs 31% in this study, next to this he found a significant drag reduction coming from the rear surface which has only a minor contribution in this study. This could come from the fact that at this intervehicle distance no separation was observed where it is seen here.

The drag reduction can be explained by looking at the pressure distribution over the rear and front surfaces of the leading and trailing model given in figures 2.51 and 2.52. The pressure over the vertical centre line on the rear surface of the trailing model is almost identical to that of the baseline platoon. Compared to the isolated model there is an almost constant increase in pressure. On the horizontal centre line given in figure 2.52(a) the suction is also lowered. Despite the model being symmetric and simulated at 0° yaw the pressure distribution shows a slight asymmetry. On the front surface of the trailing model the same two phenomena that where seen in the previous platoons can be observed. Namely the reduction of the stagnation pressure on the front middle part and the reduction of the suction on the rounded edges. The reduced suction on the rounded edges is very small meaning that almost the same thrust force is created as for the isolated model. The flow field between the two models given in figure 2.57 is very similar to that of the baseline platoon. The wake of the leading model is very comparable to that of the isolated model. For instance the size and shape of the recirculation region and the location of the saddle point is almost identical to that of the isolated model. Next to this some differences can be seen, especially in the region near the trailing model. The region of slower flow in

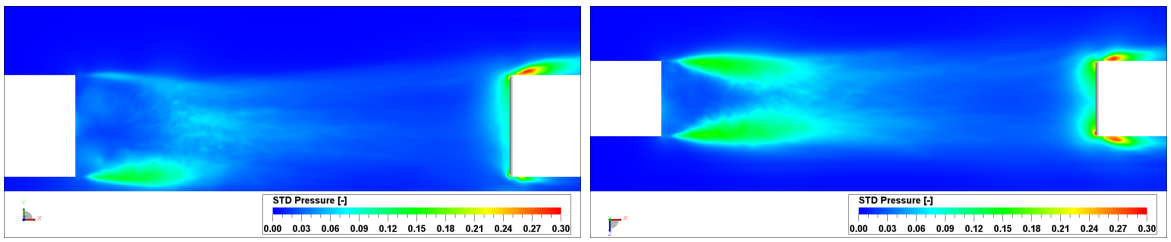


(a) Vertical centre plane z=0 (b) Horizontal centre plane y=0.5H

Figure 2.57: Numerical streamlines with contours of x-velocity in the gap of the R68-R17 platoon at 0.91 s/L

front of the trailing model has been greatly reduced compared to the platoons at smaller intervehicle distances. This in turn has two effects namely a slightly higher stagnation pressure compared to the previous platoons but also higher suction due to the acceleration over the rounded edges. This increased suction however also creates an adverse pressure gradient which the flow is not able to cope with. On the top and the edges of the trailing model separation can be seen by the reversed flow. Because the incoming flow still has a lower velocity than the free stream this separation is not as severe as that of the isolated model.

The unsteady force analysis in figure 2.55 shows an increase in both drag and side-force compared to the baseline platoon. This is caused by two phenomena. On the one side the vortices that impact the front of the trailing model result in the higher fluctuations in drag. These fluctuations can be seen in figure 2.58. Next to this high fluctuations at the sides of the model can be seen. These are caused by the separation that was seen in figure 2.57.



(a) Vertical centre plane z=0 (b) Horizontal centre plane y=0.5H

Figure 2.58: Numerical contours of the standard deviation of pressure in the gap of the R68-R17 platoon at 0.91 s/L

Chapter 3

Experimental Analysis

The second analysis method is an experimental campaign held in the OJF at TU Delft. During this experiment balance and CVV measurements were taken. The results from these measurements will be used to validate the numerical results. Next to this additional platoon configurations were tested. The chapter starts out with explaining the experimental set-up. After this the obtained results are discussed.

3.1 Experimental Set-up

3.1.1 Open Jet Facility

The experimental campaign was carried out in the Open Jet Facility (OJF) at TU Delft. The OJF is an open jet wind tunnel with an octagonal nozzle measuring 2.85 by 2.85 m. This nozzle debouches into a room, for which the main dimensions can be seen in figure 3.1, in which the experimental set-up was built. Although the maximum speed of the OJF is 35 m/s TU Delft (2016) it was decided to conduct the experiment at 15 m/s which is the limit for using the Shake The Box (STB) algorithm Schanz et al. (2016). The free stream turbulence in the OJF is 0.5% as was reported by Lignarolo et al. (2014) however this is not taking into account the seeding rake which will increase the turbulence as was found by Jux (2017).

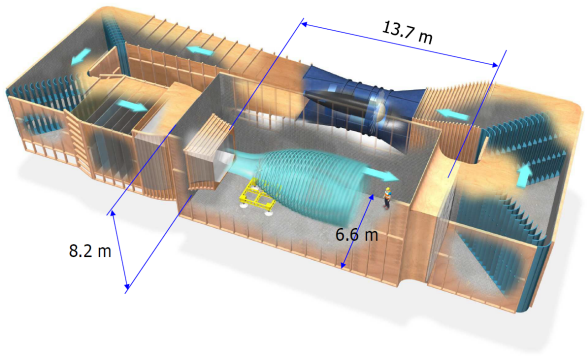


Figure 3.1: Schematic of the OJF with the dimensions of the test section TU Delft (2016).

3.1.2 Wind Tunnel Models

For the experiment the same model that was described in section 2.1 was used. This model can be seen in figure 3.2 and is made up of different parts.

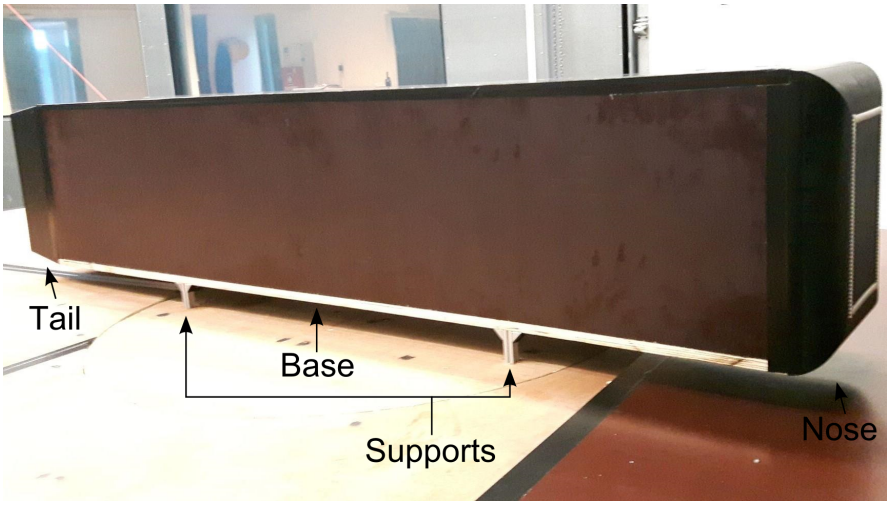


Figure 3.2: Experimental GETS model with a tail

Base with supports

The base of the model consists of a rectangular prism which was constructed out of laminated plywood. 18 mm thick plywood was used to the bottom plate while 12 mm plates were used for the front, back, top and sides. These plates were attached to each other by means of wood screws. To attach the model to the wooden plate that was attached to the balance use was made of 4 aluminium profiles item Industrietechnik GmbH (2017) which were also screwed to the model.

Nose

Because the noses of the model were going to be changed during the experiment they were made as a separate part. The noses with different front edge radii were made out of polyurethane Rampf Tooling Solutions GmbH (2015) because it is easily millable. To attach them to the wooden base threaded inserts were placed in the noses after which they could be bolted to the base. Because of the natural light colour of the noses the ones that were attached to the trailing model were painted black to minimize reflections coming from the laser light. Because one wants to have attached turbulent flow over the model in order to match the real life conditions as closely as possible it was decided to trip the boundary layer using zig-zag tape. With the help of a microphone the flow past the nose was checked for separation bubbles. For the nose with a radius of 68 mm two layers of zig-zag tape with a thickness of 0.9 mm were applied. The same tapes were applied to the noses with a smaller radius.

Tails

Lastly the various tails were made out of 1.5 mm steel and were attached to the model by means of screws and tape to ensure a smooth transition between the base model and the tail.

3.1.3 Performed Measurements

During the experimental campaign two types of measurements were performed namely force and Coaxial Volumetric Velocimetry (CVV) measurements.

Force Measurements

Because no integrated force measurement system is present in the OJF use was made of the balance provided by NLR. This balance is capable of measuring both forces and moments around the x-,y- and z-axis with an accuracy of 0.06%, 0.23% and 0.16% for the x-, y- and z-forces and 0.05%, 0.05% and 0.25% for the moments around the x-,y- and z-axis respectively Alons (2008). An averaging window of 60 seconds was chosen. After an averaging window of 30 seconds most of the osculations in the drag force had already averaged out but 60 seconds was chosen to make sure that the value had converged for all configurations.

CVV Measurements

To capture the flow field between the two models CVV measurements were performed. This relatively new technique has some advantages over conventional tomographic PIV which will be explained in this section.

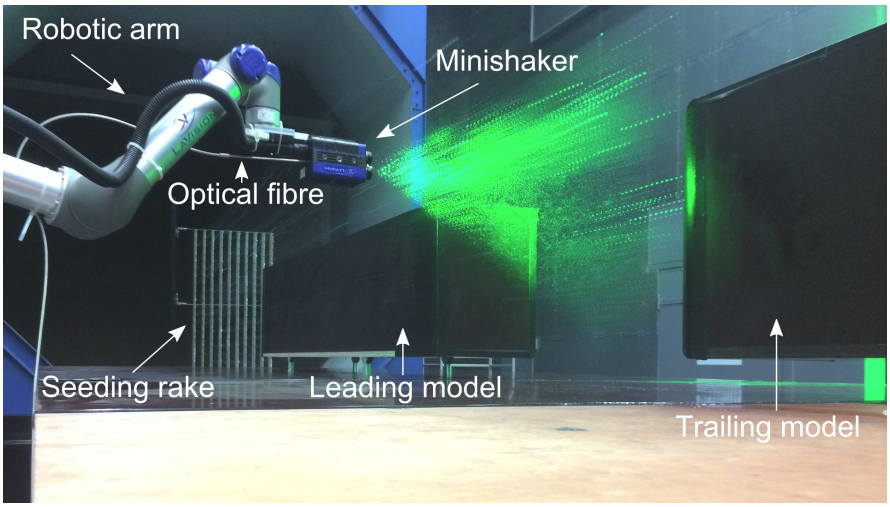


Figure 3.3: Experimental set-up for the CVV measurements

Seeding Rake The tracer particles used in this experiment are helium filled soap bubbles (HFSB) which were introduced by Scarano et al. (2015) and allow the measurement of a large volume with reduced illumination intensity. These particles are generated by the seeding rake visible in 3.3. This seeding rake consist of 10 wings which are 1 m in length. Each of these contain 20 nozzles each making for a total of 200 bubble producing nozzles. During another experiment it was noticed that some of the nozzles were never producing bubbles, these were closed which leaves a total of 175 nozzles. Each of these nozzles nominally produces 30.000 bubbles per second. The bubble production is regulated using a Fluid Supply Unit from *LaVision*. Optimal particle production was found at 2.0 bar for helium, air and soap.

The effect of the seeding rake on the free stream turbulence was measured by means of a CVV measurement. The velocimeter was positioned perpendicular to the flow around 3 m downstream of the wind tunnel exit. Evaluating the free stream turbulence intensity at this location gives a level of 1.2% which is approximately 1.4 times higher than the value reported by Lignarolo et al. (2014) and 0.6 times lower as the value noted by Jux (2017) for a smaller seeding rake.

Minishaker The coaxial velocimeter called the minishaker is what was used to capture the images necessary for the flow field reconstruction. It is made up of a cuboid which houses four *LaVision MiniShaker* S CMOS cameras with protruding lenses. Next to this the optical fibre is also implemented into the body. The cameras have a sensor size of 800 x 600 pixels however because of the velocity of 15 m/s this had to be reduced in order to have a higher image rate of 749 Hz. For this image rate the sensor size reduces to 720 x 432. The benefit of this configuration is that imaging and illumination are contained in one system which makes it very easy to capture hard to reach locations as was the case for the gap between the two models.

Calibration Another advantage of using CVV is that the previously discussed minishaker only needs one geometrical calibration for the entire experimental campaign and in theory its lifetime. This calibration is done using a pinhole-calibration model Soloff et al. (1997). A type 30 calibration plate was placed at three distances from the minishaker namely 150, 350 and 550 mm. The zero plane of the camera is located at roughly 350 mm but is exactly determined afterwards. Next to the geometrical calibration a volume self-calibration is also done to further improve the accuracy of the system Wieneke (2008). Using the corrected calibration an Optical Transfer Function (OTF) is calculated which allows the projection of 3D to 2D coordinates. This OTF is required for the STB algorithm and will be used on all recorded images. That is why a highly accurate OTF is required.

Volume Illumination In order to illuminate the tracer particles use is made of a Quantronix Darwin Duo Nd:YLF high speed laser. Through the use of a spherical lens the laser beam converges into the optical fibre (figure 3.4) which extends all the way up to the velocimeter. There the light enters another spherical lens which diverges it in the cone which can be seen in figure 3.3.

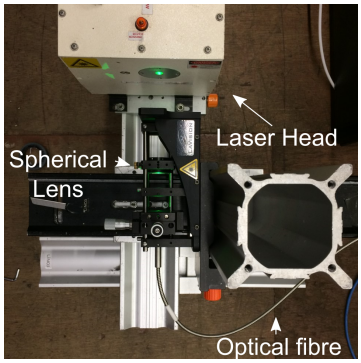


Figure 3.4: Coupling of the laser head to the optical fibre

Robotic Arm The previously discussed minishaker was placed upon a *Universal Robots - UR5 robotic* arm which allows for high degree of moveability and makes that it can easily be placed at a given location. The arm can reach a maximum of 85 cm and has 6 degrees of freedom, 3 rotations and 3 translations A/S Universal Robots (2017). It can be controlled by a tablet which allows for individual movement of the joints or the movement of the 'tool' which in this case is the minishaker. Next to this it also allows the user to save positions and recall them in the future which saves a lot of time and reduces the risk of entering a wrong coordinate during measurements.

3.1.4 Data Processing

Force correction for the turning disk

Because the model is not directly attached to the balance but a wooden disk exists between them when measuring the forces one does not solely measure the forces on the model but those of the wooden disk as well. That is why the forces of the disk without a model were obtained for the single model configuration and both intervehicle distances. These forces are then subtracted from those were the model was installed. A drawback of this procedure is that the interaction between the model and the wooden disk is neglected. Nonetheless no simple correction method is available for this interaction as is explained by SAE (2012).

Wind tunnel Corrections

Because the flow is affected by the wind tunnel and the presence of the model first some corrections on the data must be applied. In an open wind tunnel there are several effect one must correct for namely: nozzle blockage, solid blockage, empty-tunnel pressure gradients and collector blockage Cooper (1998). In this study the latter two are assumed to have no effect on the flow and are thus neglected. Although the ground plate in the experimental campaign was elevated slightly above the nozzle exit and the corrections described by Cooper (1998) are given for a ground plate and nozzle exit at equal height it was assumed that these can still be applied.

Nozzle blockage Due to the presence of the model close by the nozzle exit the effective nozzle area is reduced, this causes the flow velocity to increase at the edge of the nozzle. The correction factor for the nozzle blockage is given in 3.1.

$$\epsilon_n = \epsilon_{qn} \left(\frac{R_n^3}{(x_m^2 + R_n^2)^{3/2}} \right) \tag{3.1}$$

Where R_n is the hydraulic radius given by the square root of the nozzle area divided by pi, and x_m is the distance from the centre of the model to the nozzle. The perturbation velocity at the nozzle plane ϵ_{qn} is given by 3.2.

$$\epsilon_{qn} = \frac{\left(\frac{S}{2C}\right)\left(1 + \frac{x_s}{(x_s^2+R_n^2)^{1/2}}\right)}{\left(1 - \left(\frac{S}{2C}\right)\left(1 + \frac{x_s}{(x_s^2+R_n^2)^{1/2}}\right)\right)} \tag{3.2}$$

With S the frontal area of the model, C the nozzle area and x_s the distance from the source to the nozzle:

$$x_s = -x_m + \left(\frac{L_m}{2}\right) - \left(\frac{S}{2\pi}\right)^{1/2} \tag{3.3}$$

Where L_m is the length of the model.

Solid blockage Because the flow has to go around the model and therefore over-expands another correction factor must be applied. The correction term for the solid blockage is given in 3.4.

$$\epsilon_s = \tau \left(\frac{V}{L_m}\right)^{1/2} \left(\frac{S}{C_e^{3/2}}\right) \tag{3.4}$$

Where τ is a solid blockage correction factor from Garner et al. (1966) ,V is the volume of the model and the nozzle area reduction is given by 3.5.

$$C_e = \frac{C}{(1 + \epsilon_{qn})} \tag{3.5}$$

Total Correction Factor With the previous discussed correction factors the total correction factor for the velocity and dynamic pressure can be calculated using:

$$\frac{U_c}{U_n} = 1 + \epsilon_s + \epsilon_n \tag{3.6}$$

$$\frac{q_c}{q_n} = (1 + \epsilon_s + \epsilon_n)^2 \tag{3.7}$$

The resulting correction factors for the single model and platoon can be found in table 3.1.

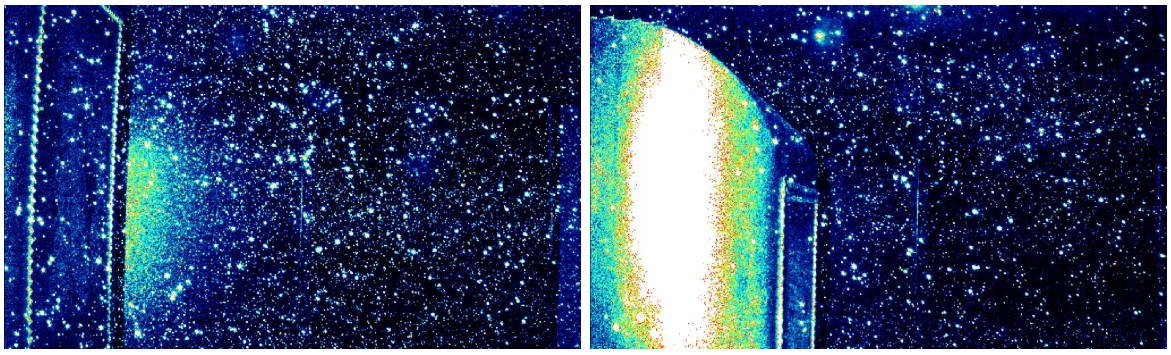
Table 3.1: Total correction factor for the single model and platoon configurations

Total Correction Factor	Single Model	Platoon 0.10	Platoon 0.45
$\frac{U_c}{U_n}$	1.0081	1.0021	1.0014
$\frac{q_c}{q_n}$	1.0162	1.0042	1.0029

CVV Processing

Before one can analyse the results coming from the CVV measurements some post-processing must be done. This includes filtering of the raw images, particle tracking, binning and stitching of multiple runs and pressure determination from the resulting flow field which will be treated in the following paragraphs.

Image Processing During the experiment for each CVV measurement 8000 images were taken. Visual inspection of these resulted into two groups of images. One with little to no reflections (figure 3.5(a)) and one with high reflections (figure 3.5(b)) which mostly came from the model.



(a) Image with little reflections

(b) Image with high reflections

Figure 3.5: Two types of images coming from the CVV measurements

Two different strategies were employed processing these two types of images. For the image with little reflections the Butterworth filter, a high pass frequency filter first introduced by

Sciacchitano and Scarano (2014) was used with a filter length of 9 images. For the second set of images with high reflections this filter did not generate desirable results, quite a lot of the reflection remained visible. That is why for these images first the average of all images was subtracted after which the same Butterworth filter is applied. Due to the quasi constant reflection this delivered desirable results with most of the model reflection filtered out.

Particle Tracking Lagrangian particle tracking was used on the acquired images, more specifically the STB algorithm presented by Schanz et al. (2016) was used. This algorithm is implemented in *Davis 8.4.0* and uses Iterative Particle Reconstruction (IPR) with particle prediction. The underlying concepts behind this algorithm are discussed by Jux (2017) and in more detail by Schanz et al. (2016).

Stitching and Binning Because the field of view of the minishaker is roughly 20 cm x 15 cm the entire gap flow could not be captured by one set of recordings. To solve this the gap was divided into a grid consisting of multiple recordings where the next measurement overlapped the previous one by 50% in x or y. After the measurements were taken and the tracking of the particles was done these images had to be brought together in order to see the entire flow field in the gap. This was done in a similar way as described by Jux (2017). First the centre of rotation of the minishaker was determined using an iterative procedure. This allows the user to convert the minishaker coordinates into the coordinate system of the robotic arm. Going from this coordinate system to the model coordinate system is done by a simple rotation and translation. The location of the model was determined by taking images with the minishaker of specific known points on the model and triangulating them using 3D-PTV.

With the coordinates of all the measurements expressed in the model coordinate system multiple runs could be brought together to form the flow field in the gap. The velocities of the particles were converted to a grid of 30 mm with an overlap of 75% which resulted in a final grid with a spacing of 7.5 mm. To remove wrongly tracked particles a filter was implemented which removed those particles with a velocity higher than 3 times the standard deviation. The remaining particles were used to calculate the average at the node using a Gaussian weighting function.

The above described operations were all implemented in a Matlab program written by Saredi.

Pressure Determination Because no direct pressure measurements were performed during the experiment the pressure was reconstructed from resulting flow field obtained from the CVV measurements. This method is based on the work of van Oudheusden (2013) and uses the pressure gradient given by equation 3.8 to calculate the pressure using an antigradient method which transforms the inverse gradient to a Poisson equation Farnebäck (2014).

$$\nabla \bar{p} = -\rho(\vec{\bar{v}} \cdot \nabla)\vec{\bar{v}} - \rho\nabla \cdot (\vec{v'}\vec{v'}) + \mu\nabla^2\vec{\bar{v}} \tag{3.8}$$

van Oudheusden (2013) observed that the viscous terms did not contribute much to the pressure gradient and thus could be neglected which results in the following equation.

$$\nabla \bar{p} = -\rho(\overrightarrow{\bar{v}} \cdot \nabla)\overrightarrow{\bar{v}} - \rho\nabla \cdot (\overrightarrow{v'}\overrightarrow{v'}) \tag{3.9}$$

Using the antigradient method the differences in pressure are calculated. After this the absolute pressure still has to be calculated. This was done by calculating the pressure using the Bernoulli equation at a top plane of the domain after which the pressure was averaged over these values.

3.2 Experimental Results

3.2.1 Single Model

As was done for the numerical analysis first the single model was tested, next to the baseline model the effect of varying the front edge radius and different tail angles were also tested. The section starts off with the effect of Reynolds number on the drag coefficient of the baseline configuration.

Baseline Configuration

Effect of Reynolds Number The velocity at which the experimental campaign was performed was 15 m/s, this gives a Reynolds number based on the square root of the cross-sectional area of 3.9×10^5. For a full scale heavy-duty vehicle the Reynolds number is closer to 5.0×10^6. To see if the difference in Reynolds number has a big effect on the acquired data a Reynolds sweep was performed, the results of which can be seen in figure 3.6.

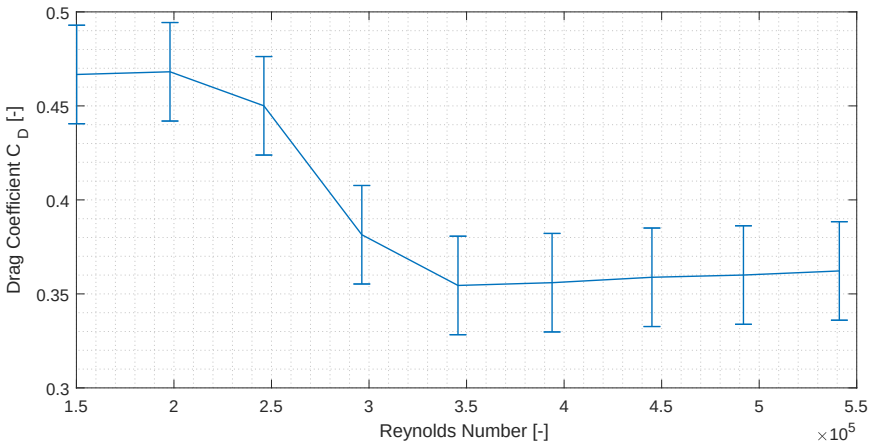


Figure 3.6: Effect of Reynolds number on the drag coefficient of the baseline model along with error bars indicating the uncertainty in drag evaluated at 95% confidence level

From this figure it can be seen that for a Reynolds number higher than 3.5×10^5 the drag coefficient stays about constant. This plateau is typical for a bluff body and was also found by Wood (2012). This Reynolds sweep is similar to the one found in Van Raemdonck (2012) which is to be expected since the same type of model was used.

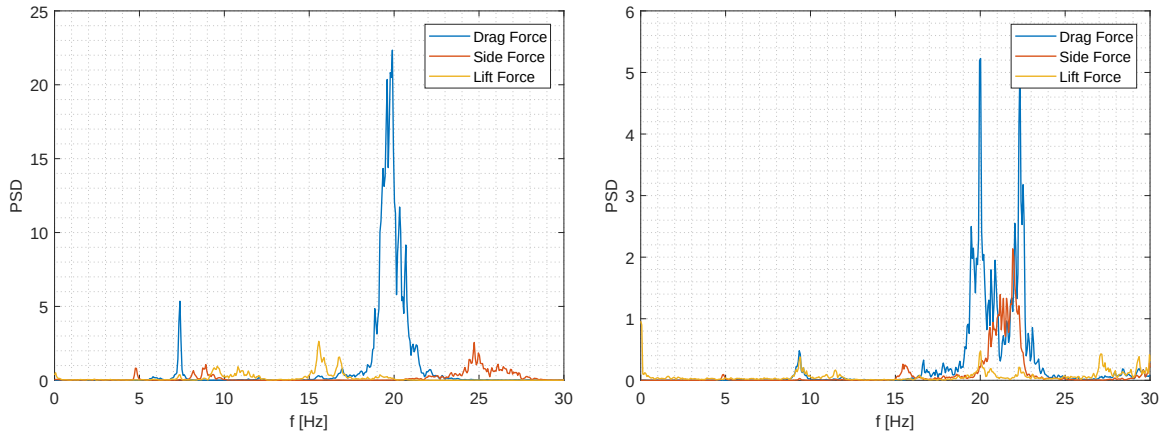
Measurement Uncertainty For any experiment it is of critical importance that during each test run the obtained results are consistent. To check if this is the case each configuration has to be tested multiple times and the measurement uncertainty for each configuration can then be determined. For this study only the baseline configuration was tested multiple times, the results of which can be seen in table 3.2, from this the resulting mean and standard

deviation of the baseline model are 0.327 and 0.013. This standard deviation will be used for the confidence intervals for all the experimental configurations.

Table 3.2: Drag coefficient of the baseline GETS model used for the confidence intervals.

Run	C_D
1	0.311
2	0.320
3	0.323
4	0.329
5	0.329
6	0.349
Mean	0.327
Standard deviation	0.013

Unsteady Forces Because the forces obtained from the balance measurements showed a periodical behaviour the power spectral density was calculated. The results of which can be found in figure 3.7.



(a) Single baseline model

(b) Wooden Disk

Figure 3.7: Experimental PSD of the drag, lift and sideforce

Looking at the lower frequency range in figure 3.7(a) where the peaks are expected it can be seen that the drag and lift force have a peak at a frequency of about 7.4 Hz or a Strouhal number of 0.216. This is higher than expected and closely resembles the shedding Strouhal number of a cylinder. For the side force a peak in the domain is seen around 4.8 Hz giving a Strouhal number of 0.140 which is closer to the values found in literature. Next to this more peaks are visible at higher frequencies which can not be easily explained by the presence of the model. To see if the wooden disk on which the model was mounted causes these fluctuations a dry run was performed for which the resulting power spectral density is given in figure 3.7(b).

From this it can be seen that the peaks at higher frequencies are not caused by the model. The wind tunnel fan is also not the cause of the vibrations since it was spinning at 340 rpm which should result in a peak at 5.7 Hz. The wooden disk itself and other phenomena such as the rotation disk and balance can be the cause of these vibrations but are as of yet not completely known.

Effect of Front Edge Radius

Just as was done in the numerical analysis the effect of a varying front edge radius was also tested experimentally. In figure 3.8 the drag coefficient for the three tested configurations is shown.

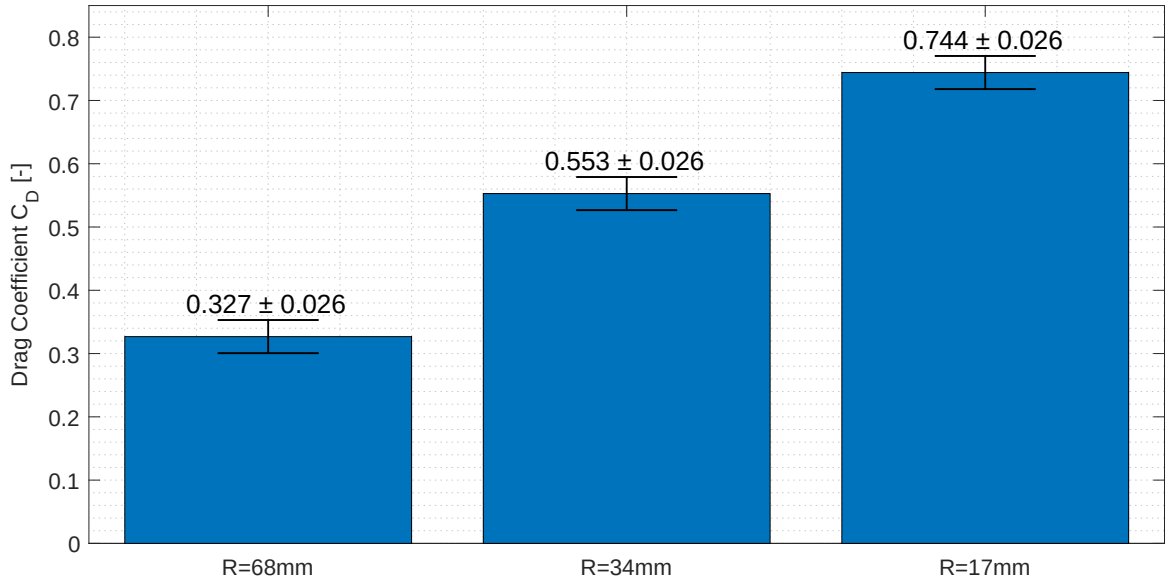


Figure 3.8: Experimental drag coefficient for the single GETS model with different front radii along with error bars indicating the uncertainty in drag evaluated at 95% confidence level

From this figure it can be seen that when halving the front radius a first time the drag is increased by 226 drag counts. Because this is quite a significant drag increase it was decided to do a CVV measurement of the front of the model. In figure 3.9 it can be seen from the negative streamwise velocity and the streamlines that flow separation has occurred which is the cause for the large drag increase. When the radius is halved a second time the drag is increased by an additional 191 counts. Separation was also seen for this configuration.

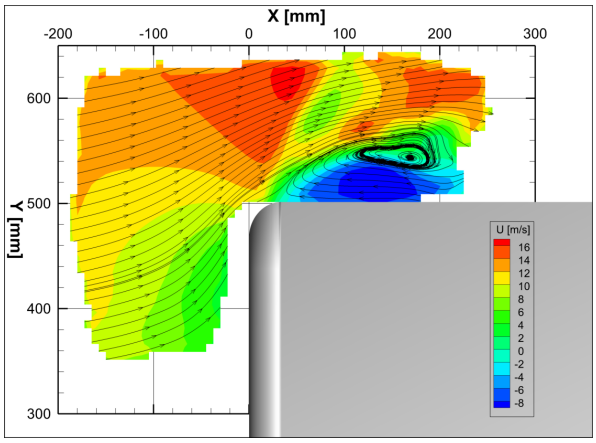


Figure 3.9: Experimental streamwise velocity in the centre plane (z=0) along with streamlines for the single model with a front radius of 34 mm

Effect of Tails

Besides varying the front edge radius of the model tails of different angles were also tested. The tails that were assessed had angles of 0°, 6° and 12°. The results of these configurations can be seen in figure 3.10.

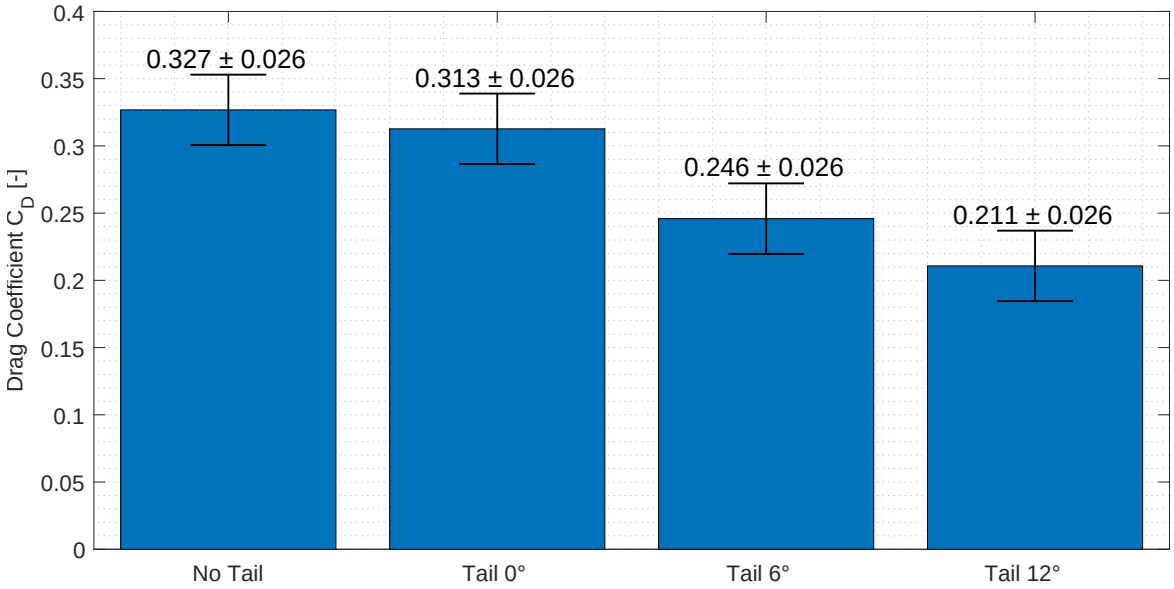


Figure 3.10: Experimental drag coefficient for the single GETS model with different tails along with error bars indicating the uncertainty in drag evaluated at 95% confidence level

From this it can be seen that adding a tail of 0° reduces drag by 14 counts, because this decrease falls in the range of the error bar no concrete statement can be made if this tail

actually reduces the drag. For the tails of 6° and 12° the drag reduction is larger and it can be stated that these tails definitely reduce the drag. For the tail of 6° and 12° the drag reduction is 81 and 116 counts respectively. Not only do the tails affect the average forces, the intensity of the unsteady forces is also altered. In figure 3.11 the power spectral density of the drag and side force is given.

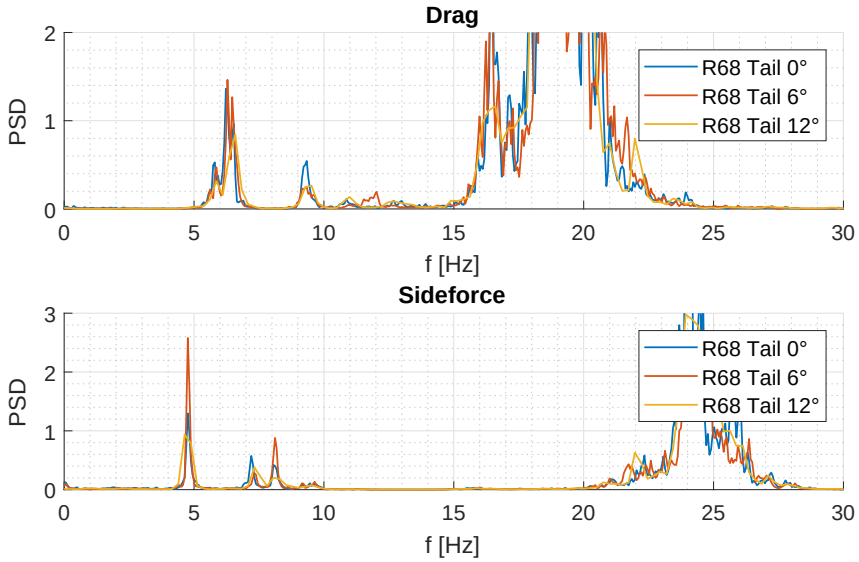


Figure 3.11: Experimental PSD of the drag and side force for the single models with tails

From the figure it can be seen that the fluctuations in drag have diminished compared to the single model. For the tail of 0° and 6° the magnitude of the peak at a Strouhal number of 0.19 (6.5 Hz) is about equal while for the tail of 12° it has been reduced even more. For the sideforce the largest peak is visible at 4.7 Hz which gives a Strouhal number of 0.14. Here the magnitude of the peak is larger compared to the baseline model. It can also be seen that the tail of 6° has the highest magnitude while the tail of 12° has the lowest magnitude of the three.

3.2.2 Platoon

Next to the single models platoons were also tested during the experimental campaign. Initially the platoon was going to be tested at three intervehicle distances 0.10, 0.45 and 0.91 times the vehicle length but due to an unforeseen event which required the entire set-up to be moved backward there was not enough time for the final intervehicle distance.

Intervehicle distance 0.10 s/L

The first intervehicle distance that the platoon configuration was tested at was 0.10 times the vehicle length. The relative and absolute drag results for the trailing vehicle with different

front edge radii are shown in figure 3.12. At this distance all the vehicles benefit from the platoon configuration. It can be seen that the relative gains increase when the front edge radius is decreased. This is because for models with smaller radius the front drag makes up a much larger portion of the total drag and because of this a front drag decrease will be more pronounced than in the case of models with a larger radius.

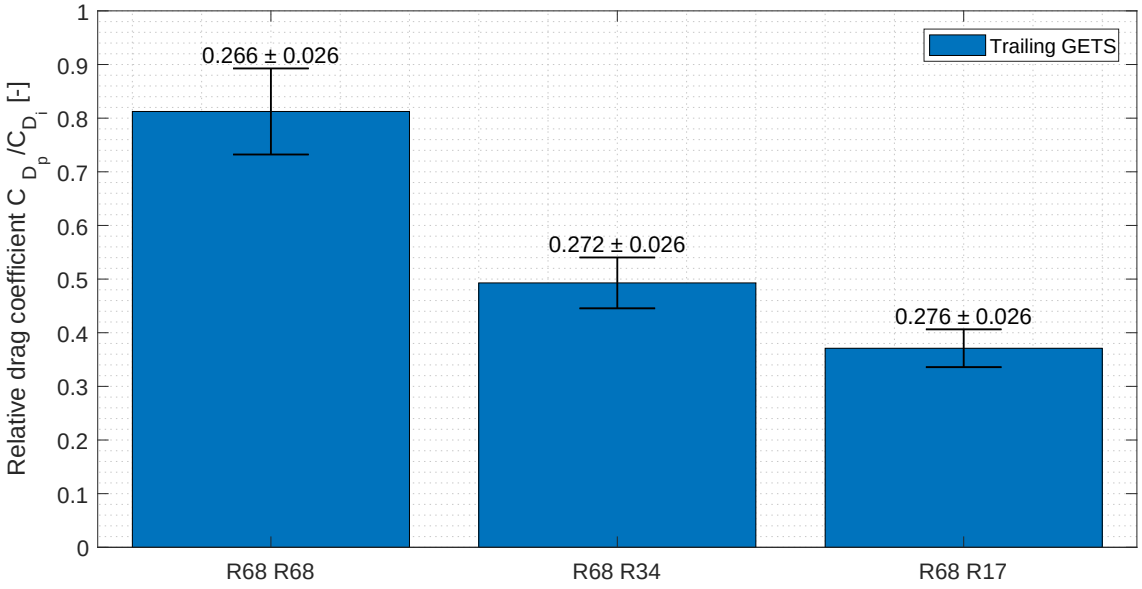


Figure 3.12: Experimental drag coefficient for the platoon at 0.10 s/L with different front edge radii along with error bars indicating the uncertainty in drag evaluated at 95% confidence level.

When it comes to absolute drag stated above each bar in figure 3.12 it can be seen that the differences between the various front edge radii are rather small. In fact the differences are so small that they fall into the measurement uncertainty so no statement about what front edge radii has the lowest drag.

Next to the averaged drag force the unsteady forces were also analysed. The results of this can be seen in figure 3.13.

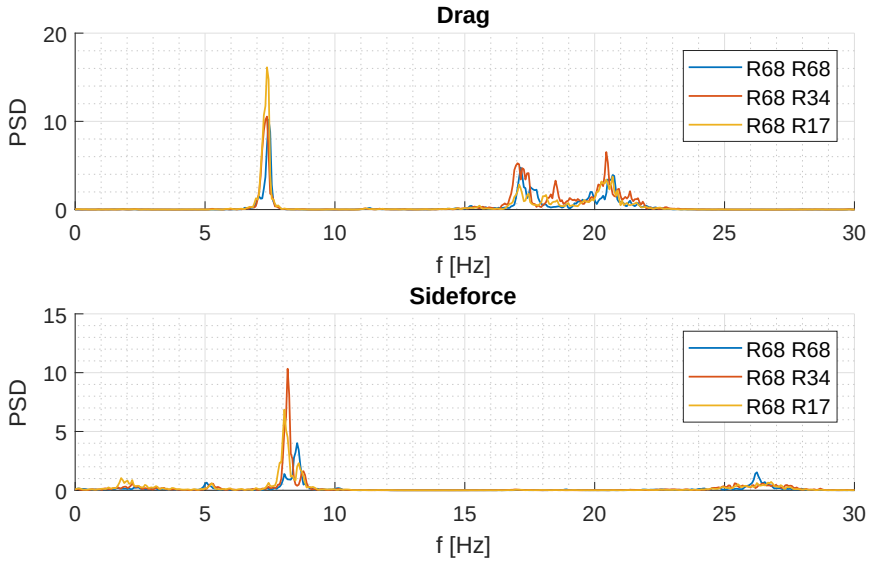


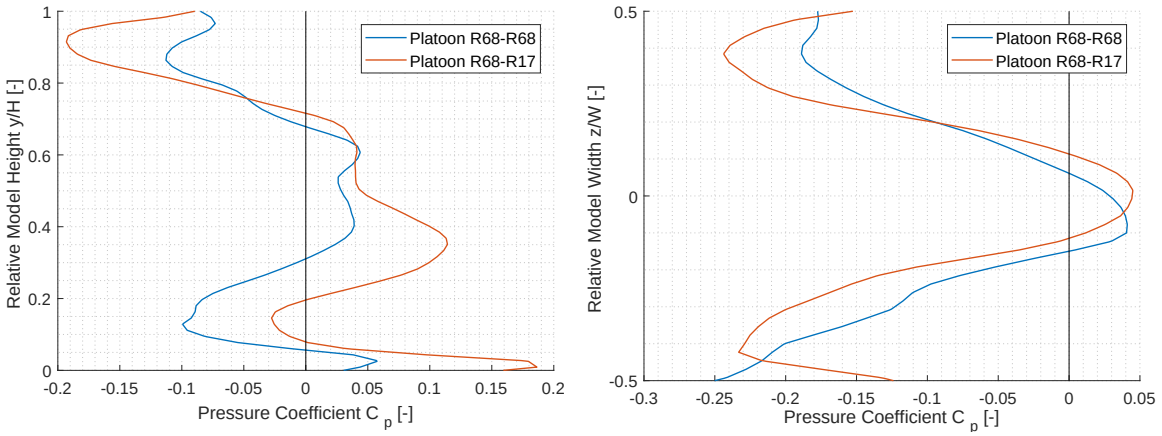
Figure 3.13: Experimental PSD of the drag and sideforce of the trailing model in the platoon at 0.10 s/L

From this it can be seen that the fluctuations in drag and sideforce have been increased compared to the baseline platoon. For the drag a peak for all the configurations can be seen at a Strouhal number of 0.216. The magnitude for the baseline platoon is about twice as high as the single model. This also holds for the model with a front radius of 34 mm. For the model with the sharpest front radius the magnitude is even higher, three times as high as the single model. For the sideforce not only an increased magnitude can be seen but the most dominant peak is now at a Strouhal number between 0.23 and 0.25. The increase in magnitude compared to the single model is about 5, 12.5 and 8 for the models with a radius of 68 mm, 34 mm and 17 mm respectively.

Baseline Platoon: R68-R68 For the baseline platoon the drag reduction of the trailing model is 19% compared to the isolated model. Because one expects most of the drag reduction due to the platooning to come from the front part of the model the pressure on the front surface is investigated.

Looking at the pressure over the vertical centre line in figure 3.14(a) it can be seen that the stagnation pressure, which is assumed to be close to one for the isolated model, has been greatly reduced. Next to this on the top and bottom of the model there is a region of suction. At the very bottom of the model however the pressure coefficient goes from being negative to positive again. For the pressure over the horizontal centre line it must be noticed that the distribution is not entirely symmetric and centred around zero. This can attributed to the fact that the model could have been slightly yawed and was misaligned in the lateral direction. The pressure distribution itself shows a reduced stagnation pressure at the middle of the model which decreases linearly going outward and becomes negative. These pressures can be explained by investigating the flow field between the two models which is what will

be done next.



(a) Vertical centre line z=0

(b) Horizontal centre line y=0.5H

Figure 3.14: Experimental pressure coefficient over the front surface of the trailing model in the platoon at 0.10 s/L

The general behaviour of the flow can be seen by looking at the streamlines which are given in figure 3.15. The flow which is coming from the sides of the leading model either flows past the gap or enters it. The flow that enters the gap rolls up and creates a toroidal recirculation region where it decelerates. In the centre of this toroidal recirculation region the flow stagnates on the rear surface of the leading model. The flow then continues its path and either re-enters the recirculation region or it leaves the gap from the top, bottom or the sides where it is accelerated over the rounded edges and flows further downstream.

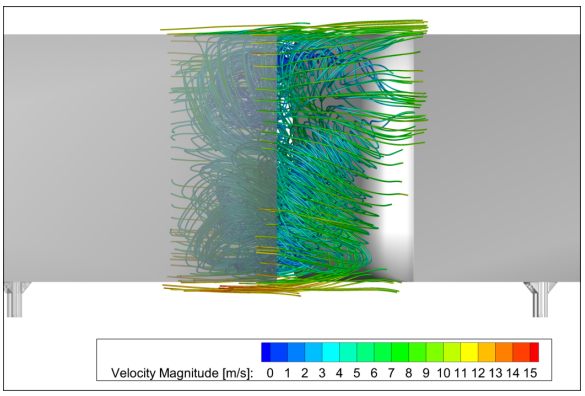
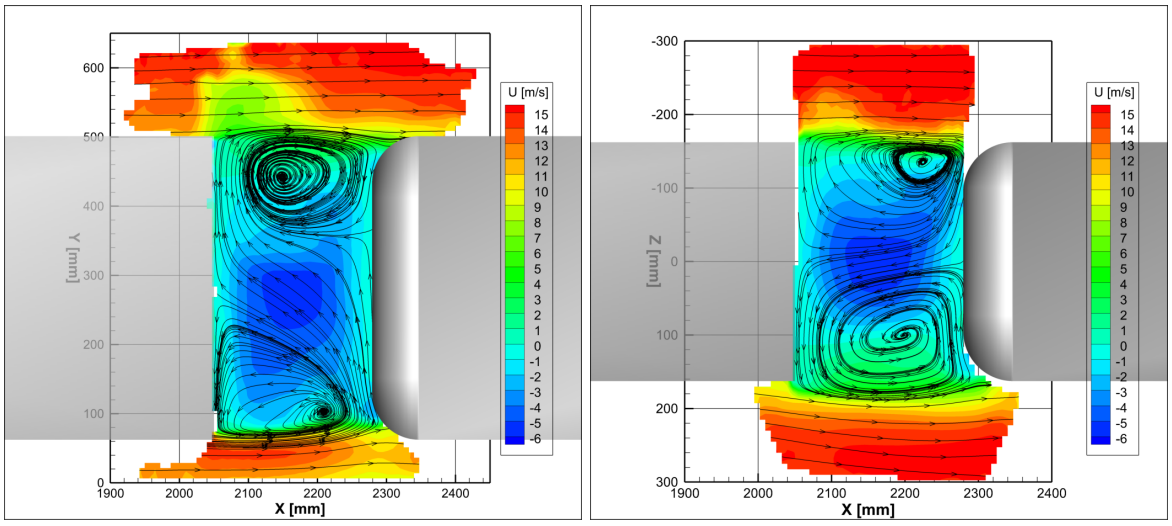


Figure 3.15: Experimental streamlines coloured by the velocity magnitude in the gap of the R68-R68 platoon at 0.10 s/L

The flow field in the vertical and horizontal centre plane is given in more detail in figure 3.16(a). From the vertical centre plane it can be seen that the flow is entering the gap from

the bottom. Part of it stagnates on the bottom edge of the trailing model explaining the positive pressure peak, the rest that continues follows an S-shaped path an exits the gap from the top. On the way to the gap firstly part of the flow is drawn into the vortex at the bottom of the gap which explains the first suction peak. Moving further upwards it can be seen that the flow stagnates on the rear of the leading model. The flow that does not stagnate ends up in the second vortex at the top of the gap or leaves the gap via the top of the trailing model. Because the core of the top vortex is not as close as that of the second vortex the suction on the surface is also slightly lower. The positive pressure that was seen on the surface is caused by the stagnation of the flow on the front surface of the trailing model which can be seen just below the top vortex. Next to the streamlines the distribution of velocity is what was expected. In the gap reversed flow can be seen which is strongest in the centre of the gap. On the outer edges the flow starts to reach the freestream condition of 15 m/s. On the top left of the gap an interesting region can be seen. The figure indicates that the flow has been strongly slowed down but no effect on the streamlines is visible. It is not known what causes this deceleration of the flow.



(a) Vertical centre plane z=0

(b) Horizontal centre plane y=0.5H

Figure 3.16: Experimental flow structure in the gap of the R68-R68 platoon at 0.10 s/L with contours of x-velocity

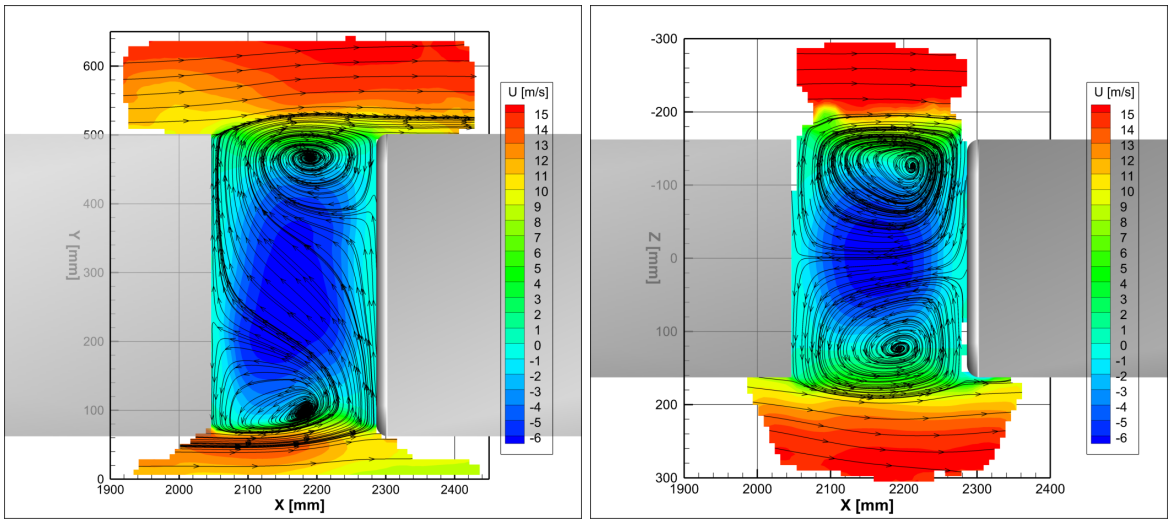
Figure 3.16(b) shows the flow in the horizontal centre plane. The first thing that can be noticed is that the flow is not completely symmetrical when comparing the top and bottom. This can be due to a combination of factors namely the misalignment of the leading and/or trailing model and the fact that the uncertainty in depth of the CVV measurements increases with increasing depth Jux (2017). From the figure it can be seen that no flow is entering the gap from the sides. Inside the gap two counter rotating vortices are present which explain the suction on the front of the trailing model. The high pressure can be explained by the stagnation of the flow which happens in the middle on both the leading and trailing model. In general the flow can be described as follows. Flow coming from the top or bottom enters

the upper vortex where part of it recirculates and leaves the domain from the upper edge. The other part moves down and either ends up in the lower vortex or passes it completely and makes its way out of the gap via the lower edge.

Effect of front edge radius on the trailing model: R68-R17 Next to the baseline platoon the effect of changing the front radius on the trailing model was also tested. When the front radius is halved a first time the drag reduction increases to 51%. A second halving leads to an additional 12% drag reduction. Next to the balance measurement for the sharpest front radius of 17 mm a CVV measurement was also performed. The resulting pressure over the front surface is given in figure 3.14.

From the pressure over the vertical centre line in figure 3.14(a) it can be seen that the pattern is quite similar compared to the baseline platoon. However the magnitude of the peaks of positive and negative pressure are not equal to those of the baseline platoon. On the bottom the positive pressure peak is stronger, moving upwards the suction peak can be seen to be weaker while the positive pressure peak above that is stronger. Finally the suction at the top of the model is also seen to be stronger. Similar statements can be made about the pressure over the horizontal centre line. First of all in this configuration it can be seen that the pressure distribution is symmetric and centred around zero. Next to this the positive pressure peak is very similar to the one of the baseline platoon, the suction on the left and right however is stronger for this configuration. The explanation for this can be given by looking at the flow field in the gap.

Although the general flow field between the two models shows the same phenomena that were noticed for the baseline platoon there are some differences which cause the changes in the pressure. In figure 3.17(a) the same two vortices at the top and bottom that were noticed in the baseline configuration can be seen. The flow still follows and S-shaped path. It enters from the bottom and either ends up in the lower vortex or continues its way upward where it is drawn in the top vortex or exits the gap via the top of the trailing model. The main differences compared to the baseline can be seen when looking at the contours of x-velocity. The region of reversed flow is elongated and stronger. This can be explained by looking at the streamlines. From the bottom it can be seen that more flow enters the gap, because of the sharper front radius the deflection of the flow is stronger which in turn causes a reversed flow of higher magnitude. Due to this reversed flow of higher magnitude the rotation of the vortices is higher which causes the higher suction pressure that was seen on the front of the model. Next to this at the top of the model also more flow is seen leaving the gap, this is probably due to a slight vertical misalignment that was noticed when setting up the experiment.



(a) Vertical centre plane z=0

(b) Horizontal centre plane y=0.5H

Figure 3.17: Experimental flow structure in the gap of the R68-R17 platoon at 0.10 s/L with contours of x-velocity

For the flow in the horizontal centre plane in figure 3.17(b) the first thing that can be noticed is that it is more symmetric than the baseline platoon although asymmetry can still be seen. Also here the stronger reversed flow can be seen which speeds up the rotation of the two vortices and lowers the pressure.

Intervehicle distance 0.45 s/L

The second intervehicle distance at which the platoon was tested was 0.45 times the vehicle length. In figure 3.18 the relative and absolute drag coefficients of the platoon with varying front edge radii is given. The relative drag is indicated by the bars while the values above the bar show the absolute drag.

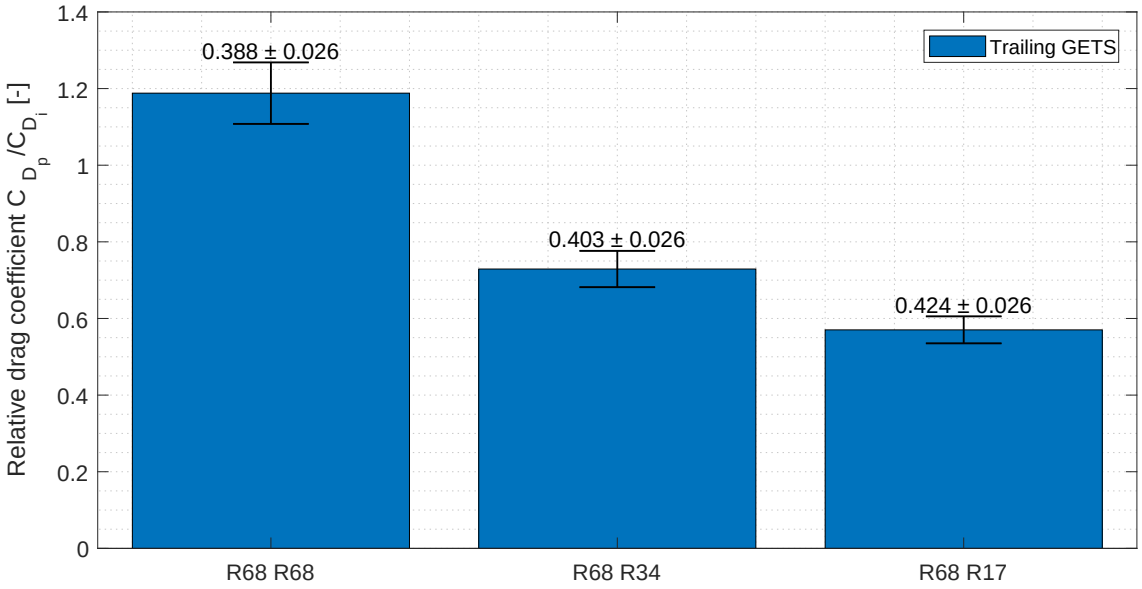


Figure 3.18: Experimental drag coefficient for the trailing model with different front edge radii in the platoon at 0.45 s/L along with error bars indicating the uncertainty in drag evaluated at 95% confidence level.

From the figure it can be seen that the baseline configuration does not benefit from the platoon. On the contrary the drag of the trailing model is 19% higher than the isolated model. It is assumed that the lack of thrust generated by the rounded edges causes the drag increase since this was also seen from the simulation data. For the two models with smaller radii being in the platoon does help them reduce drag. The model with the front radius of 34 mm loses 27% drag and the model with the sharpest radius of 17 mm gains 43% drag reduction. The reason for the increase in drag reduction with sharper front edge radii is the same one that was given for the platoons at 0.10 intervehicle distance.

At this distance the unsteady forces showed an even greater increase in magnitude. This can be seen in figure 3.19 where the PSD of the drag and sideforce is given.

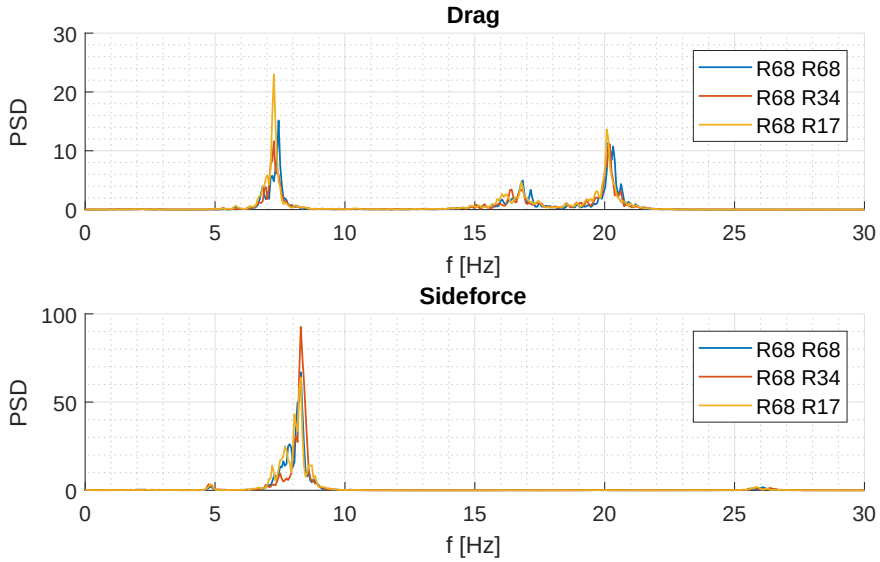
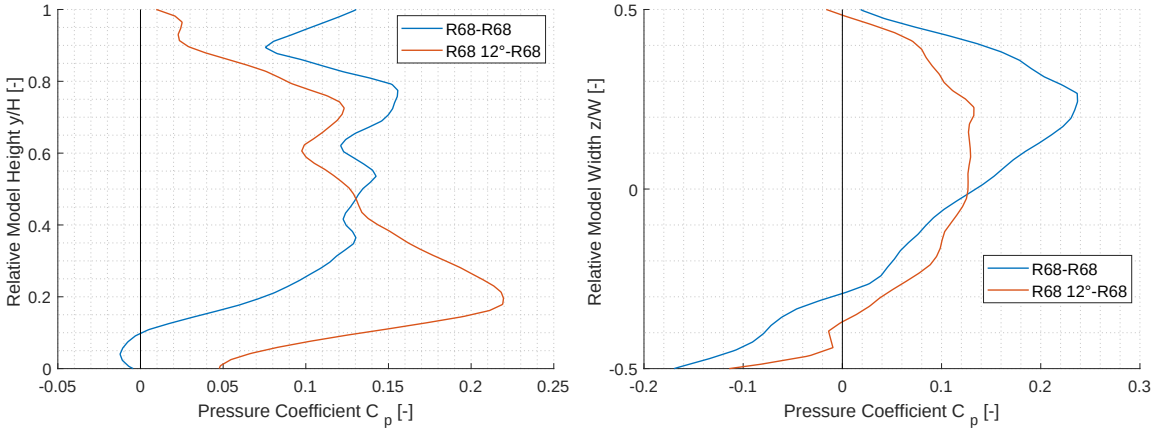


Figure 3.19: Experimental PSD of the drag and sideforce of the trailing model in the platoon at 0.45 s/L

For the drag force a peak for the various configurations can be seen at a Strouhal number between 0.21 and 0.22, the magnitude is about 3, 2 and 4 times higher than the isolated model for the model with a radius of 68 mm, 34 mm and 17 mm respectively. For the sideforce the increase is even higher namely 80, 112 and 78 times the value that was seen for the single model. The location of this peak is at a Strouhal number of 0.24.

Baseline Platoon: R68-R68 Because the increase in drag was shown for the baseline platoon it was decided to perform a CVV measurement on the region inbetween the two models. The resulting pressure on the front surface of the trailing model is given in figure 3.20.



(a) Vertical centre line z=0

(b) Horizontal centre line y=0.5H

Figure 3.20: Experimental pressure coefficient over the front surface of the trailing model in the platoon at 0.45 s/L

Figure 3.20(a) shows that the stagnation pressure, which is assumed to be close to one for the isolated model, is greatly reduced which should reduce the drag. Moving to the top and bottom the pressure decreases even further but still stays positive. For the pressure over the horizontal centre line in figure 3.20(b) roughly the same can be seen. On the front stagnation surface the pressure has been reduced and has a constant value. On the outward parts the pressure decreases but not equally for the left and right parts. For the right part the pressure stays positive while the left part suction can be seen on the very end. Since a symmetric model was used this indicates that the model was misaligned for this configuration which will also become clear when looking at the flow field which will be done next.

In figure 3.21 the general flow in the gap can be seen. From this it can be seen that the flow coming from the leading model enters the gap from the top, bottom and the sides. In the gap decelerates and either is drawn into the recirculation region of the trailing model or flows past the recirculation region and stagnates on the front surface of the trailing model or flows over the rounded edges of the trailing model and accelerates. From the figure it is seen that the recirculation region is made up of a toroidal structure with a stronger vortex on the lower half indicated by the amount of streamlines. The flow in this recirculation region turns inwards and stagnates on the rear surface of the trailing model. After this the flow ends up in the recirculation region again or it leaves it and stagnates on the front of the trailing model or flows over the rounded edges of the model and is accelerated.

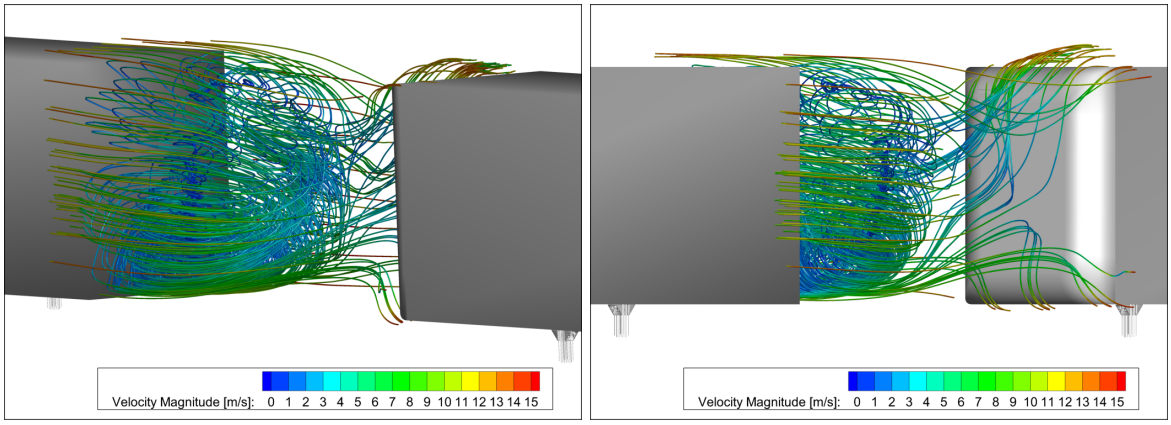
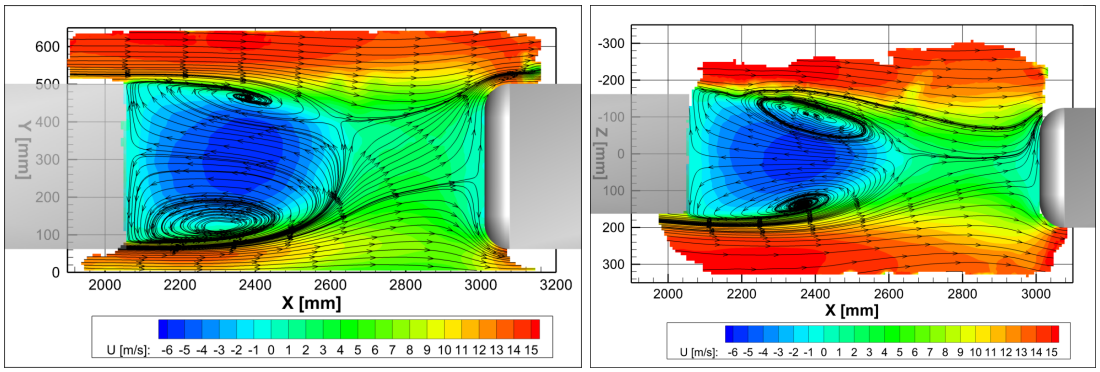


Figure 3.21: Experimental streamlines coloured by the velocity magnitude in the gap of the R68-R68 platoon at 0.45 s/L

The flow field can be seen in more detail in figure 3.22. From the vertical centre plane the lower and upper recirculation region can clearly be seen with the saddle point near the upper vortex. Also here it is clear that more flow is coming in from the bottom and feeds the lower vortex. Part of the flow that does not enter the lower vortex continues and stagnates on the front surface explaining the higher pressure in the middle of the front surface. The flow beneath the stagnation streamline moves down and accelerates when it flows over the rounded edge creating lower pressure as was indicated. The flow above the stagnation streamline moves diagonally upwards and flows over the top rounded edge where it accelerates and leaves the gap. From the top not as much flow is entering the top vortex which was also visible from the streamlines in figure 3.21. Most of it follows a concave trajectory when moving into the gap after which it also flows over the top rounded edge and leaves the gap.



(a) Vertical centre plane z=0 (b) Horizontal centre plane y=0.5H

Figure 3.22: Experimental streamlines with contours of x-velocity in the gap of the R68-R68 platoon at 0.45 s/L

The first thing that stands out from the horizontal centre plane in figure 3.22(b) is that the flow is not symmetric when comparing the left to the right side. This is due to a lateral alignment error between the leading an trailing model. This causes the streamline leaving the saddle point and the stagnation streamline to be different streamlines where they are the same streamline when the model is perfectly aligned. Next to this on both sides the vortices can be seen. The flow coming from the side of the leading model enters there vortices where it is decelerated and its direction reversed. This flow then stagnates on the rear surface of the leading model. The flow that is not contained by the two vortices follows a concave path. Because of the misalignment this path is more curved for the right side than it is for the left. Flow following this path either stagnates on the front part of the trailing model or flows over the rounded edges where it accelerates causing a decrease in pressure. From figure 3.20 it was seen that the pressure decrease was higher for the left side and that for a small part suction was created. This is due to the higher velocity that is seen by the left rounded edge which is caused by the misalignment. The faster flow is accelerated and leads to a lower pressure compared to the one on the right side. From this analysis it is not obviously clear what is causing the drag of the model to be higher. On the one hand the stagnation pressure on the front part is reduced which reduces drag. On the other hand suction was seen on the rounded edges which created a bit of thrust. For the isolated model this thrust could be much higher and in the platooning configuration no suction is created on these edges because of the reduced velocity in the gap. The combination of the reduced stagnation pressure and the loss of suction on the rounded edges means that in total more drag is created in this case.

Effect of a tail on the leading model For the second set of configurations tested at this distance a tail of 12° was applied to the leading model. The drag results of this set-up can be found in figure 3.23. Just as was seen for the baseline platoon the configuration where the model has the most blunt radius gains 16% drag compared to the isolated model. For the two sharper radii the drag is decreased with 29% and 44% for the model with a front radius of 34 mm and 17 mm respectively.

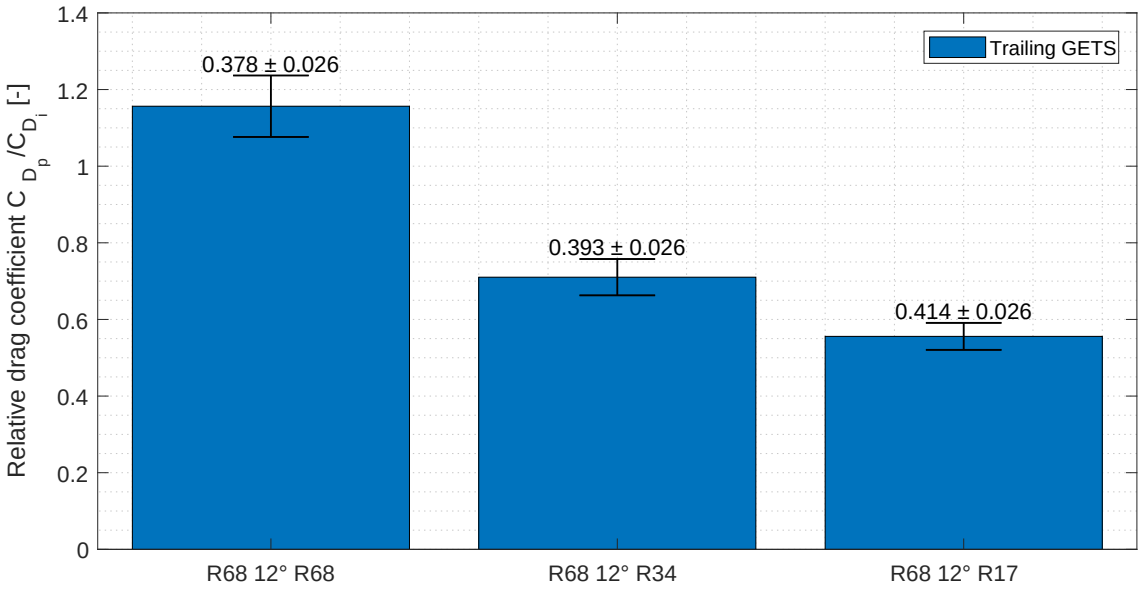


Figure 3.23: Experimental drag coefficient for the trailing model with different front edge radii in the platoon at 0.45 s/L where a tail of 12° was applied to the leading model along with error bars indicating the uncertainty in drag evaluated at 95% confidence level.

Looking at the absolute drag one can see that the values lie very close to the ones where the leading model had no tail. For all the configurations the drag is 10 counts lower. Since this difference is smaller than the error bar of 26 counts no concrete statement can be made about what effect the tail has on the drag of the trailing model.

Due to the tail applied to the leading model the fluctuations in drag force have reduced significantly. This can be seen in figure 3.24 where the PSD of the drag and side force is given.

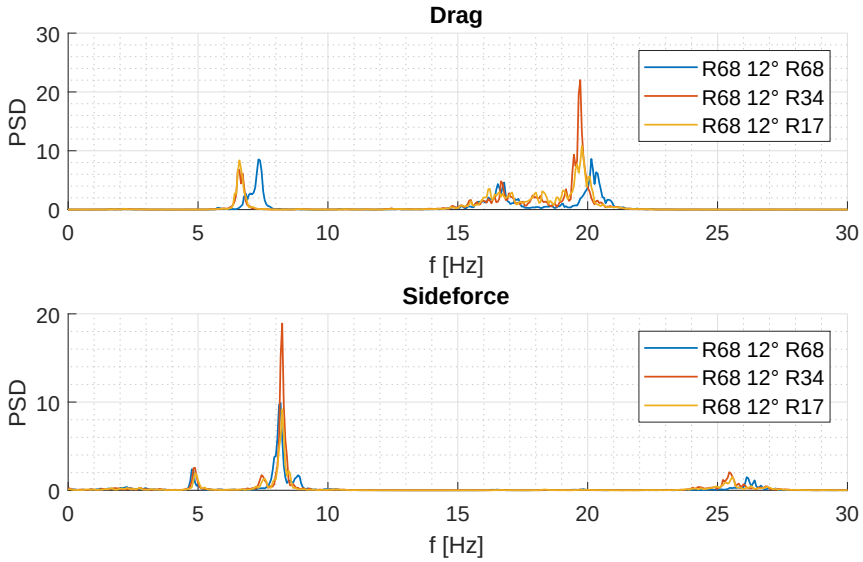


Figure 3.24: Experimental PSD of the drag and sideforce of the trailing model in the platoon with tails at 0.45 s/L

The peaks in drag at a Strouhal number between 0.19 and 0.21 are only slightly higher in magnitude compared to the single model. For the sideforce the fluctuations are still higher two peaks can be seen one is located at a Strouhal number of 0.140 (4.8 Hz) and one at 0.24 (8.2 Hz). The magnitudes of these peaks are about twice as high for the peak at 4.8 Hz and 12, 23 and 11 times as high for the peak at 8.2 Hz for the model with decreasing front edge radii.

For the platoon with the largest trailing front edge radius a CVV measurement was taken. The reconstructed pressure on the front of the trailing model can be seen in figure 3.20. Compared to the platoon where no tail was applied the pressure distribution on the vertical centre line shows quite different behaviour. Moving from bottom to top the pressure starts out rather low, it then rises and reaches a peak at about 20% model height. After that the pressure starts to drop again, a small kink can be seen at about half the model height. At 80% model height the pressure crosses from positive to negative and suction is created. The negative pressure peak at the top diminishes and at the top of the model the pressure is slightly positive again. The pressure on the horizontal centre line is similar to that of the platoon with no tails. At the sides the pressure is low, at the left side it is even slightly negative, and it increases moving inward. Where in the centre of the baseline platoon the pressure was almost constant this can not be seen in this configuration. At the right side the pressure is lower and it increases when moving to the left.

The explanation for these pressures can be given by looking at the flow field in more detail. Figure 3.25 shows streamlines coloured by the velocity magnitude. Although the flow pattern is quite similar to that of the baseline platoon multiple differences can be noticed. First of all the flow is seen entering the gap from the top, bottom and the sides of the leading model just as was the case with the baseline platoon. However since a tail is installed the

flow is more guided while it decelerates. The flow then is reversed and flows into the gap of the tail. In this gap part of the toroidal recirculation region can be seen. Due to the tail the recirculation region is much narrower. The flow in this recirculation region is also not decelerated as much. The flow not contained in the recirculation region follows a concave trajectory. It enters the gap and moves inwards while it decelerates. It then either stagnates on the front surface of the trailing model or flow over the rounded edges where it accelerates again.

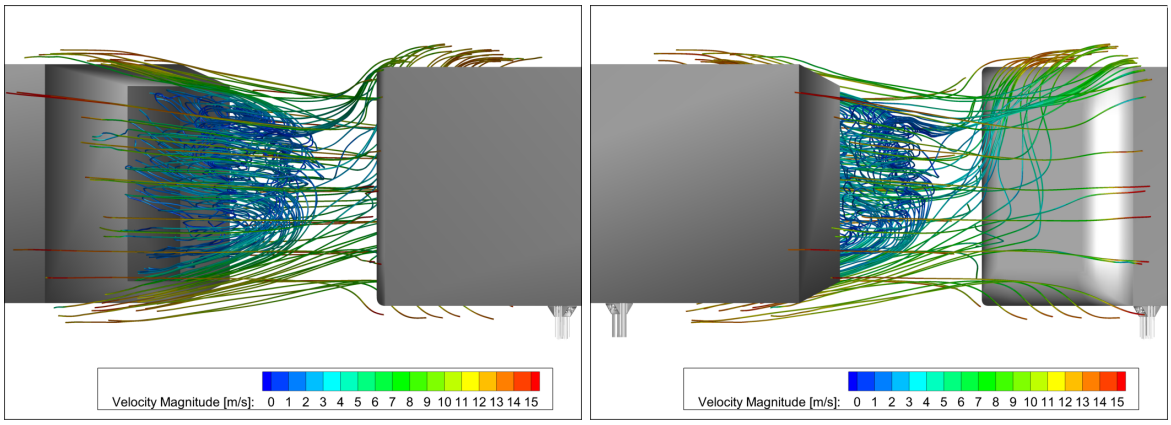
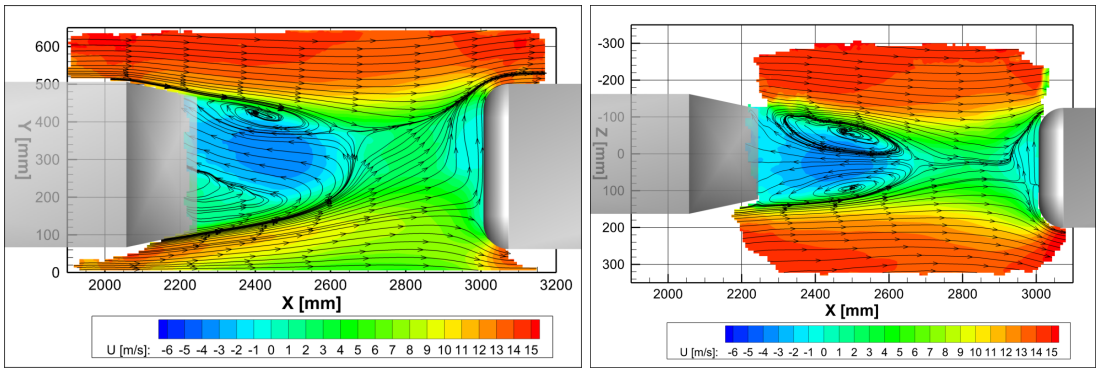


Figure 3.25: Experimental streamlines coloured by the velocity magnitude in the gap of the R68 Tail 12°-R68 platoon at 0.45 s/L

The flow field in more detail is given in figure 3.26. In the vertical centre plane it can be seen that the structure of the recirculation region has changed quite a bit. On top a small vortex can be seen while on the bottom only part what is believed to be the secondary vortex is visible. The flow is still entering the recirculation region from the top and bottom where it then turns and is reversed. The magnitude of this reversed flow however is not as big as it was in the baseline platoon. Next to this the flow that is not entering the recirculation region follows a concave path. From the top the flow moves down and decelerates until it meets the streamline leaving from the saddle point of the recirculation region, there it turns and flows over the top rounded edge and accelerates. From the bottom the flow moves upward and it is divided into two regions by the stagnation streamline. The flow above the streamline continues to move up until it comes near the front surface of the trailing model where it takes a very abrupt turn and is accelerated over the front surface and leaves the gap via the top. The flow below the stagnation streamline follows a slightly concave trajectory and flow over the bottom rounded edge where it is accelerated and leaves the gap. From the pressures in figure 3.20 a bigger stagnation pressure was seen. This can be explained by the up-wash caused by the tail which increases the velocity the flow has when it stagnates. A lower pressure was observed everywhere else which is explained by the lower velocity in front of the trailing model. The suction is probably caused by the sharper turn the flow makes on the front of the trailing model which leads to a higher acceleration.



(a) Vertical centre plane z=0

(b) Horizontal centre plane y=0.5H

Figure 3.26: Experimental Streamlines with contours of x-velocity in the gap of the R68 Tail 12°-R68 platoon at 0.45 s/L

From figure 3.26(b) the same misalignment that was seen in the baseline platoon is visible. Next to this the two vortices in the recirculation region can be seen to be very similar comparing left and right. The flow entering these vortices is coming from the left and right side of the trailing model. As it enters the recirculation region it turns and is reversed flowing in to the gap of the tail. Flow not going in to the recirculation region is seen taking a concave path while travelling towards the trailing model. The flow on the right needs to take a sharper turn compared to the right. This is because of the misalignment. Another effect of the misalignment is the lower pressure on the left of the model. The reason for this is the same that was given for the baseline platoon.

Additional Configurations Because on the last test day the equipment necessary to conduct CVV measurements was not present any more it was decided to do extra balance measurements to see what configuration has the lowest amount of drag and what the effect of the different drag reduction devices is. The results of these measurements are presented in table 3.3 and 3.4 where the drag coefficients are given and figure 3.27 where the drag difference with respect to the baseline single model is shown.

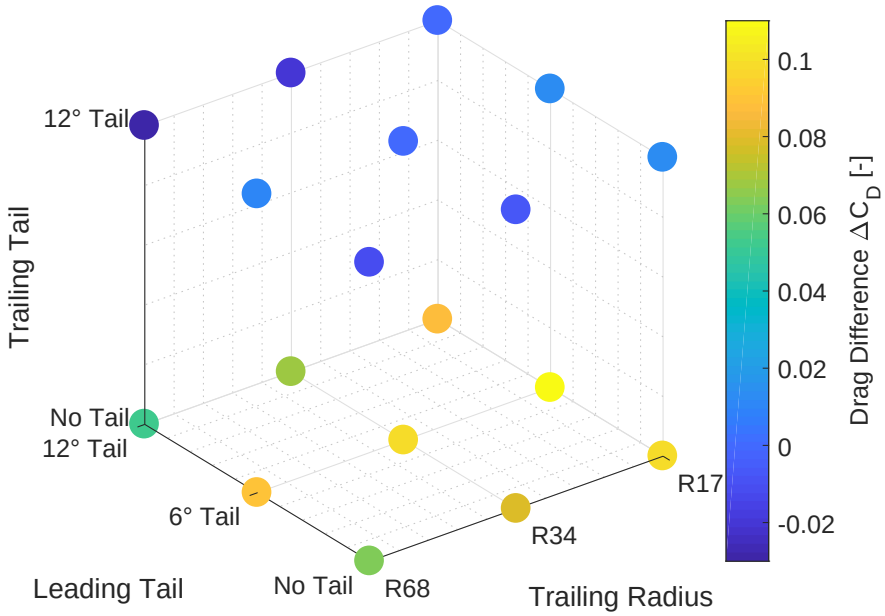


Figure 3.27: Experimental drag difference between the single baseline model and the trailing model in the platoon at 0.45 s/L intervehicle distance for all tested configurations

During these balance measurements three variables were changed namely the tail of the leading model, the front edge radius of the trailing model or the tail of the trailing model. For the tail of the leading model the options were no tail, a tail of 6° or one of 12°. For the trailing model a radius of 68, 34 or 17 mm could be chosen and for the trailing tail the two options were no tail or one of 12°. This lead to a total of 18 configurations. The highest drag is achieved by

Table 3.3: Experimental drag coefficient of the trailing model with no tail in the platoon at 0.45 s/L

		Trailing Radius		
		R68	**R34**	**R17**
Leading Tail	**No Tail**	0.389	0.404	0.426
	6° Tail	0.416	0.425	0.439
	12° Tail	0.379	0.394	0.415

Table 3.4: Experimental drag coefficient of the trailing model with a tail of 12° in the platoon at 0.45 s/L

		Trailing Radius		
		R68	**R34**	**R17**
Leading Tail	**No Tail**	0.315	0.321	0.340
	6° Tail	0.337	0.326	0.339
	12° Tail	0.297	0.306	0.327

the configuration with the leading tail of 6°, the sharpest radius of 17 mm and no tail for the trailing model. The lowest drag configuration is the one where both models have a tail of 12°

and the bluntest radius of 68 mm is applied to the trailing model.

From the figure it can be seen that applying a tail of 12° to the trailing model is always a good idea. All the configurations benefit when a tail is added to the trailing model. Adding a tail to the leading model however is not always a good idea. For every configuration the addition of a 6° tail increases the drag compared to when no tail was added. Adding a tail of 12° however is reducing the drag of every configuration again. It is assumed that when a tail of 6° is added the drag increase is caused by a smaller drag reduction due to the incoming flow of higher velocity compared to when no tail is applied. This faster flow also means more suction is created. The assumption is that this effect is stronger when the tail of 12° is applied which then causes the overall drag decrease. When it comes to front radius the most streamlined model still has the lowest drag. Next to this it is also visible that with a lower front edge radius the model becomes less sensitive to changes made at the rear of the leading model and that the achieved drag reductions decrease with decreasing radius. This is because for a sharper radius the thrust force generated by the front is of less importance since most of the drag reduction is gained from the reduced stagnation pressure which is influenced less by the addition of tails.

Chapter 4

Discussion of Results

This chapter discusses the numerical and experimental results. A comparison between the results obtained from the numerical and experimental analyses and previous studies will be presented after which the differences seen from this comparison will be explained.

4.1 Comparison between numerical and experimental results

In this section the results obtained from the numerical and experimental will be compared against one another. First the results for the single model will be compared after which the platoon configurations are compared.

4.1.1 Single Model

In this section the results from the single GETS model will be compared against each other. First the baseline model will be compared after a comparison between the models with different front edge radii is given. Lastly the comparison between the models with a tail will be presented.

Baseline Configuration

The first results that will be compared are the ones for the baseline GETS configuration. Besides the results from the numerical and experimental analysis done in this study the comparison will also be done against results from previous studies. In figure 4.1 the drag distribution and total drag coefficients for the baseline configuration are given from results obtained during this study as well as results from previous studies.

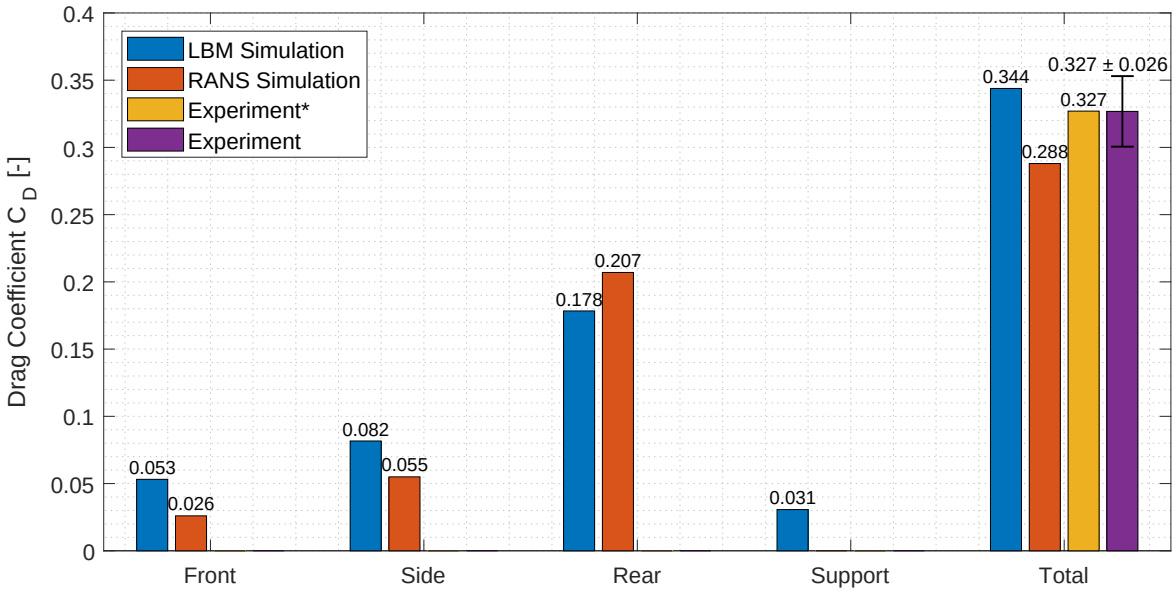


Figure 4.1: Numerical drag distribution and experimental total drag coefficients for the baseline configuration, RANS simulation data from Gheyssens (2016) and experimental* data obtained from Van Raemdonck and Van Tooren (2008)

Before comparing the results first the differences between test conditions from the previous studies will be discussed. Whereas this study uses a 1/8 scale GETS model tested at a Reynolds number of 3.9×10^5 the results from Gheyssens (2016) were obtained for a full scale GETS model without supports and with a moving floor, tested at a Reynolds number of 5.1×10^6, Van Raemdonck and Van Tooren (2008) on the other hand performed a wind tunnel experiment on a 1/15 scale model at a Reynolds number of 8.3×10^5.

Looking at the total drag coefficients in figure 4.1 it can be said that the agreement between the LBM simulation and the experiment performed in this study is very good. The difference is only 17 counts (5%) which falls into the range of the error bar. Besides this the agreement between the results from both experiments is excellent. Both show a drag coefficient of 0.327. The results from Gheyssens (2016) show a lower drag coefficient which is partly due to the lack of supports. Looking at the drag distribution over the various parts it can be seen that the front drag is about half of that of the LBM simulation. This is due to the increased suction generated by the frontal edges which is created because of the higher flow speed. The side drag is also lower, this is due to the lowered shear stress because of the thicker boundary layer at higher Reynolds numbers. Lastly the rear drag is higher than that of the LBM simulation which can be explained by looking at the base pressure given in figure 4.2.

From this it can be seen that the base pressure from the RANS simulation is much lower for the top and bottom 25% compared to the pressure resulting from the LBM simulation. The less negative peak also has a much higher magnitude. Besides this the experimental pressure distribution from Van Raemdonck and Van Tooren (2008) is also given. Comparing this distribution to the one of the LBM simulation it can be seen that the shape is quite

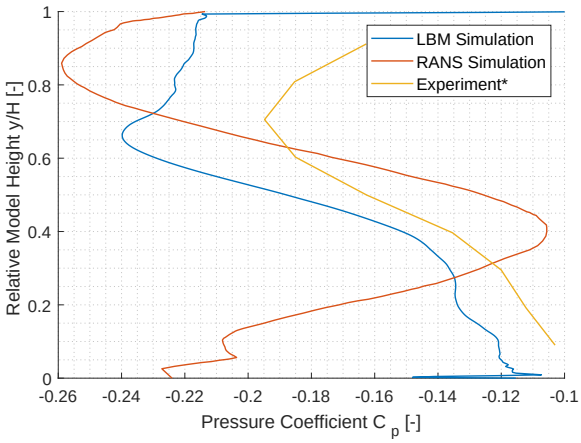
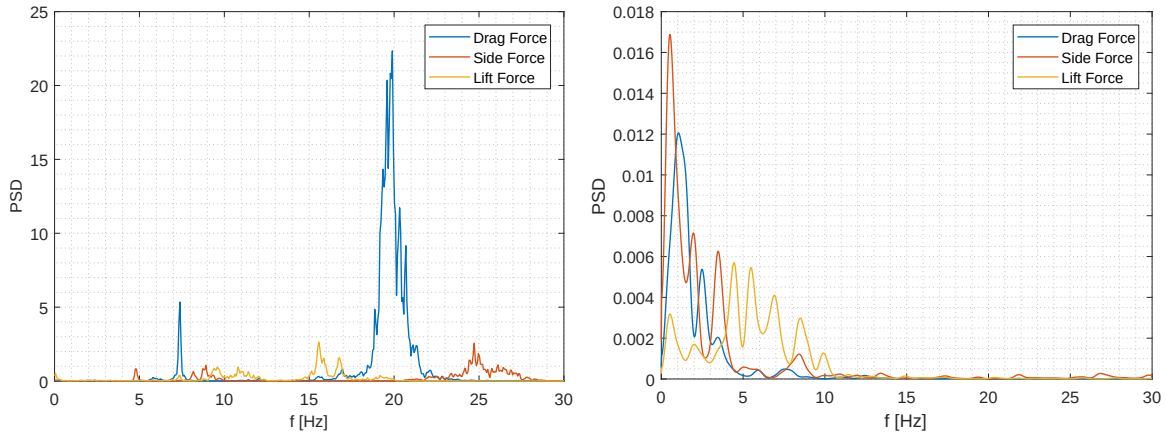


Figure 4.2: Numerical and experimental base pressure distribution, RANS simulation data from Gheyssens (2016) and experimental* data obtained from Van Raemdonck and Van Tooren (2008)

similar, there seems to be an almost constant offset except at the most negative peak which is higher for the LBM simulation.

Next to the averaged forces the unsteady forces of the baseline model were also analysed and will be compared to each other. In figure 4.3 the PSD for the drag, side and lift force is given. The first thing that can be noted from this figure it that the magnitudes of the experimental



(a) Experiment

(b) Simulation

Figure 4.3: PSD of the forces of the baseline model

force fluctuations are several hundreds times higher compared to those of the simulation. Next to this the peaks with the highest amplitude are not located at the same frequencies. For the simulation the highest peak for the drag forces is seen at a Strouhal number of 0.073, which is comparable to the values of 0.07 ,0.073 and 0.069 found by Khalighi et al. (2001) and Krajnović and Davidson (2001) from unsteady base pressure analyses. For the experiment the highest peak is located at a Strouhal number of 0.216 which is closer to the shedding

frequency of a cylinder. For the experimental side and lift force a peak can be seen at 0.140 Hz while for the simulation multiple peaks are seen at Strouhal numbers of 0.058 and 0.102 for the side force and 0.130 and 0.160 for the lift force. From the above analysis it can be stated that the unsteady forces are not comparable between the results coming from the simulation and the experiment. It is assumed that the interaction between the model and the wooden rotation disk on which the model was mounted during the experiments as well as additional vibrations are the cause of the higher fluctuations seen from the experimental results.

Effect of Front Edge Radius

The next results from the numerical and experimental analysis that will be compared against each other are the drag coefficients of the single model with varying front radius which are given in figure 4.4.

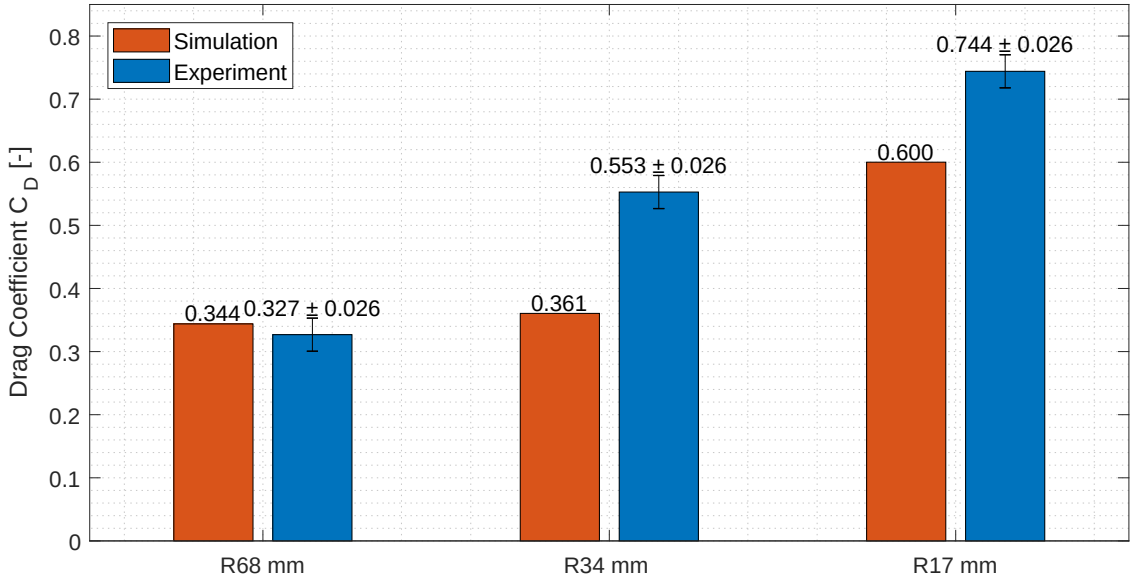
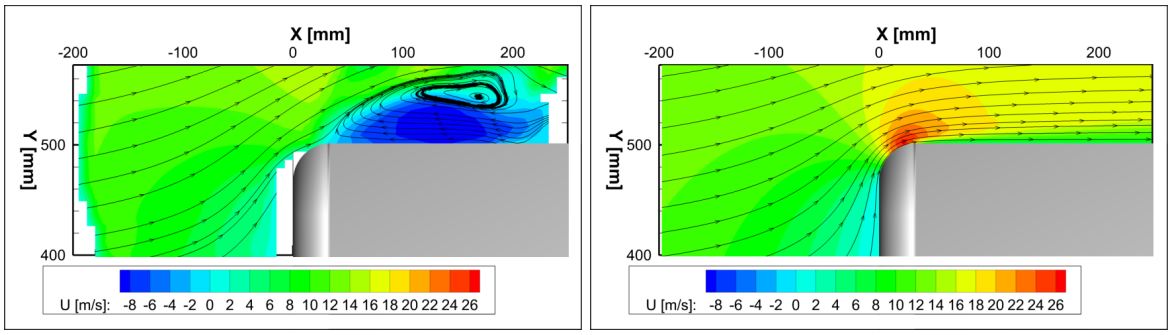


Figure 4.4: Numerical and experimental drag coefficient for the single model with different front edge radii

From this it can be seen that the agreement for the GETS model with the largest front radius is very good as was discussed in the previous section. When the radius is halved a first time the experimental drag is greatly increased this is not the case for the simulation. The difference between the simulation and experiment is 192 counts (53%). Next to a balance measurement also a CVV measurement was taken of this configuration. The results of this can be seen in figure 4.5 together with the flow field from the simulation. In this figure it can be seen that the flow in the experiment is not able to stay attached and separates when it flows over the top edge. This can be seen by looking at the streamlines and the reversed stream wise velocity. For the simulation this is not the case, the flow follows the outline of the model nicely and accelerates over the top edge. This separation then is what causes the large difference in drag. The reason for this lack of flow separation for the simulation

data will be given in 4.2.1. When the radius is halved a second time the drag increases for both the simulation and experiment but the values are not equal. A difference of 144 counts (24%) is observed. For this configuration flow separation was noticed for both models. Since the drag of the experiment is higher it is assumed that the separation is more severe for the experiment.



(a) Experiment

(b) Simulation

Figure 4.5: Streamlines with contours of x-velocity at the front top of the R34 single model z=0

Effect of Tails

Next to the varying front radius different tails were also tested for the model with the largest front radius of 68 mm. In figure 4.6 the difference between the baseline model and the model where a tail is applied is given for both the simulation and the experiment.

When a tail of 0° is applied the drag decreases with 7 counts (2%) and 14 counts (4%) for the simulation and experiment respectively. For the tail of 6° the decrease becomes even larger 72 counts (21%) for the simulation and 81 counts (25%) for the experiment. The final tail of 12° that was applied results in drag decreases of 117 counts (34%) and 116 counts (35%) for the simulation and experiment. From this analysis it can be noticed that the results from the simulation and the experiment agree very well. The differences between simulation and experiment are rather small and all fall in the error bar of the experiment. Next to this the trend of the various tails for the simulation and experiment is very similar.

The effect of tails was also investigated by Gheyssens (2016) and Van Raemdonck (2012) using RANS simulations on a full scale GETS model and a wind tunnel experiment on a 1/15 scale GETS model respectively. The resulting drag decrease was 15 (5%), 87 (29%) and 124 counts (41%) for the tails with increasing angles from the simulation and 90 drag counts (28%) for the tail of 12°,although its length was 30% shorter than the one applied in this study, from the wind tunnel experiment.

From this it can be said that the effectiveness of a tail increases with Reynolds number which was also found by Van Raemdonck (2012). This is because the pressure drag is proportional to the Reynolds number. The tail works by decreasing the negative pressure at the rear of

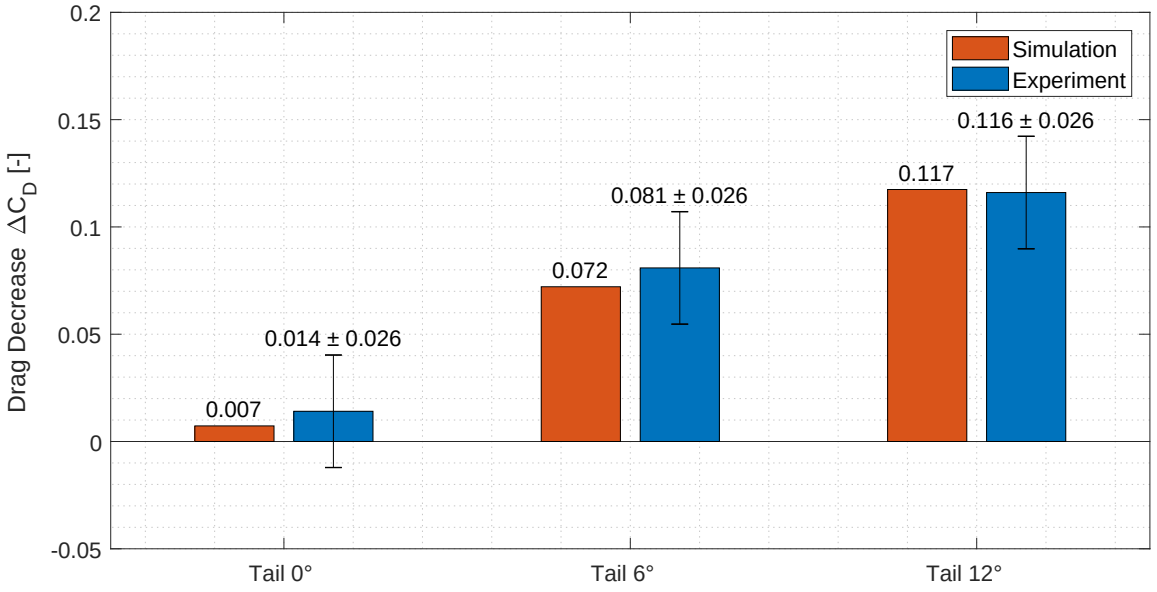


Figure 4.6: Numerical and experimental drag decrease for different tails

the model so the addition of a tail will have a larger effect on the drag at higher Reynolds numbers.

4.1.2 Platoon

Next to the single models the platoon configurations that were analysed both numerically and experimentally will also be compared.

Intervehicle distance 0.10 s/L

At the first intervehicle distance of 0.10 times the vehicle length three simulations were performed. These will be compared against two experiments. In figure 4.7 the drag results of these configurations are presented. Just as was done in the numerical and experimental analyses the bars indicate the relative drag while the absolute values are given above each bar.

For the first platoon where both models have the largest front radius of 68 mm the relative drag reduction is 32% for the simulation and 20% for the experiment. The difference in absolute drag coefficients is 33 counts. From this it can be concluded that the relative and absolute results are pretty far apart. Since during the experiment a small vertical alignment error was noted it was decided to also perform a simulation with this alignment error. For this simulation the drag decrease is much closer to that of the experiment, 18% compared to 20%. The absolute results are also much closer together and only differ 13 counts which is well within the experimental error bar. The second platoon that will be compared is the one

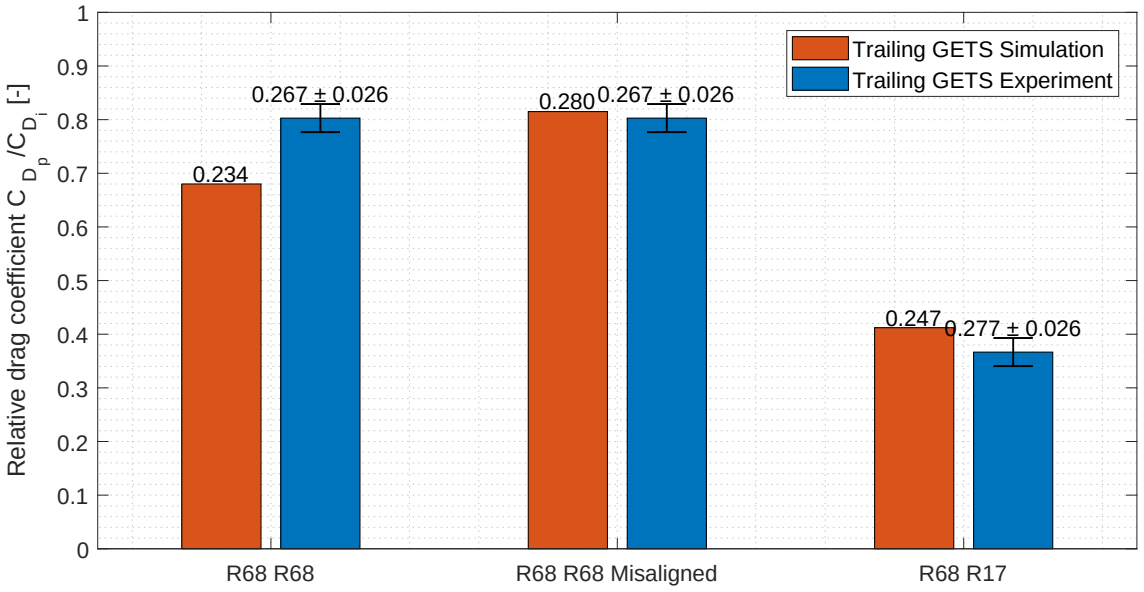
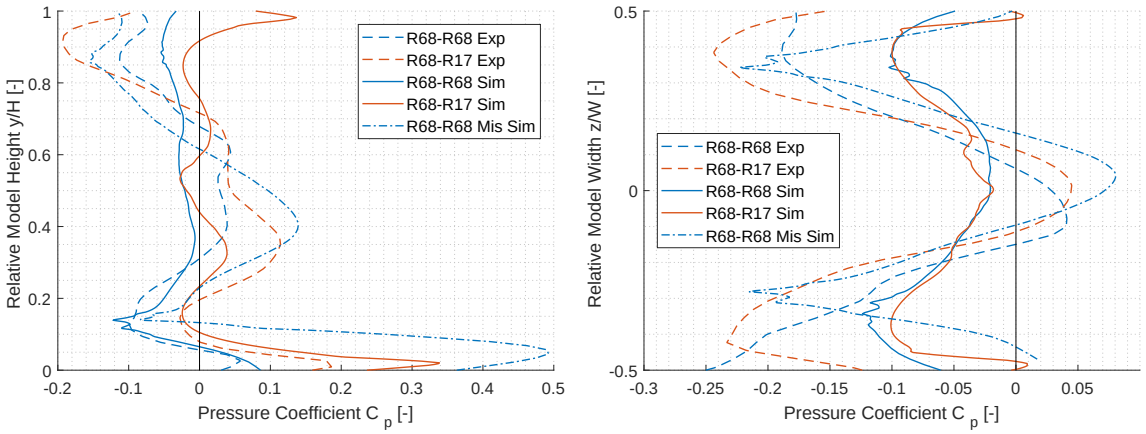


Figure 4.7: Numerical and experimental drag coefficient for the platoons at 0.10 s/L

were the trailing model is applied with the sharpest front radius of 17 mm. The relative drag decreases are 59% and 63% for the simulation and experiment. The differences in absolute drag is 30 counts which just falls out of the experimental error bar. The difference in relative drag coefficient is a combination of the error in the drag of the single model and that of the platoon. The mismatch between the absolute drag coefficient is caused by the vertical alignment error that was also seen in the platoon where both models had the largest front radius.

Next to the drag coefficients the pressure at the front of the trailing model can also be compared. In figure the pressure coefficient is given at the front of the trailing model over the vertical and horizontal centreline. For the baseline platoon it can be seen when comparing the pressures from experiment and simulation they are quite different. Starting from the bottom the pressure is very similar up to the first low pressure peak. After that the pressure in the simulation does not cross over into the positive region whereas the experimental pressure does. The experimental upper peak is weaker than that of the misaligned platoon but stronger than that of the baseline platoon. Since the experimental pressure lies between the ones of the aligned and misaligned platoons it can be stated that the misalignment that was seen during the experiment was not as large as the one simulated. This also holds for the pressure over the horizontal centre line. Next to this a small horizontal misalignment misalignment can also be seen. The experimental pressure for the model with the sharper radius is also not very similar except for a small portion at the lower part of the model where a suction peak is formed. For the rest the extrema of the experimental pressure are higher which can be seen from both the vertical and horizontal centre line. These differences can also be explained by the vertical misalignment.



(a) Vertical centre line z=0

(b) Horizontal centre line y=0.5

Figure 4.8: Pressure coefficient over the front surface of the trailing model in the platoon at 0.10 s/L

Baseline Platoon: R68-R68 Next to the pressures the flow field between the two models will also be compared. In figures 4.9 and 4.10 streamlines with contours of x-velocity are given for the baseline platoon from the experiment and simulation.

From figure 4.9 it can be seen that the flow inside the gap is very similar comparing the experiment to the simulation. Especially the experiment and the misaligned simulation show very similar structures. In both the flow entering from the bottom can be seen to take an S-shaped path through the gap before it leaves at the top of the trailing model. The shape of the two vortices is also very similar. In table 4.1 the location of these vortices is given, from this it can be seen that the y-coordinate of the upper vortex improves for the misaligned simulation. Next to this the difference between the x-coordinate increases for the misaligned simulation both for the upper and lower vortex. For the misaligned simulation the location of the lower vortex is lowered but the difference with respect to the experiment stays the same. When looking at the contours some more differences can be noticed, for the misaligned simulation a stronger reversed flow in the middle of the gap can be seen which can be explained by a small difference in vertical misalignment. In the experiment a region of decelerated flow can also be noticed at the top of the gap. This is not visible in the simulation. Since it is not known what causes this deceleration the reason behind this difference can not be given.

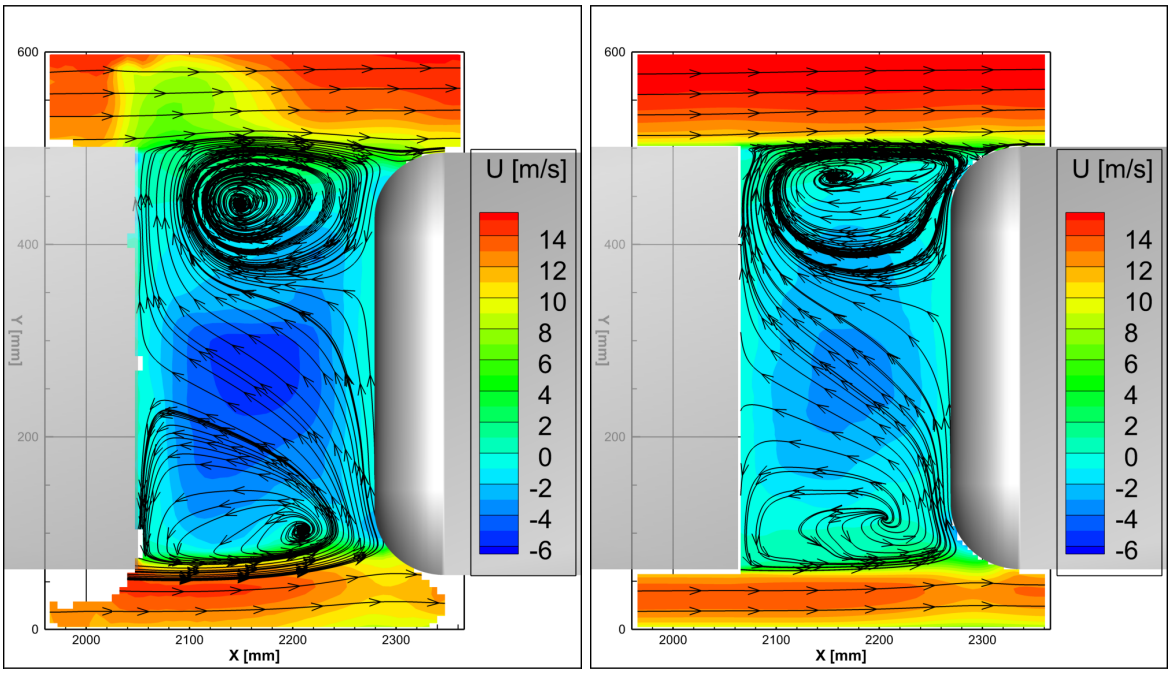
Table 4.1: Vortex core location in the vertical centre plane for the R68-R68 platoon at 0.10 s/L

	Exp		**Sim Aligned**		**Sim Misaligned**	
	x [mm]	**y [mm]**	**x [mm]**	**y [mm]**	**x [mm]**	**y [mm]**
Upper vortex	2149	442	2155	470	2183	440
Lower vortex	2210	103	2205	115	2194	91

The flow similarity is also visible in the horizontal centre plane given in figure 4.10. Looking at the streamlines in the experiment and both the simulations the two vortices on the left and right can be seen. The size, shape and location of these vortices is quite different however, which can also be seen in table 4.2. For both simulations the are symmetric comparing left to right. This is not the case for the experiment. This can be explained by a small lateral misalignment in the experimental set-up. The left vortex of the experiment resembles the one of the misaligned simulation the most, the difference in the location is also quite small. The right vortex from the experiment however is most comparable to that of the aligned simulation. This is not the case for the contours of x-velocity. Looking at the magnitude of the reversed flow it can be seen that the experiment lies somewhere between the aligned and misaligned simulation. This was also seen from the pressure comparison.

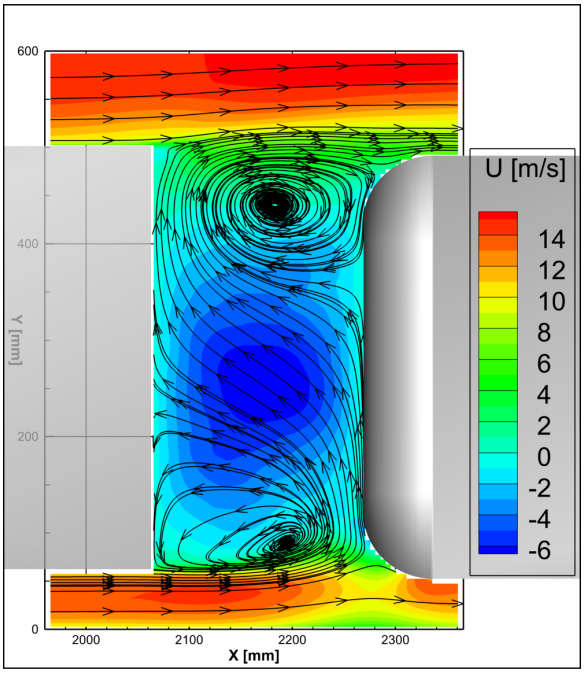
Table 4.2: Vortex core location in the horizontal centre plane for the R68-R68 platoon at 0.10 s/L

	Exp		**Sim Aligned**		**Sim Misaligned**	
	x [mm]	**z [mm]**	**x [mm]**	**z [mm]**	**x [mm]**	**z [mm]**
Left vortex	2198	100	2232	132	2208	119
Right vortex	2225	-136	2241	-128	2206	-125



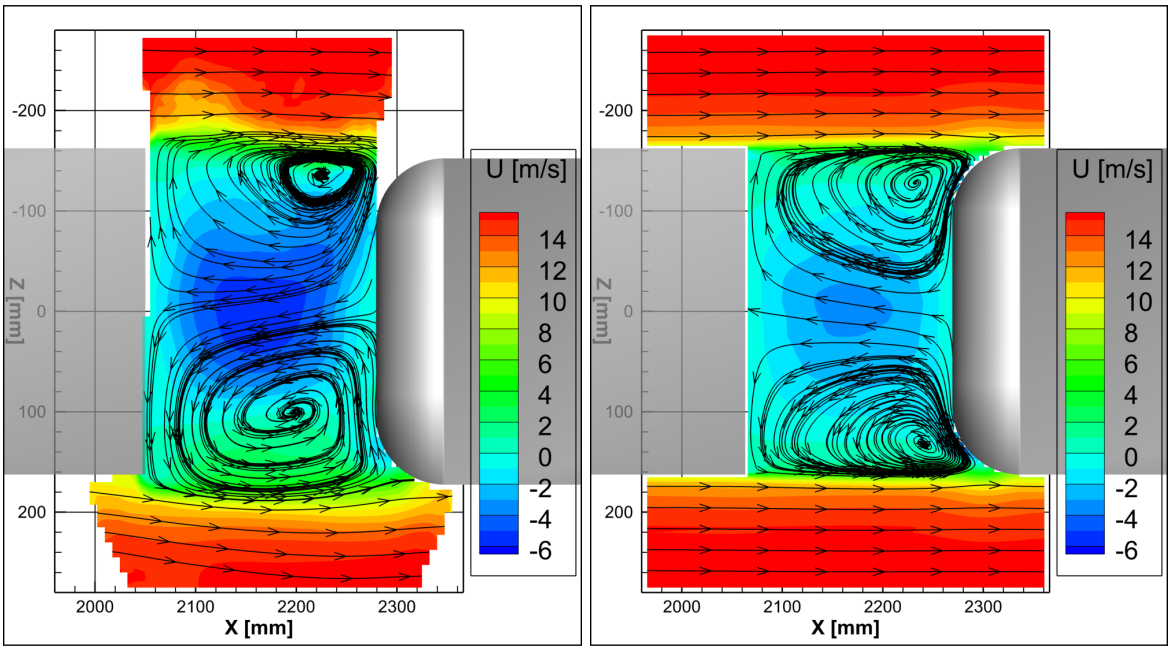
(a) Experiment

(b) Aligned Simulation



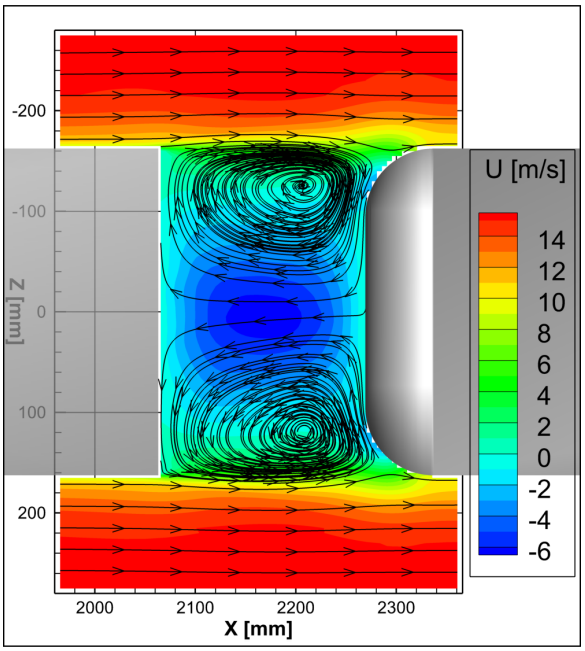
(c) Misaligned Simulation

Figure 4.9: Streamlines with contours of x-velocity in the vertical centre plane of the R68-R68 platoon at 0.10 s/L



(a) Experiment

(b) Aligned Simulation



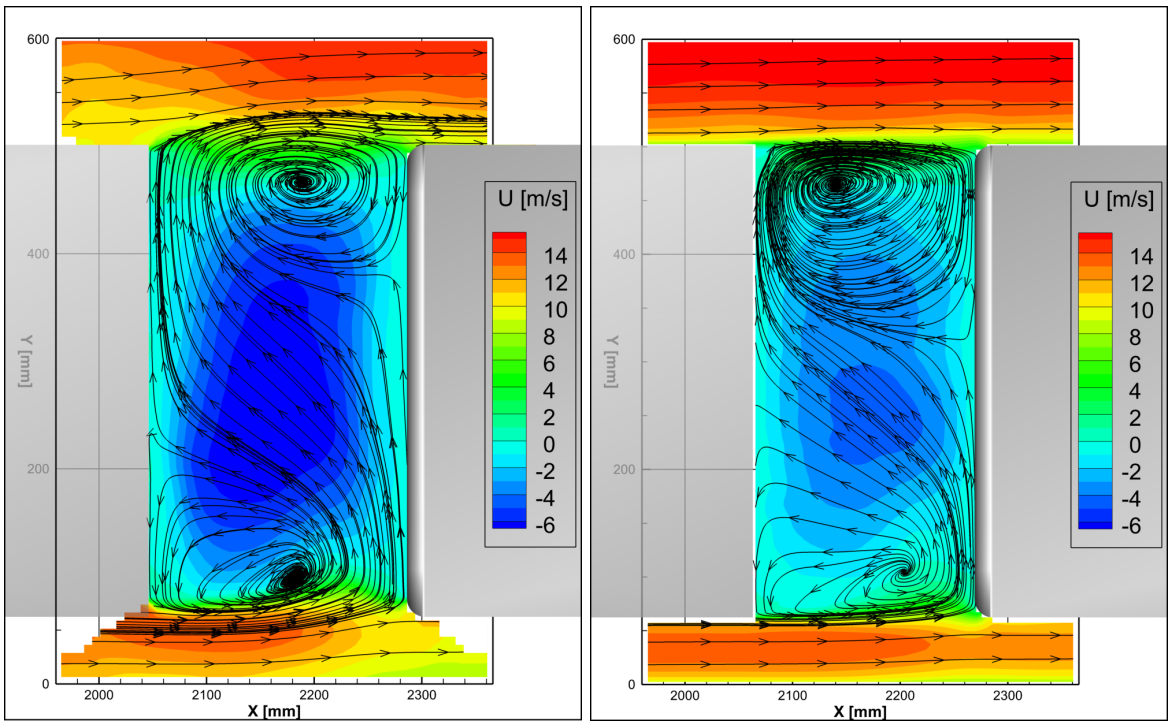
(c) Misaligned Simulation

Figure 4.10: Streamlines with contours of x-velocity in the horizontal centre plane of the R68-R68 platoon at 0.10 s/L

Effect of front edge radius: R68-R17 Next to the baseline platoon the flow field of the platoon where the trailing model had a sharper radius also can be compared. The flow in the vertical centre plane can be seen in figure 4.11. From this it is also visible that this configuration is affected by the misalignment. The flow is similar in saying that it is composed of two counter rotating vortices. However the size, shape and location is quite different. From table 4.3 it can be seen that the y-location of the vortices very similar. The x-location of the upper vortex is located more upstream and the lower vortex more downstream for the simulation which can be explained by the differences in streamwise velocity. The magnitude of reversed flow inside the gap is much less in the simulation. This is an effect of the vertical misalignment as more flow enters the gap and is deflected by the front of the trailing model. This deflection changes the location of the vortices.

Table 4.3: Vortex core location in the vertical centre plane for the R68-R17 platoon at 0.10 s/L

	Exp		**Sim**	
	x [mm]	**y [mm]**	**x [mm]**	**y [mm]**
Upper vortex	2189	466	2140	465
Lower vortex	2182	99	2204	105



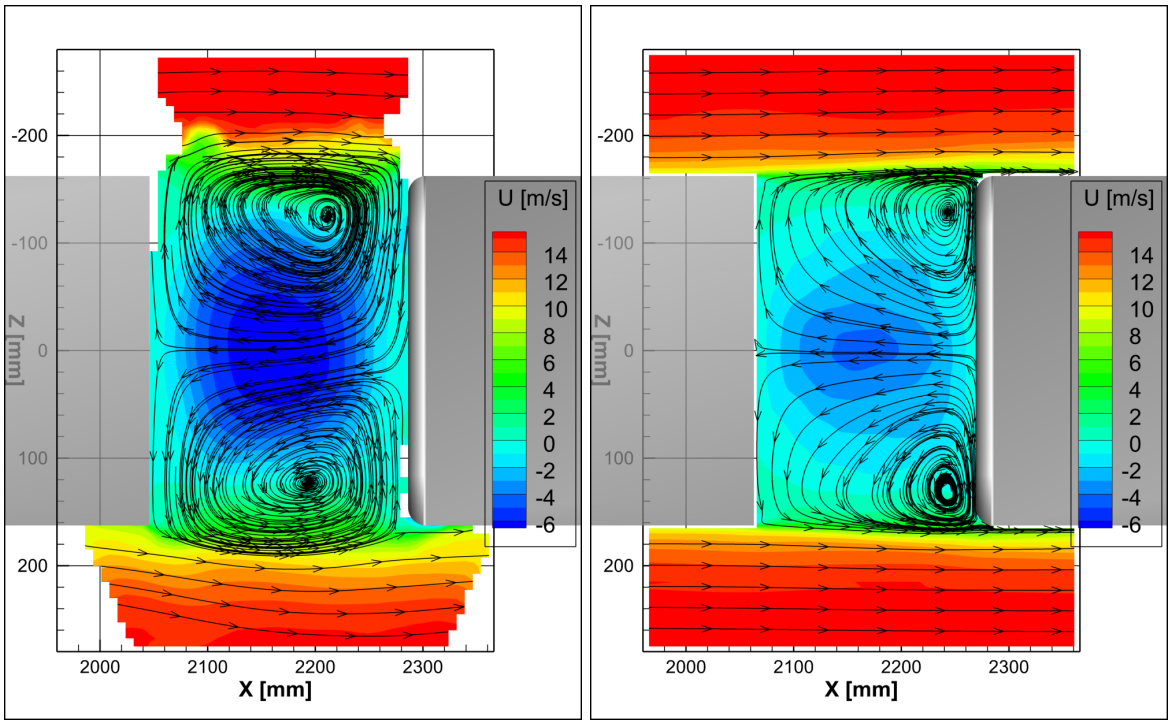
(a) Experiment (b) Simulation

Figure 4.11: Streamlines with contours of x-velocity in the vertical centre plane of the R68-R17 platoon at 0.10 s/L

The effect of the misalignment can also be seen in the horizontal centre plane in figure 4.12. Here the two vortices are also visible but the size, shape and location is not very similar. From table 4.4 it can be seen that the lateral position is very similar but large differences exist when comparing the x-location. This is caused by the higher reversed flow in the experiment which moves the vortex cores more upstream.

Table 4.4: Vortex core location in the horizontal centre plane for the R68-R17 platoon at 0.10 s/L

	Exp		Sim	
	x [mm]	**z [mm]**	**x [mm]**	**z [mm]**
Left vortex	2194	123	2242	132
Right vortex	2212	-125	2242	-129



(a) Experiment (b) Simulation

Figure 4.12: Streamlines with contours of x-velocity in the horizontal centre plane of the R68-R17 platoon at 0.10 s/L

Intervehicle distance 0.45 s/L

For the larger intervehicle distance of 0.45 also three simulations were performed, for these three configurations balance measurement were also taken during the experiment. Next to the balance measurements for two of these configurations CVV measurements were performed

to visualise the flow field. The relative and absolute drag results of these configurations are given in figure 4.13. For the baseline configuration the drag increase for the simulation is

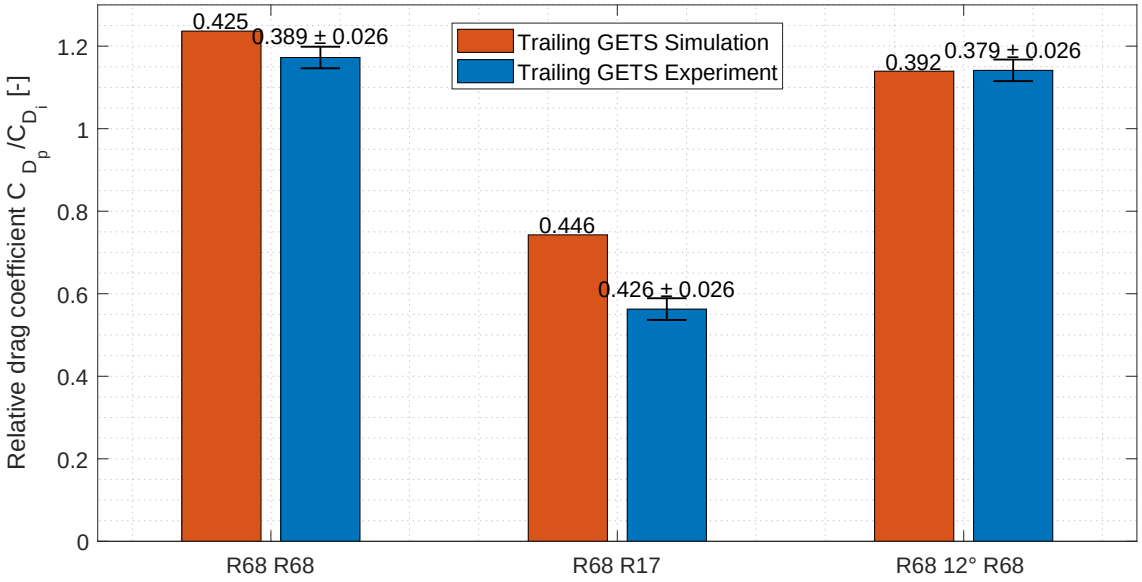
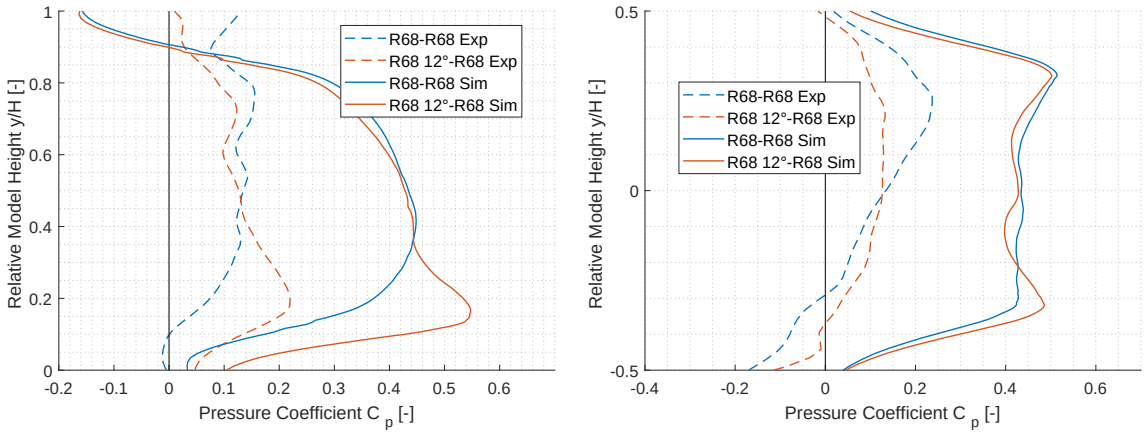


Figure 4.13: Numerical and experimental drag coefficient for the platoons at 0.45 s/L

24% and 17% for the experiment. The difference in absolute drag coefficient is 36 counts which is outside the error bar of the experiment. This difference in drag can be attributed to a lateral misalignment that was seen during the experimental campaign. For the platoon where the trailing model had the sharper front edge radius the drag decrease is 26% for the simulation and 44% for the experiment. The absolute difference in drag is only 20 counts which fall into the experimental error bar. The large difference in relative drag coefficient is caused by the large difference in drag that was seen for the single GETS model with the sharp radius. For the last configuration at this distance which is the platoon where a tail of 12° was applied to the leading model the drag was increased again. For both models the drag increase is 14%, the difference between absolute drag coefficients is only 13 counts.

Besides the averaged forces the pressure at the front of the trailing model will also be compared. In figure 4.14 these pressures are given over the vertical and horizontal centre line. From this figure it can be seen that the experimental pressure is rather different than that of the simulation. For the baseline configuration the simulation shows a suction peak at the top of the model while this is not visible in the experiment. Next to this the stagnation pressure is much lower in the experiment. This can also be seen from the horizontal centre line. For the platoon where a tail was applied to the leading model the same differences can be seen the stagnation pressure is much lower for the experiment. What can be seen is the higher stagnation pressure caused by the upwash of the tail.

Baseline Platoon: R68-R68 For these two configurations CVV measurements were also performed to visualize the flow field. These will now be compared to the results from the



(a) Vertical centre line z=0

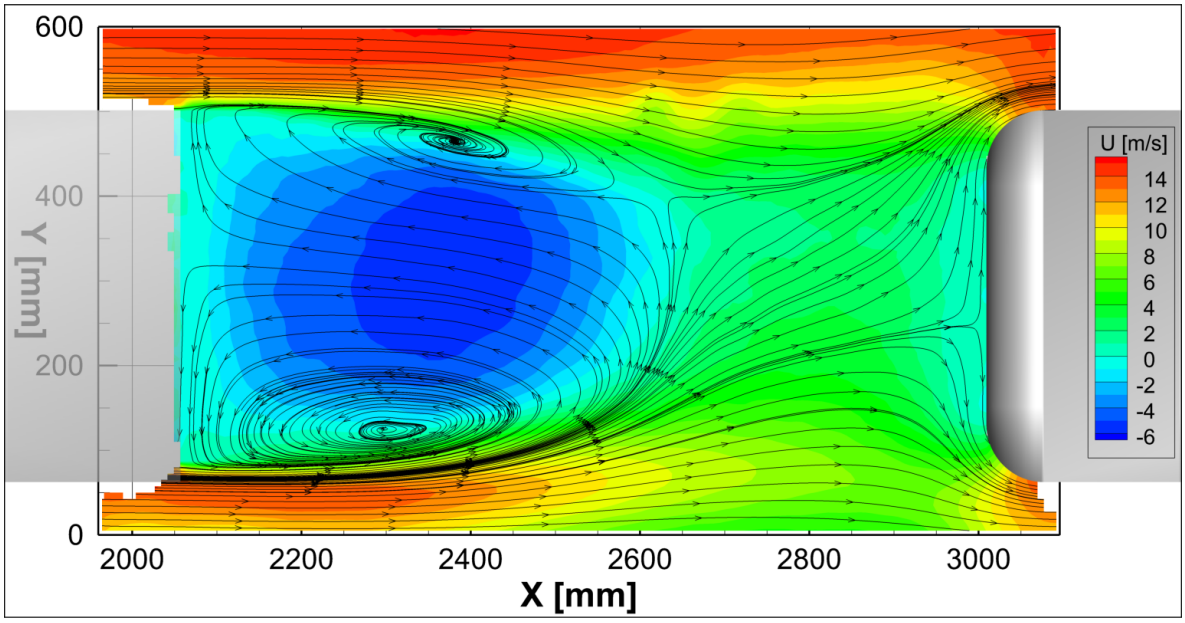
(b) Horizontal centre line y=0.5

Figure 4.14: Pressure coefficient over the front surface of the trailing model in the platoon at 0.45 s/L

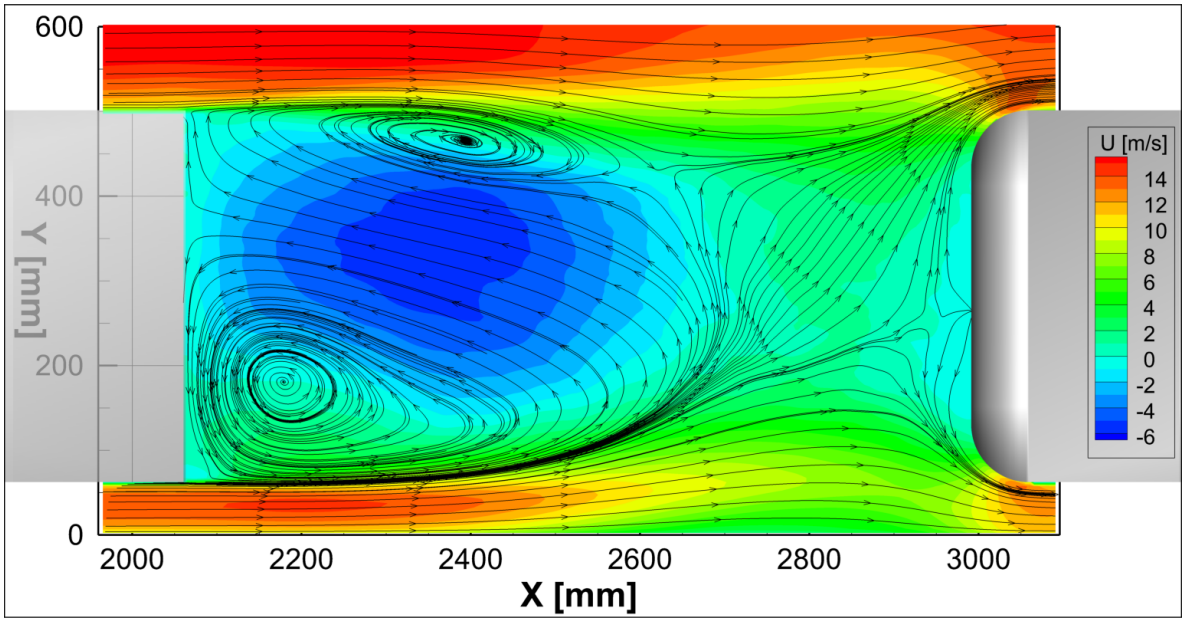
simulation starting off with the baseline platoon. In figure 4.15 the flow in the vertical centre plane is given. In general it can be said that the flow in both the experiment and the simulation is very comparable. Both show the recirculation region with two vortices. The vortex at the top is quite comparable which can also be seen in table 4.5 where the locations of the vortex cores, saddle point and stagnation point are given. There are some differences though, especially for the lower vortex. In the experiment this vortex is much more elongated and its core is located closer to the bottom and more downstream. For the simulation the lower vortex has a more triangular shape and its core is closer to the rear of the leading model. Next to the lower vortex the location of the saddle point is again very similar compared to the experiment. Due to the difference in the lower wake structure the way the flow impacts the trailing model is also slightly different which can also be seen by comparing the location of the stagnation. When looking at the contours of x-velocity it can also be seen that the experiment has a larger region of reversed flow in the wake. This can be due to the lateral misalignment.

Table 4.5: Vortex core, saddle- and stagnation point location in the vertical centre plane for the R68-R68 platoon at 0.45 s/L

	Exp		**Sim**	
	x [mm]	**y [mm]**	**x [mm]**	**y [mm]**
Upper vortex	2380	465	2394	465
Lower vortex	2296	125	2179	181
Saddle point	2603	407	2618	429
Stagnation point	3009	247	2991	264



(a) Experiment



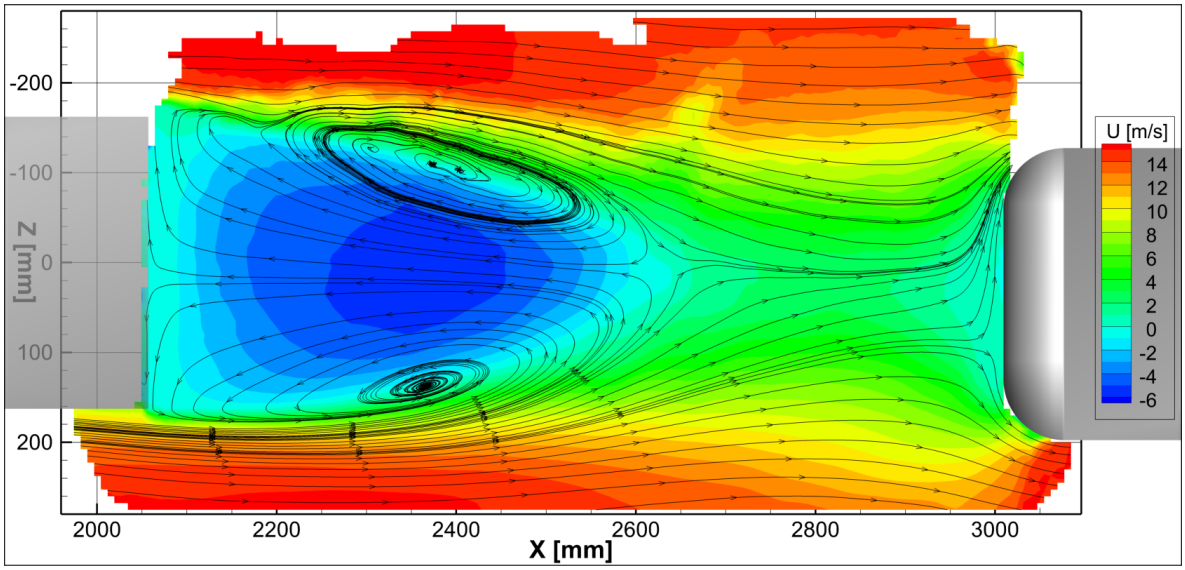
(b) Simulation

Figure 4.15: Streamlines with contours of x-velocity in the vertical centre plane of the R68-R68 platoon at 0.45 s/L

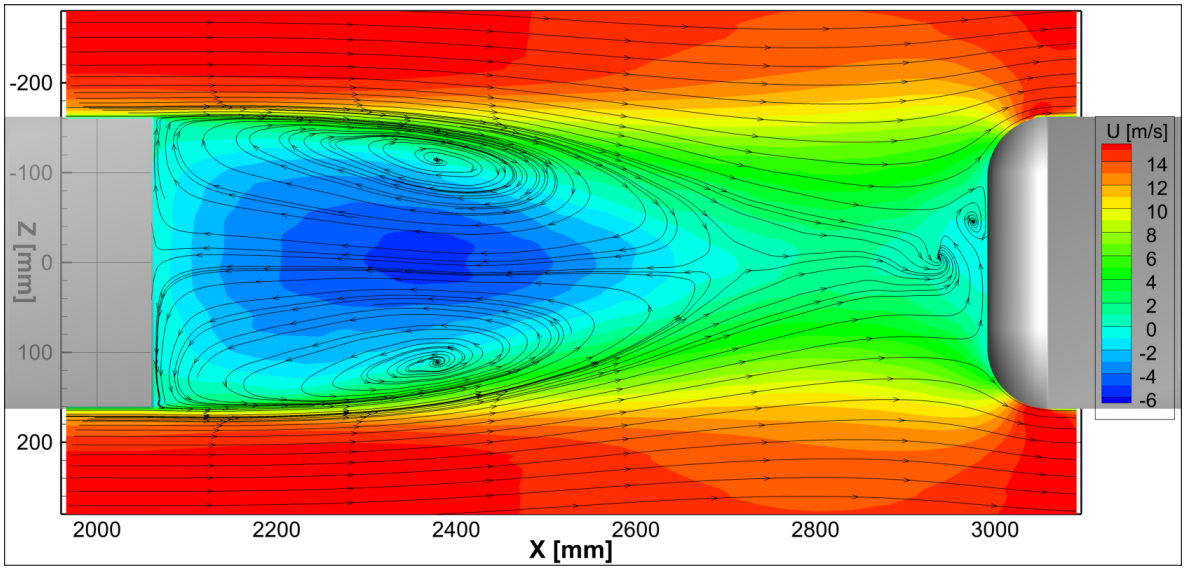
This lateral misalignment can be noticed in figure 4.16 where the flow field in the horizontal centre plane is given for the experiment and simulation. When comparing the wake structure of the experiment and simulation it can be seen that both show the two vortices although a slight asymmetry can be seen from the experimental results, next to this the right experimental vortex also shows two vortex cores instead of a single one. The saddle point in the experiment lies closer upstream than the one from the simulation which is also visible from table 4.6. Also because of the lateral misalignment the experimental stagnation streamline and the streamline leaving the saddle point are not the same. In the simulation no clear streamline leaving the saddle point can be seen. Instead of a clear stagnation point on the front surface of the trailing model a vortical structure appears, which was also seen in the study done by Gheyssens (2016). Just as was seen in figure 4.15 the region of reversed flow is larger in the experiment. Lastly from the experimental data it can be seen that the wake is wider than the width of the model which is not the case for the simulation data.

Table 4.6: Vortex core, saddle- and stagnation point location in the horizontal centre plane for the R68-R68 platoon at 0.45 s/L

	Exp		**Sim**	
	x [mm]	**z [mm]**	**x [mm]**	**z [mm]**
Left vortex	2366	137	2379	111
Right vortex	2374 - 2402	-110 - -103	2378	-114
Saddle point	2628	-1	2709	-7
Stagnation point	3009	93	\	\



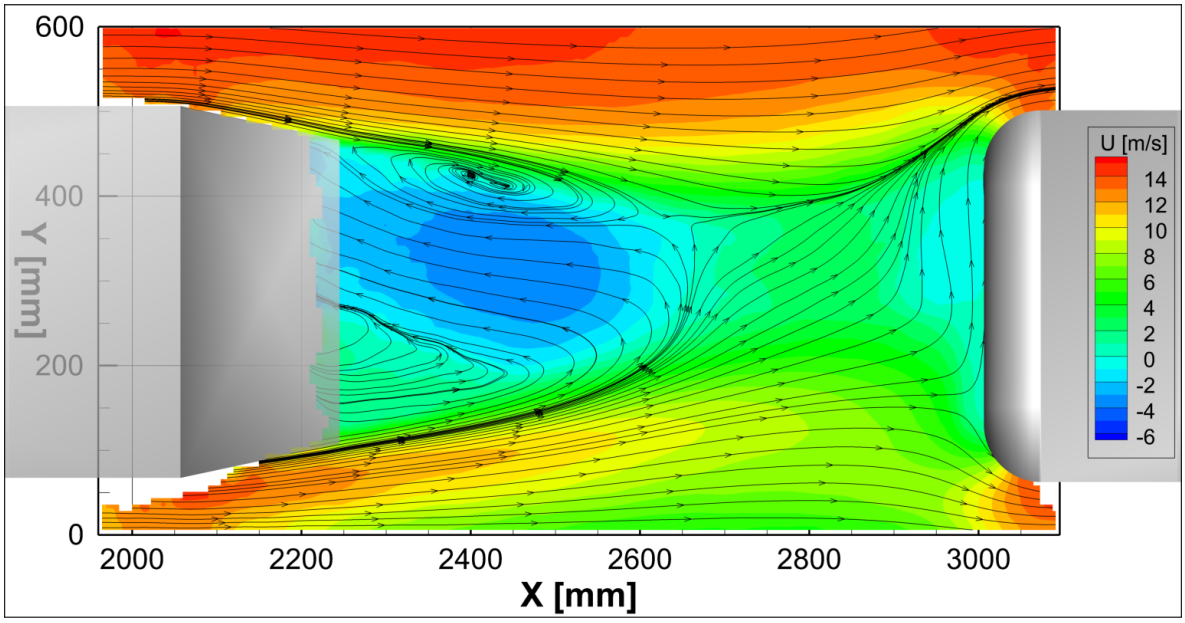
(a) Experiment



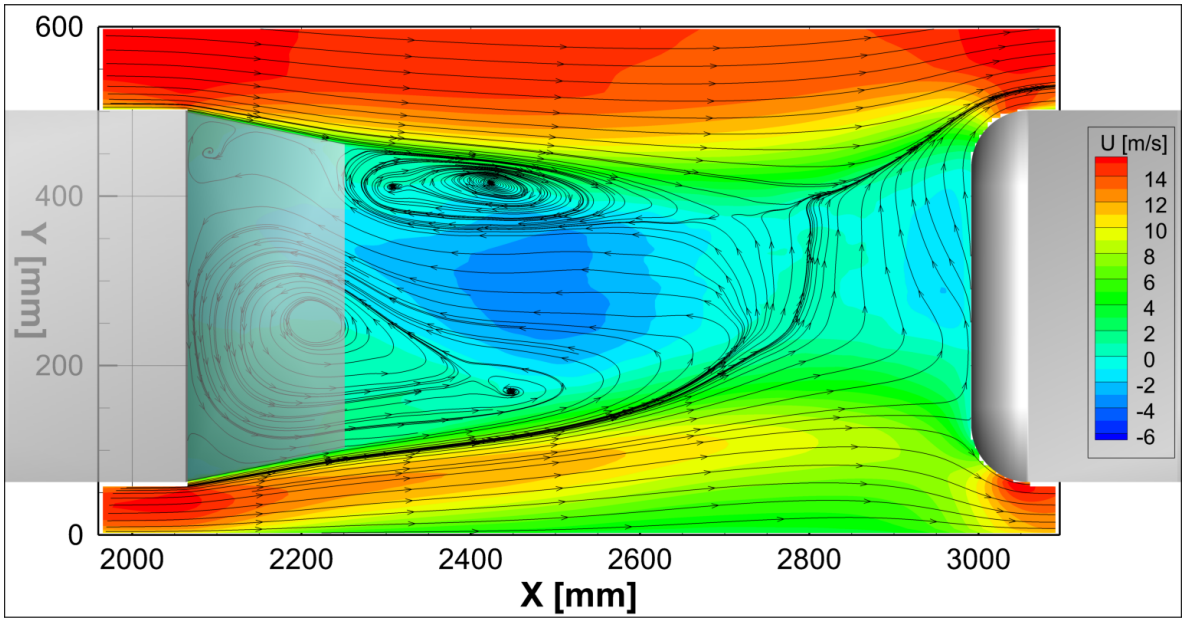
(b) Simulation

Figure 4.16: Streamlines with contours of x-velocity in the horizontal centre plane of the R68-R68 platoon at 0.45 s/L

Effect of Tail applied to the leading model: R68 Tail 12°-R68 The flow field when a tail is applied to the leading model will be compared next. In figure 4.17 the flow in the vertical centre plane is given. At first sight the flow pattern between experiment and simulation is very similar. In the recirculation region two vortices can be seen, one of them at the top and



(a) Experiment



(b) Simulation

Figure 4.17: Streamlines with contours of x-velocity in the vertical centre plane of the R68 Tail 12°-R68 platoon

one at the bottom which extends into the tail gap. The location of the vortex cores is given in table 4.7. The location of the top vortex is very similar however an extra small vortical

structure can be seen in the simulation which is not visible from the experimental data. Next to this the flow between the top and bottom is divided by the streamline leaving from the saddle point of the recirculation region. Which lies more upstream for the experimental data. This streamline moves upwards and flows over the top of the trailing model. Looking at the contours of the streamwise velocity it can be seen that there exists great similarity between the experiment and simulation results. In the wake of the leading vehicle the region of reversed flow is very similar. In the region between the wake and the front of the trailing model the simulation shows slower flow than the experiment this is also the case in front of the trailing model. Lastly the upwash coming from the tail is more pronounced in the results coming from the simulation. The reason behind these differences will be explained in section 4.2 but part of it is due to the lateral misalignment that can be seen in figure 4.18. Here the flow field

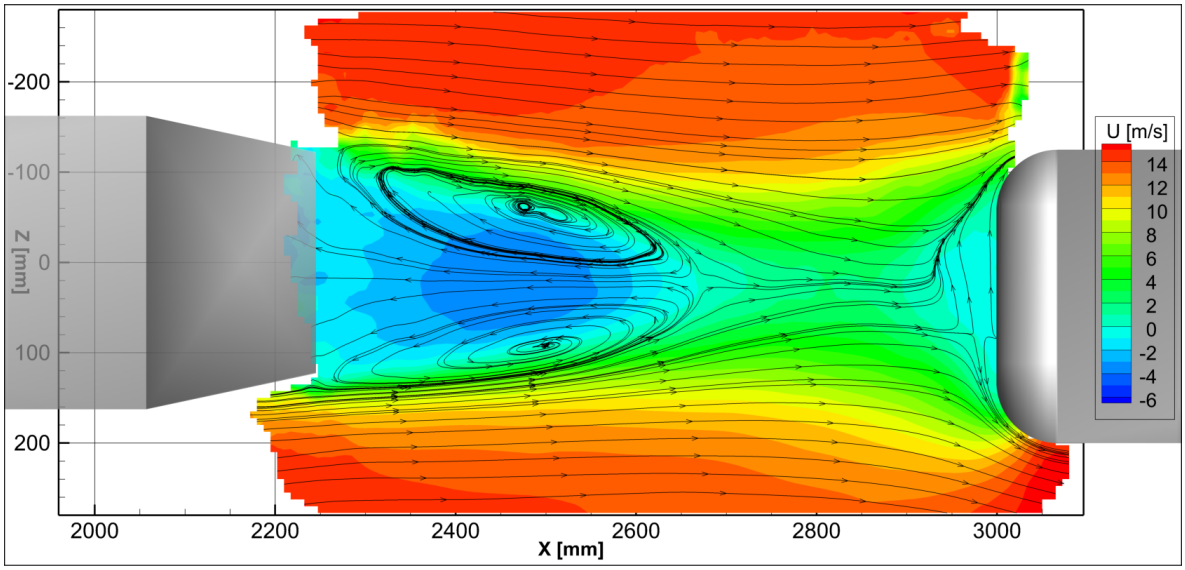
Table 4.7: Vortex core, saddle- and stagnation point location in the vertical centre plane for the R68 Tail 12°-R68 platoon at 0.45 s/L

	Exp		**Sim**	
	x [mm]	**y [mm]**	**x [mm]**	**y [mm]**
Upper vortex	2401	425	2424	416
Lower vortex	\	\	2448	170
Saddle point	2625	374	2699	377
Stagnation point	3006	157	2995	132

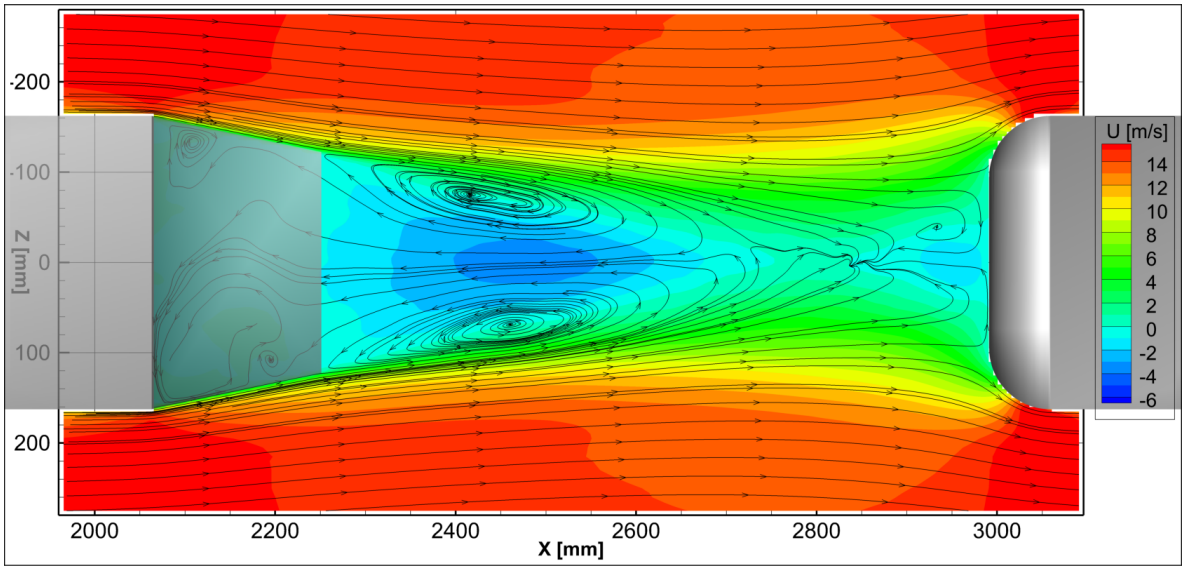
seen from the top is given. Also here the general flow pattern when comparing experiment and simulation is quite similar. The wake is made up of two vortices which are symmetric for the simulation results. For the experiment a slight asymmetry can be seen. In the experiment the cores of these vortices lie more upstream which is also visible from table 4.8. Also here the wake predicted by the simulation is longer, which can be seen from the location of the saddle point, and the region of flow between the wake and the front of the trailing model has a lower magnitude. Next to this a vortical structure in front of the trailing model can be seen for the simulation data. Because of the lateral misalignment the experimental data shows two streamlines one for leaving the saddle point and one defining the stagnation point. The lateral misalignment also explains the offset of the stagnation point. Because of the vortical structure seen from the simulation no clear stagnation streamline is defined.

Table 4.8: Vortex core, saddle- and stagnation point location in the horizontal centre plane for the R68 Tail 12°-R68 platoon at 0.45 s/L

	Exp		**Sim**	
	x [mm]	**z [mm]**	**x [mm]**	**z [mm]**
Left vortex	2500	92	2460	69
Right vortex	2509 - 2476	-54 - -62	2415	-76
Saddle point	2666	20	2721	-16
Stagnation point	3006	84	2993	0



(a) Experiment



(b) Simulation

Figure 4.18: Streamlines with contours of x-velocity in the horizontal centre plane of the R68 Tail 12°-R68 platoon

4.2 Explanation of the differences between the numerical and experimental results

Although the results from the experiment and simulation were quite comparable, some differences did exist. These differences will be explained here by discussing the errors from the numerical method (section 4.2.1) and those that occurred during the experimental campaign (section 4.2.2).

4.2.1 Numerical Errors

Discretization

The effect of the mesh size was discussed in section 2.2.5. The used mesh differed only 3 drag counts from the one with double the spatial resolution for the single baseline model. This was deemed to be enough but a finer spatial discretization could lead to even closer results compared to the experiment.

Next to this no extra spatial resolution was used around the ground plate. The lack of this can lead to an incorrectly predicted boundary layer over this plate and thus also an incorrectly predicted underbody flow which leads to a different wake structure.

Averaging time

As was explained in section 2.2.5 all the simulations were run for 3.6 seconds with an averaging window active for the last 1.8 seconds. This averaging time is about 6 times lower than that of the experiment where 8000 images at a frequency of 749 Hz were taken to average the flow field. This difference in averaging time can lead to a different flow field as small errors have a greater impact when a smaller averaging time is used compared to a longer one.

Boundary layer modelling

In section 2.2.2 boundary layer transition model was disabled because it was assumed that the boundary layer started out fully turbulent due to the tripping with the help of zig-zag tape. For the baseline model this seemed to be the case. For the models with smaller front edge radii however the zig-zag strips used for the baseline model were not enough to fully trip the boundary layer as flow separation was seen. To fully trip the boundary layer more zig-zag tape should have been used but at the time no extra tape was available. This difference in boundary layer modelling leaded to the large mismatch in drag coefficient for the models with smaller front edge radii as severe flow separation for the experiment was seen.

Turbulence modelling

PowerFLOW uses VLES and to solve the large turbulence scales and the $\kappa - \epsilon$ RNG to model the unresolved scales. This means that not all the small vortices and turbulent structures that exist in the gap are correctly simulated which can lead to a different flow field.

4.2.2 Experimental Errors

Model

Whereas the model used in the simulation is one piece and everything is perfectly aligned this is not the case for the experimental model. As explained in section 3.1.2 these models are made up of different parts which were not always aligned perfectly. For example there was a small backwards facing step at the top between the nose and the base of the model. The wooden plates used to make the base of the model were also not perfectly aligned, sometimes part of the top or bottom plate was a bit proud or recessed. It was also noticed that the tails were not manufactured perfectly square but had the shape of a parallelogram. During the experiment it was attempted to make these tails square by bending them slightly but this attempt was unsuccessful. Lastly the edges of the model and transitions between multiple parts were made as smooth as possible by using tape. Because of the soap this tape did not stick after some time which could have gone unnoticed for some runs and can affect the measurements.

Alignment

During the experiment it was very difficult to properly align the models with respect to the wind tunnel and to each other. A small yaw angle could have existed between the model and the wind tunnel. The models in the platoon were aligned by moving the scissor lift in the OJF which can move over the floor by air cushions. However small adjustments were very difficult because of the weight and resistance of this platform. That is why several alignment errors were seen during the experiment which lead to a different flow field compared to the numerical results.

Coordinate conversion

In order to convert the coordinates from the CVV measurements to those of the model coordinate system use was made of a MATLAB program which required the coordinates of the model. For some of the runs this conversion resulted in unexpected coordinates and a manual shift was required. This shift was determined by looking at the outline of the model which could be seen from the results. When determining this shift errors on the size of several millimetres could have occurred as the grid size was 7.5 mm. When comparing profiles and planes from the simulation and experiment this can result in a plane for the experimental measurements that is in a slightly different location.

Unsteady force behaviour

The PSD of the unsteady forces was very different when comparing the numerical and experimental results. From the simulation only the force on the model is taken into account. For the experiment this was not possible since the model is connected to the ground plate. It is assumed that the interaction between the model and ground plate together with possible additional vibrations generated by the structure are the cause of the higher amplitude and different frequency. Next to this the length of the signal used for the analysis can also be the reason.

Chapter 5

Conclusions and Recommendations

Now that all the results from the numerical and experimental analysis have been discussed and compared conclusions can be drawn. This will be done in this chapter. Next to conclusions some recommendations for further studies on platooning of heavy duty vehicles are given.

5.1 Conclusions

5.1.1 Single Model

Before the platoon configurations were tested first the single models were analysed. Next to the baseline model the effect of a smaller frontal radius and the addition of tails with varying angles was also investigated.

Baseline Model

The drag coefficient of the baseline model that has a radius of 68 mm was 0.344 and 0.327 from the numerical and experimental analysis respectively. From the numerical data it could be seen that most of the drag was generated by the wake of the model. This wake consists of a toroidal recirculation region in which a vortex ring is present. The unsteady forces show that the drag, side and lift force fluctuate at a Strouhal number of 0.073, 0.058 and 0.102 and 0.130 and 0.160. From the experimental data these fluctuations take place at a Strouhal number of 0.216 for the drag and lift and 0.140 for the side force. These differences are assumed to be caused by the rotating disk upon which the model was mounted. From the numerical analysis it was found that these fluctuations are caused by the fluctuations in the flow field with most of them coming from the shear layer at the bottom and sides of the model.

Effect of Frontal Radius

When a sharper frontal radius is applied to the models the drag rises to 0.361 and 0.600 from the numerical data and 0.553 and 0.744 from the experimental analysis for the models with a radius of 34 mm and 17 mm. The difference between numerical and experimental data is caused by the separation that can be seen in the experiment for the model with a radius of 34 mm. For the model with a front radius of 17 mm separation was seen from both the numerical and experimental results. The simulation did not predict the separation because it was assumed that the boundary layer was fully turbulent which was not the case in the experiment.

Effect of Tails

The models where a tail was applied showed a drag reduction compared to the baseline model. The drag reductions were 7, 72 and 117 drag counts for the simulation and 14, 81 and 116 drag counts for the experiment for the tails with an angle of 0°, 6° and 12°. This drag reduction comes from the higher pressure that acts on the rear of the model. Next to the reduction of the average forces the unsteady forces are also influenced. The simulation data shows that the amplitudes of drag and side forces have diminished compared to the baseline model which improves driver comfort. The higher the tail angle the lower the fluctuations. The reason for these lower fluctuations is due to the lower fluctuations in the flow field and in particular in the shear layer.

5.1.2 Platoon Configurations

Intervehicle distance 0.10 s/L

At an intervehicle distance of 0.10 times the vehicle length all configurations benefit from the platoon formation. For the baseline platoon, where both models have a front radius of 68 mm, the numerical results show that it loses 42% and 32% of its drag for the leading and trailing model respectively. Most of the drag reduction comes from the rear and front of the leading and trailing model. This drag reduction is caused by the flow pattern that exists between the models. The flow follows an S-shaped path moving from the bottom to the top of the models. In the gap the toroidal recirculation region is still visible but has been drastically reduced in size. The vortices in this gap are the cause of low pressure while the stagnation that takes place on the front and rear surfaces is the reason for the high pressure peak that was seen in the middle of the gap. At this distance there is only a little increase in the amplitude of the unsteady drag force. For the side force an amplitude with a magnitude about 3.5 times higher than the single model was seen. This is due to the vortices which when leaving the gap flow over the rounded edges on the side of the model.

When a sharper radius of 17 mm is applied to the trailing vehicle the drag reductions change to 43% and 59% for the leading and trailing model from the numerical data and 63% for the trailing model in the experiment. The flow field in the gap is very similar to that of the

baseline platoon. Because of the sharper front radius the top and bottom vortex are better contained in the gap, another effect is that the flow needs to take a sharper turn which leads to a higher stagnation pressure and lower pressure in the middle of the gap. Next to this the separation that was seen for the single model has disappeared due to the more favourable pressure gradient. The unsteady drag force shows an amplitude similar to that of the baseline platoon. For the sideforce the amplitude has diminished this is because due to the sharper radius less area is exposed to the sides.

The last platoon that was tested is the one where the trailing model had a vertical misalignment. This was done because this vertical misalignment was seen during the experiment. For this configurations the drag reduction drop to 40% and 18% for the leading and trailing model from the simulation. The drag reduction from the experiment is 20% for the trailing model. In this case more flow from the underbody enters into the gap. This causes faster flow in the gap which leads to higher stagnation pressures and lower pressures in the vortices. The unsteady drag and side forces are much higher compared to the baseline platoon. This is due to the higher pressure fluctuations.

Intervehicle distance 0.45 s/L

For the second intervehicle distance not all vehicles benefit from the platoon configuration. For the baseline platoon the leading model experiences a drag reduction of 31%. The drag of the trailing model increases with 24% for the simulation and 19% for the experiment. This drag increase is due to the lack of thrust generated by the rounded edges of the front. The drag reduction of the leading vehicle is caused by an increase of the base pressure. At this distance the wake flow is quite similar to that of the single model. The flow enters the gap from the top, bottom and sides and ends up in the toroidal recirculation region. Flow leaving this region stagnates on the front of the trailing model or flows over the rounded edges where it accelerates. The unsteady forces show twice the amplitude for the drag force compared to the single model and 6.5 times the side force amplitude. These high values are caused by the impacting vortices which are stronger at this configuration.

The model with a sharper front radius does benefit from the platoon. The drag of the leading vehicle is 69% and the trailing model drag reduces with 26% for the simulation and 43% for the experiment. This mismatch in drag reduction comes from the mismatch for the drag of the single models. The flow field is almost identical to that of the baseline platoon. The amplitude of the unsteady drag force is higher than that of the baseline platoon, for the side force it is similar.

When a tail is applied to the leading model its drag reduction increases to 65%. The drag of trailing model increases with 14% for the simulation and 16% for the experiment. This is lower than the baseline platoon due to more suction being generated by the rounded edges. Due to the tail the recirculation region has been reduced in size. The magnitude of the reversed flow is also lower compared to the baseline platoon. The unsteady forces show that almost all fluctuations have been diminished this was also seen for the single model with a tail.

Intervehicle distance 0.91 s/L

At the final intervehicle distance all configurations benefit again from the platoon configuration. The drag reduction of the leading and trailing model of the baseline platoon is 7% and 5%. For the configuration where the trailing model has a sharper radius the drag reduction is 7% and 33%. This is higher than the platoon at 0.45 interverhicle distance and is due to the lowered stagnation pressure but hardly altered suction that is generated by the rounded edges. At this distance the effect of the platoon on the flow between the two models is hardly noticeable. The wake structure is almost identical to that of the single model. The unsteady forces show slightly higher amplitude compared to the single model.

Comparison between the two analysis methods

The drag results from both methods were quite comparable to each other, only the single models with a sharper front radius had a large mismatch but this was due to a numerical error in the boundary layer simulation. There was also quite a large difference when comparing the pressure profiles but this can be due to the error in the coordinate conversion from the CVV coordinate system to the model coordinate system. The flow field is quite comparable, the differences that were seen can be explained by a lack of resolution in the simulation and the alignment errors that occurred during the experiment. The biggest difference was seen when comparing the results from the unsteady force analysis. It is assumed that the length of the signal, the influence of the rotating disk along with other vibrations are the cause of these large differences.

5.2 Recommendations

Although the results from the numerical analysis are quite similar compared to those obtained during the experiment but can be better if a finer discretization is used and the simulations are run for a longer time.

Because of the simplicity of the model the drag coefficient is much lower compared to a real life heavy duty vehicle. This also influences the drag reductions that were seen when the models were placed in the platoon configuration. A follow up study using more detailed models can lead to more realistic relative drag reductions. In this study the front of the model was vertical with respect to the flow, this was done because of the shape of European heavy duty vehicles. A recently introduced heavy duty vehicle the *Tesla Semi* has a shape that is not quite similar to an American nor an European heavy duty vehicle. It front is tilted with respect to the flow. It might be interesting to use this type of front shape for a future platoon studies. The used model in this study did also not take into account any cooling orifices which could influence the flow structure between the two models. In this study the platoon was studied with the flow only coming directly in the driving condition. It is known that heavy duty vehicles spend most of there time driving in crosswind conditions Van Raemdonck (2012). That is why for future studies varying yaw angles should also be considered when studying the flow between the two models.

During the experimental campaign it was noted that moving and aligning the models with respect to each other and the wind tunnel was no easy task. Because of the heavy scissor lift minor adjustments were next to impossible. This lead to several misalignments during the experiment which should be avoided if future platoon experiments are going be conducted in the OJF. The structure required to support the ground plate should also be made stiffer as during the experiment several wooden beams came loose due to vibrations.

When reconstructing the flow field from the CVV measurements it was noted that the resulting coordinates in model coordinate system were outside the expected range and a manual shift was required. This conversion relied on the location of the model in the reference frame of the minishaker by means of a set of images on which 3D-PTV was performed. For future studies use should be made of a more robust way to accurately pinpoint the model location, next to this the location of the model should be recorded for every configuration and after each movement or adjustment of the set-up

Bibliography

H.J. Alons. Ojf external balance. Technical report, National Aerospace Laboratory (NLR), 2008.

A/S Universal Robots. *UR5 Technical details*, 2017.

Ilhan Bayraktar, Drew Landman, and Oktay Baysal. Experimental and computational investigation of ahmed body for ground vehicle aerodynamics. In *SAE Technical Paper*. SAE International, 11 2001. doi: 10.4271/2001-01-2742. URL http://dx.doi.org/10.4271/2001-01-2742.

P. L. Bhatnagar, E. P. Gross, and M. Krook. A model for collision processes in gases. i. small amplitude processes in charged and neutral one-component systems. *Phys. Rev.*, 94: 511–525, May 1954. doi: 10.1103/PhysRev.94.511. URL https://link.aps.org/doi/10.1103/PhysRev.94.511.

Christophe Bonnet and Hans Fritz. Fuel consumption reduction in a platoon: Experimental results with two electronically coupled trucks at close spacing. In *SAE Technical Paper*. SAE International, 08 2000. doi: 10.4271/2000-01-3056. URL http://dx.doi.org/10.4271/2000-01-3056.

Fred Browand, John McArthur, and Charles Radovich. Fuel Saving Achieved in the Field Test of Two Tandem Trucks. Institute of Transportation Studies, Research Reports, Working Papers, Proceedings qt29v570mm, Institute of Transportation Studies, UC Berkeley, June 2004. URL https://ideas.repec.org/p/cdl/itsrrp/qt29v570mm.html.

Canadian Trucking Alliance. Cta paves the way for boat-tails, longer b-trains & tri-drives, 2014. URL http://cantruck.ca/cta-paves-the-way-for-boat-tails-longer-b-trains-tri-drives/. Accessed: 2017-04-07.

Hudong Chen, Satheesh Kandasamy, Steven Orszag, Rick Shock, Sauro Succi, and Victor Yakhot. Extended boltzmann kinetic equation for turbulent flows. *Science*, 301(5633): 633–636, 2003. ISSN 0036-8075. doi: 10.1126/science.1085048. URL http://science.sciencemag.org/content/301/5633/633.

Shiyi Chen and Gary D. Doolen. Lattice boltzmann method for fluid flows. *Annual Review of Fluid Mechanics*, 30(1):329–364, 1998. doi: 10.1146/annurev.fluid.30.1.329. URL https://doi.org/10.1146/annurev.fluid.30.1.329.

Kevin Cooper. Bluff-body blockage corrections in closed- and open-test-section wind tunnels. In B.F.R. Ewald, editor, *Wind Tunnel Wall Corrections*, chapter 6, pages 6–1,6–28. Advisory Group for Aerospace Research & Development (AGARD), Neuilly-sur-Seine, 1998.

Edward G. Duell and A. R. George. Experimental study of a ground vehicle body unsteady near wake. In *SAE Technical Paper*. SAE International, 03 1999. doi: 10.4271/1999-01-0812. URL http://dx.doi.org/10.4271/1999-01-0812.

J. Eckhardt. European truck platooning challenge 2016: Lessons learnt, 2016.

Matthew Ellis, Joaquin Ivan Gargoloff, and Raja Sengupta. Aerodynamic drag and engine cooling effects on class 8 trucks in platooning configurations. *SAE Int. J. Commer. Veh.*, 8:732–739, 09 2015. doi: 10.4271/2015-01-2896. URL http://doi.org/10.4271/2015-01-2896.

European Truck Platooning. Photos daf, 2016. URL https://www.eutruckplatooning.com/press/photos+daf/default.aspx. Accessed: 2016-03-06.

European Union. Eu law and publications eur-lexeur-lex - 31996l0053 - en. http://eur-lex.europa.eu/legal-content/NL/TXT/?uri=celex:31996L0053, 1996. Accessed: 2017-03-07.

Exa Corporation. Powercase user's guide, 2017a.

Exa Corporation. Powerflow user's guide, 2017b.

Gunnar Farnebäck. Antigradient, 2014. URL https://github.com/GunnarFarneback/spatial_domain_toolbox.

Thorsten Frank and James Turney. *Aerodynamics of Commercial Vehicles*, pages 195–210. Springer International Publishing, Cham, 2016. ISBN 978-3-319-20122-1. doi: 10.1007/978-3-319-20122-1_12. URL http://dx.doi.org/10.1007/978-3-319-20122-1_12.

H. C. Garner, E. W. Rogers, W. E. Acum, and E. C. Maskell. *Subsonic Wind Tunnel Wall Corrections*, chapter Blockage Effects in Closed or Open Tunnels, page 310. North Atlantic Treaty Organization, Middlesex, England, 1966.

T. Gheyssens. Aerodynamic analysis of a platoon of bluff bodies subjected to cross wind. Master's thesis, Delft University of Technology, 2016.

KUI Hai-lin, XU Xiang-gang, LI Ming-da, and TIAN Chong-he. Effect of lateral wind and longitudinal spacing on the two trucks in tandem. *Journal of Jilin University (Engineering and Technology Edition)*, 46(5):1426, 2016. doi: 10.13229/j.cnki.jdxbgxb201605007. URL http://xuebao.jlu.edu.cn/gxb/EN/abstract/article_13031.shtml.

M. Hammache and F. Browand. On the aerodynamics of tractor-trailers. Technical report, Dept. of Aerospace and Mechanical Engineering, University of Southern California, 2004.

M. Hammache, M. Michaelian, and F. Browand. Aerodynamic forces on truck models, including two trucks in tandem. In *SAE Technical Paper*. SAE International, 03 2002. doi: 10.4271/2002-01-0530. URL http://dx.doi.org/10.4271/2002-01-0530.

Harwell and Didcot. "good practice guide truck aerodynamic styling". Internal publication, Department for Transport, june 2001.

Daniel G. Hyams, Kidambi Sreenivas, Ramesh Pankajakshan, D. Stephen Nichols, W. Roger Briley, and David L. Whitfield. Computational simulation of model and full scale class 8 trucks with drag reduction devices. *Computers & Fluids*, 41(1):27 – 40, 2011. ISSN 0045-7930. doi: http://dx.doi.org/10.1016/j.compfluid.2010.09.015. URL http://www.sciencedirect.com/science/article/pii/S0045793010002434. Implicit Solutions of Navier–Stokes Equations. Special Issue Dedicated to Drs. W.R. Briley and H. McDonald.

item Industrietechnik GmbH. Profile 5, December 2017. URL http://product.item24.nl/nl/producten/productcatalogus/products/profile-5.html.

C. Jux. Robotic volumetric particle tracking velocimetry by coaxial imaging and illumination. Master's thesis, Delft University of Technology, 2017.

Bahram Khalighi, S. Zhang, C. Koromilas, S. R. Balkanyi, Luis P. Bernal, G. Iaccarino, and P. Moin. Experimental and computational study of unsteady wake flow behind a bluff body with a drag reduction device. In *SAE Technical Paper*. SAE International, 03 2001. doi: 10.4271/2001-01-1042. URL http://dx.doi.org/10.4271/2001-01-1042.

Siniša Krajnović and Lars Davidson. Large-eddy simulation of the flow around a ground vehicle body. In *SAE 2001 World Congress*. SAE International, mar 2001. doi: 10.4271/2001-01-0702. URL https://doi.org/10.4271/2001-01-0702.

Siniša Krajnović and Lars Davidson. Numerical study of the flow around a bus-shaped body. *Journal of Fluids Engineering*, 125(3):500–509, 2003. ISSN 0098-2202. doi: 10.1115/1.1567305. URL http://dx.doi.org/10.1115/1.1567305.

Michael P. Lammert, Adam Duran, Jeremy Diez, Kevin Burton, and Alex Nicholson. Effect of platooning on fuel consumption of class 8 vehicles over a range of speeds, following distances, and mass. *SAE Int. J. Commer. Veh.*, 7:626–639, 09 2014. doi: 10.4271/2014-01-2438. URL http://doi.org/10.4271/2014-01-2438.

L.E.M. Lignarolo, D. Ragni, C. Krishnaswami, Q. Chen, C.J. Simão Ferreira, and G.J.W. van Bussel. Experimental analysis of the wake of a horizontal-axis wind-turbine model. *Renewable Energy*, 70(Supplement C):31 – 46, 2014. ISSN 0960-1481. doi: https://doi.org/10.1016/j.renene.2014.01.020. URL http://www.sciencedirect.com/science/article/pii/S0960148114000494. Special issue on aerodynamics of offshore wind energy systems and wakes.

Bogdan Marcu and Fred Browand. Aerodynamic forces experienced by a 3-vehicle platoon in a crosswind. In *SAE Technical Paper*. SAE International, 03 1999. doi: 10.4271/1999-01-1324. URL http://dx.doi.org/10.4271/1999-01-1324.

Brian R. McAuliffe. Improving the aerodynamic efficiency of heavy duty vehicles: wind tunnel test results of trailer-based drag-reduction technologies. Report, National Research Council Canada. Aerospace, 2015/07/22 2015.

Rick Mihelic, Jeff Smith, and Matthew Ellis. Aerodynamic comparison of tractor-trailer platooning and a-train configuration. *SAE Int. J. Commer. Veh.*, 8:740–746, 09 2015. doi: 10.4271/2015-01-2897. URL http://doi.org/10.4271/2015-01-2897.

J. D. Miller and C. Façanha. The state of clean transport policy a 2014 synthesis of vehicle and fuel policy developments. Technical report, The International Counsil on Clean Transportation (ICCT), 2014.

Maryam Mirzaei and Siniša Krajnović. *Large Eddy Simulations of Flow Around Two Generic Vehicles in a Platoon*, pages 283–288. Springer International Publishing, Cham, 2016. ISBN 978-3-319-30602-5. doi: 10.1007/978-3-319-30602-5_35. URL http://dx.doi.org/10.1007/978-3-319-30602-5_35.

R. Muncrief and B. Sharpe. Overview of the heavy-duty vehicle market and co_2 emissions in the european union. Technical report, The International Counsil on Clean Transportation (ICCT), 2015.

Jason M. Ortega, Tim Dunn, Rose McCallen, and Kambiz Salari. *Computational Simulation of a Heavy Vehicle Trailer Wake*, pages 219–233. Springer Berlin Heidelberg, Berlin, Heidelberg, 2004. ISBN 978-3-540-44419-0. doi: 10.1007/978-3-540-44419-0_22. URL http://dx.doi.org/10.1007/978-3-540-44419-0_22.

R Pagliarella. *On the aerodynamic performance of automotive vehicle platoons featuring pre and post-critical leading forms*. PhD thesis, RMIT University, 2009.

G Rajamani. Cfd analysis of air flow interactions in vehicle platoons. Master's thesis, RMIT University, 2006.

Rampf Tooling Solutions GmbH. Polyurethane board for styling & design, 03 2015.

J. Roberts, R. Mihelic, and M. Roeth. Two truck platooning. Confidence report, North American Council for Freight Efficiency, 2016.

SAE. *SAE Wind Tunnel Test Procedure for Trucks and Buses*, jul 2012. URL https://doi.org/10.4271/J1252_201207.

SAE. *Guidelines for Aerodynamic Assessment of Medium and Heavy Commercial Ground Vehicles Using Computational Fluid Dynamics*, sep 2013. URL https://doi.org/10.4271/J2966_201309.

Fulvio Scarano, Sina Ghaemi, Giuseppe Carlo Alp Caridi, Johannes Bosbach, Uwe Dierksheide, and Andrea Sciacchitano. On the use of helium-filled soap bubbles for large-scale tomographic piv in wind tunnel experiments. *Experiments in Fluids*, 56(2):42, Feb 2015. ISSN 1432-1114. doi: 10.1007/s00348-015-1909-7. URL https://doi.org/10.1007/s00348-015-1909-7.

Daniel Schanz, Sebastian Gesemann, and Andreas Schröder. Shake-the-box: Lagrangian particle tracking at high particle image densities. *Experiments in Fluids*, 57(5):1–27, 2016. URL http://elib.dlr.de/99710/. Article 70, Published online: 27 April 2016.

Andrea Sciacchitano and Fulvio Scarano. Elimination of piv light reflections via a temporal high pass filter. *Measurement Science and Technology*, 25(8):084009, 2014. URL http://stacks.iop.org/0957-0233/25/i=8/a=084009.

Jeff Smith, Rick Mihelic, Brandon Gifford, and Matthew Ellis. Aerodynamic impact of tractor-trailer in drafting configuration. *SAE Int. J. Commer. Veh.*, 7:619–625, 09 2014. doi: 10.4271/2014-01-2436. URL http://doi.org/10.4271/2014-01-2436.

S M Soloff, R J Adrian, and Z-C Liu. Distortion compensation for generalized stereoscopic particle image velocimetry. *Measurement Science and Technology*, 8(12):1441, 1997. URL http://stacks.iop.org/0957-0233/8/i=12/a=008.

Sauro Succi and J.M. Yeomans. *The lattice Boltzmann equation for fluid dynamics and beyond*. Oxford University Press, Oxford, UK, 2001.

TU Delft. Open jet facility (hsl). http://www.lr.tudelft.nl/organisatie/afdelingen/aerodynamics-wind-energy-flight-performance-and-propulsion/facilities/wind-tunnel-lab/open-jet-facility-hsl/, 2016.

B W van Oudheusden. Piv-based pressure measurement. *Measurement Science and Technology*, 24(3):032001, 2013. URL http://stacks.iop.org/0957-0233/24/i=3/a=032001.

GMR Van Raemdonck. *Design of Low Drag Bluff Road Vehicles*. PhD thesis, Delft University of Technology, 2012.

GMR Van Raemdonck and MJL Van Tooren. Time averaged phenomenological investigation of a wake behind a bluff body. In *Bluff Body Aerodynamics and Application VI Conference, Milan, Italy*, 2008.

S. Watkins and G. Vino. The effect of vehicle spacing on the aerodynamics of a representative car shape. *Journal of Wind Engineering and Industrial Aerodynamics*, 96(6-7):1232–1239, 2008. doi: 10.1016/j.jweia.2007.06.042. URL https://www.scopus.com/inward/record.uri?eid=2-s2.0-44649180496&doi=10.1016%2fj.jweia.2007.06.042&partnerID=40&md5=0ed45fd3394668c78c41e8a2621942c6.

B. Wieneke. Volume self-calibration for 3d particle image velocimetry. *Experiments in Fluids*, 45(4):549–556, Oct 2008. ISSN 1432-1114. doi: 10.1007/s00348-008-0521-5. URL https://doi.org/10.1007/s00348-008-0521-5.

Richard Wood. A review of reynolds number effects on the aerodynamics of commercial ground vehicles. *SAE Int. J. Commer. Veh.*, 5:628–639, 09 2012. doi: 10.4271/2012-01-2045. URL https://doi.org/10.4271/2012-01-2045.

Richard M Wood. A discussion of a heavy truck advanced aerodynamic trailer system. In *Int. Symp. Heavy Veh. Weights Dimens., 9th, University Park, PA*, 2006.

Appendix A

Experimental Set-up

A.1 Single Model

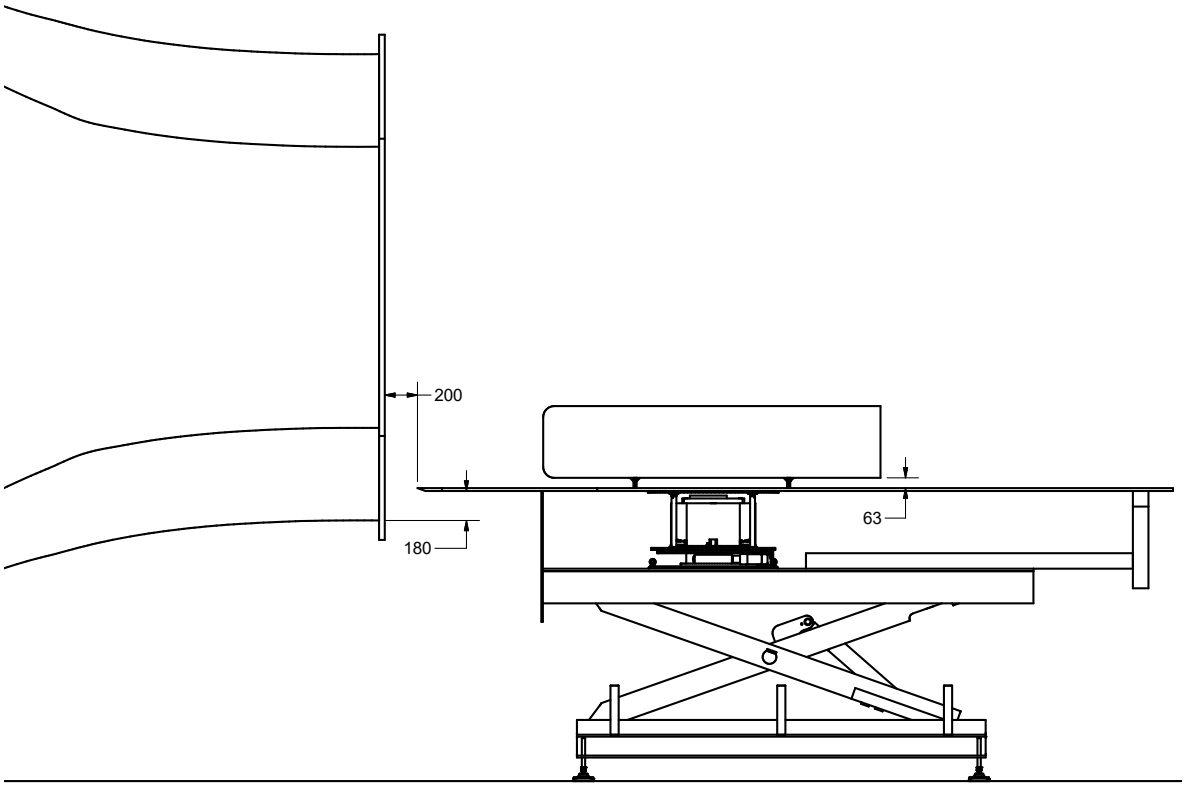


Figure A.1: Side view of the single model experimental set-up [mm]

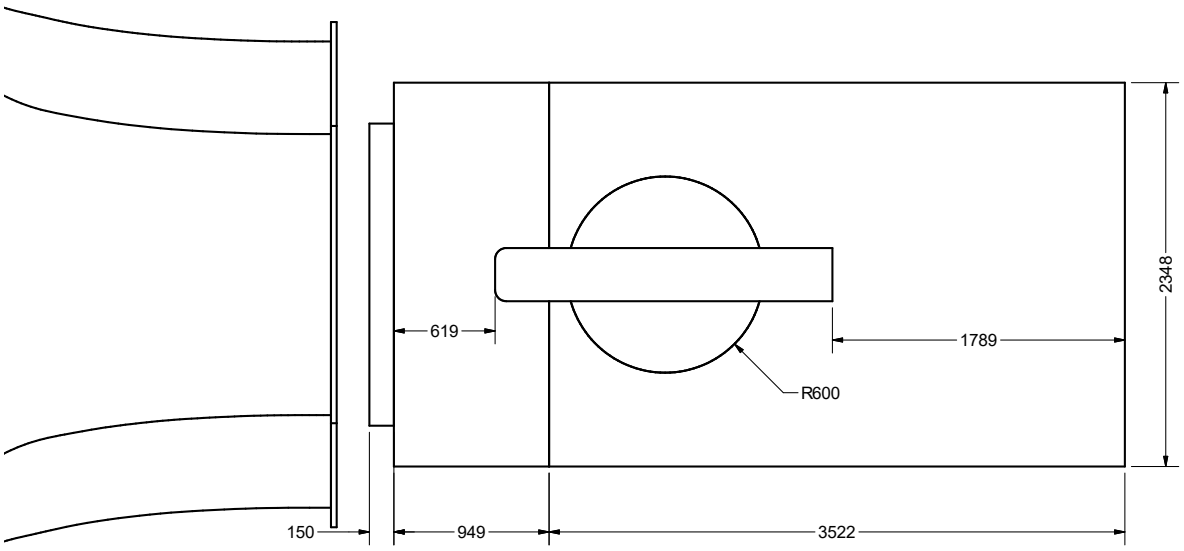


Figure A.2: Top view of the single model experimental set-up [mm]

A.2 Platoon

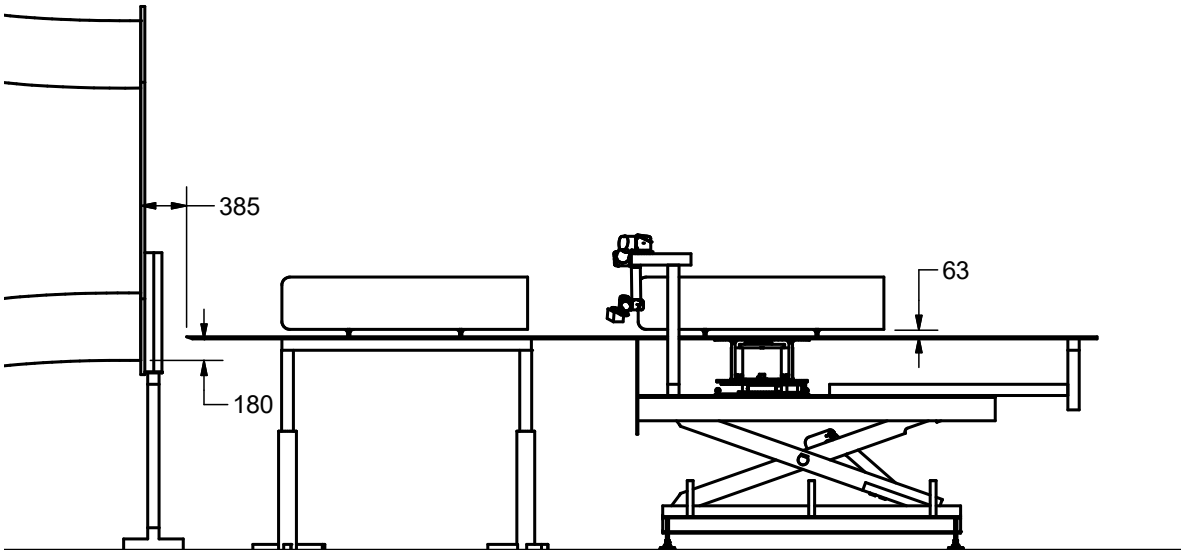


Figure A.3: Side view of the platoon experimental set-up [mm]

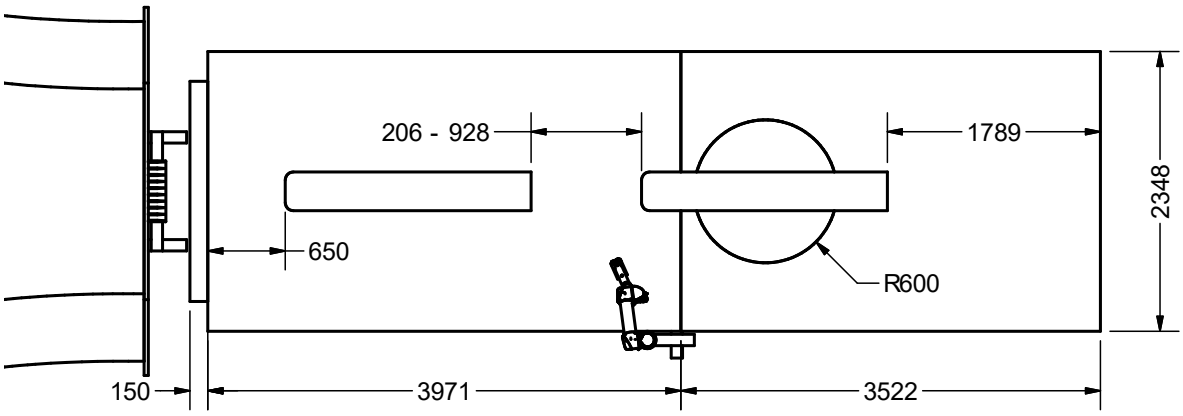


Figure A.4: Top view of the platoon experimental set-up [mm]